

**MODELLING PAPER MICROSTRUCTURE AND ITS ROLE IN
TONER TRANSFER IN XEROGRAPHIC PRINTING**

By

TAO WU, B. S., M. Sc.

A Thesis

Submitted to the School of Graduate Studies

In Partial Fulfillment of the Requirements

For the Degree

Doctor of Philosophy

McMaster University

© Copyright by Tao Wu, October 2008

**MODELLING PAPER MICROSTRUCTURE AND ITS ROLE IN
TONER TRANSFER IN XEROGRAPHIC PRINTING**

DOCTOR OF PHILOSOPHY (2008)
(Materials Science and Engineering)

McMaster University
Hamilton, Ontario

**TITLE: Modelling Paper Microstructure and Its Role in
Toner Transfer in Xerographic Printing**

**AUTHOR: Tao Wu, B. S., M. Sc. (Tsinghua University, Beijing
- China)**

SUPERVISOR: Professor Nikolas Provatas

NUMBER OF PAGES: XVIII, 169

ABSTRACT

This thesis investigates paper structure and how its spatial heterogeneity affects the electrostatic and contact forces responsible for the toner transfer in Xerographic printing. Modeling predictions and experiments are reported which link length scales of variation in toner density distribution in Xerographic printing with certain structural length scales in paper.

A modified 3D fibre network model is introduced, which is used to simulate handsheet paper microstructure. Specific measures addressed by the model include formation, surface roughness and porosity. Simulated (i.e. virtual) handsheet paper structure is compared with that from specially prepared laboratory handsheet, obtaining a good correspondence between theory and experiments.

An efficient Multigrid Poisson solver is used to simulate the electrostatic fields involved in the Xerographic toner transfer process. The distribution of dielectric property is input into the solver either analytically or from simulated 3D paper webs prepared by the fibre network model of paper. A spectral analysis is used to elucidate the relative importance of spatial variations of paper surface, filler and porosity in establishing spatial variations of the electrostatic field. It is found that only long wavelength variations in either surface height, bulk filler or porosity affect variations in electrostatic toner transfer forces to any relevant degree. Furthermore, it is shown

that the long wavelength perturbations of the electrostatic field can be modeled using a new 1D effective capacitor model. Direct use of simulated handsheet paper webs - which are described by several heterogeneous measures - shows that to lowest order it is the paper surface structure *not* formation is responsible in shaping the electrostatic toner field variations.

A new platform for modeling toner transfer in Xerographic printing is also introduced. It combines the 3D stochastic fibre network model of paper, the 3D electrostatic field solver, paper compression in the printing nip, and contact adhesion forces acting on toner particles during Xerographic printing. The modeling platform is used to demonstrate that paper-press interactions are critical in shaping the surface of paper, which, in turn, has the greatest influence in controlling both the electrostatic and contact adhesion forces responsible for shaping the distribution of toner transferred to paper during Xerography.

ACKNOWLEDGEMENTS

I would like to start by showing my deep and sincere gratitude to my supervisor Dr. N. Provatas for the support and help in the field of research and study. Thanks for his generous sharing of knowledge, intelligence and experience which add great value to this research.

I would like to thank Chaohui Tong, a Postdoctoral Fellow in my group, who helped me co-develop some of the models and numerical codes in this work.

I would also like to give special thanks to Gordon Sisler at the Xerox Research Center of Canada (XRCC), who was closely involved in this project and help with experimental facilities and instructive suggestions and ideas. Special thanks also to XRCC and the National Science and Engineering Research Council of Canada (NSERC) for funding this work.

Special thanks to Dr. R. H. Pelton, from the Department of Chemical Engineering, who shared their handsheet making facilities and surface profilometer with us. Special thanks also to Dr. Kari Dalnoki-Veress, from Department of Physics and Astronomy, who allowed us to use their micro-indentation equipment for investigating the compressibility of paper. I would like to thank his graduate student Adam Raegan for invaluable discussions and suggestions. Special thanks also go to Jim Garrett for fabricating the tips for micro-indentation experiments. Finally, I would like to give a

Special thanks to Dr. D. S. Keller, who performed beta-radiography tests on some of our samples.

Thanks to all my group, Jun Fan, Michael Greenwood and Peter Stefanovic, who gave me lots of useful suggestions related to my life, study and research over the years.

Finally, I would like to thank my wife, Jing Li, for her strong support and help.

TABLE OF CONTENTS

ABSTRACT	II
ACKNOWLEDGEMENTS	IV
TABLE OF CONTENTS	VI
LIST OF FIGURES	VIII
LIST OF TABLES	XVIII
CHAPTER 1 Introduction	1
1.1 Background	1
1.2 Objectives	3
1.3 Organization of the Thesis	4
CHAPTER 2 Literature Review	6
2.1 Electrophotographic Process.....	6
2.2 Toner Transfer Process.....	8
2.2.1 Overview.....	8
2.2.2 Previous Models for Toner Transfer Process	10
2.3 Paper Structure	16
2.3.1 Paper Making Process	16
2.3.2 Paper Composition	18
2.3.3 Inhomogeneous Paper Structure.....	20
2.3.4 Paper Structure Simulation	26
2.4 Physical Properties of Toner	28
2.4.1 Toner Fabrication.....	28
2.4.2 Size of Toner Particles.....	30
2.4.3 Charge of Toner Particles	32
2.4.4 Toner Adhesion Force	35
CHAPTER 3 Modeling Paper Structure	42
3.1 Introduction to 3D Fibre Network Model of Paper.....	43
3.1.1 Fibre Deposition.....	43
3.1.2 Fibre Interactions.....	44
3.1.3 Fibre Collapse and Flexibility.....	46
3.1.4 Consolidation of Simulated Paper Webs	50
3.2 Experimental Validation of Fiber Network Model of Paper	54
3.2.1 Laboratory Handsheet Preparation.....	54
3.2.2 Structure Analysis for Uncompressed Handsheet Paper	57
3.2.3 Calibrating the Paper Structure Model from Experiments	67

3.3 Improvement of “dry” Paper Compression Formalism	76
3.3.1 Experimental Characterization from Micro-Indentation Testing.....	77
3.3.2 Experimental Results and Discussion	82
3.3.3 Incorporating Paper-Nip Compression into Paper Structure Model ..	95
CHAPTER 4 Analysis of Electrostatic Toner Transfer Forces	97
4.1 Toner Transfer Physics Revisited	97
4.2 Multigrid Solver for the Poisson Equation with Random Dielectric Field ..	99
4.3 One-Dimensional Electrostatic Transfer.....	107
4.4 Spectral Analysis of Electrostatic Field Variations	111
4.4.1 Effect of Surface Fluctuations.....	112
4.4.2 Effect of Filler and Porosity Fluctuations.....	117
CHAPTER 5 The Role of Paper Structure Heterogeneity in Xerograph	126
5.1 Analysis of Electrostatic Field in Toner Layer Using Simulated Paper ...	126
5.2 Predicting Toner Density Distribution onto Paper	129
5.2.1 Toner Transfer Experiments	129
5.2.2 Comparison of Experiments and Simulations: The Importance of Paper Deformation and Contact Adhesion in the Print Nip.....	133
5.2.3 Comparison of Simulations and Experiment: Predicting Toner Density Distribution	138
CHAPTER 6 Conclusion and Future Work.....	146
6.1 Conclusion	146
6.2 Future Directions.....	150
6.2.1 Moisture Distribution in Paper.....	150
6.2.2 Corona Charging	150
6.2.3 Effect from the Combination of Surface and Filler Distribution.....	154
BIBLIOGRAPHY	160

LIST OF FIGURES

Chapter 1

- Figure 1.1 A magnified image for a piece of commercial paper that is printed with black toner, indicated by dark black. The circles show typical scales of toner variation, also known as *print mottle*.....2

Chapter 2

- Figure 2.1 Six steps of Electrophotographic process7
- Figure 2.2 The toner transfer process in Xerography9
- Figure 2.3 Toner transfer model (copied from Yang 1976)..... 10
- Figure 2.4 1-D transfer model (copied from Butler 1991)..... 12
- Figure 2.5 The four-layer model for toner transfer process (copied from Cassidy 2004) 15
- Figure 2.6 A SEM micrograph showing the surface structure typical of commercial paper sheet. 19
- Figure 2.7 The Scanning Electron Microscope image of a paper surface (copied from Alava 2006).20
- Figure 2.8 Example of paper cross section showing fibre and fillers (copied from Alava 2006).....24
- Figure 2.9 Cross-sectional image of a coated paper sheet (copied from Alava 2006). 24
- Figure 2.10 SEM cross-section (bottom) for a 7460 μm filled-paper substrate (copied from Cassidy 2004).25
- Figure 2.11 Two crossing fibres on the square lattice (copied from Niskanen 1994)27
- Figure 2.12 SEM photograph of (a) pulverized toner and (b) polymerized toner (copied from Grushkin 1992)..29

Figure 2.13 Coulter Counter (copied from Hoffmann 2004).....	31
Figure 2.14 Schematic charge test (copied from Hoffmann 2004)	33
Figure 2.15 Experiments on charge distribution (copied from Hoffmann 2004)..	34
Figure 2.16 centrifuge measurements for adhesion force (copied from Hoffmann 2004)	36
Figure 2.17 AFM measurements for toner adhesion (copied from Hoffmann 2004)	36
Figure 2.18 Toner on AFM cantilever (SEM image) (copied from Hoffmann 2004)	37
Figure 2.19 Electric field detachment measure of toner adhesion (copied from Hoffmann 2004).....	37

Chapter 3

Figure 3.1 Paper structures with different formations (a) Random fibre networks ($\rho = 1.0$); (b) uniform fibre networks ($\rho \rightarrow 0, \alpha = 0.5$). (units: 5 μm)	45
Figure 3.2 Paper structures with different fibre collapse index (a) Low collapse fibre network ($C_i = 1.0$); (b) High collapse fibre network ($C_i = 3.0$) (Units: 5 μm).....	47
Figure 3.3 Paper structures with different fibre flexibility(a) Stiff fibre network ($T_f = 0.1$); (b) flexible fibre network ($T_f = 1.0$). (units: 5 μm)	49
Figure 3.4 Standard 159-mm-diameter sheet machine, opened to reveal mesh on which handsheet forms. (Courtesy of Dr. R. Pelton, Chemical Engineering department, McMaster University)	56
Figure 3.5 Beta-Radiographic image for handsheet paper (basis weight 36g/m ²).	58
Figure 3.6 An interference microscope (copied from Wyko Menu).....	61

Figure 3.7 A 3-D surface profile for a handsheet paper sample (Basis weight 36 g/m ²).	61
Figure 3.8 Two-point mass correlation function of (a) an area of laboratory made handsheet paper; (b) a piece of commercial paper.	64
Figure 3.9 Plots of the two-point mass-mass correlation function (formation correlation) for six different samples and their average.	66
Figure 3.10 Plots of the two-point height-height correlation function (roughness correlation) for six different samples and averaged result.....	67
Figure 3.11 Schematic of Fibre Dimensions (The interior of the fibre is hollow and is termed the lumen) (Deng 1994)	68
Figure 3.12 SEM image of hardwood fibre after beating	70
Figure 3.13 Optical microscope image of fibre after beating	72
Figure 3.14 The simulated paper surface, the size in the x and y directions is 5 mm by 5 mm in unit of 5 μm, with a minimum resolution of 5 μm..	74
Figure 3.15 Handsheet surface profile obtained by Wyko NT1100 surface profiler, the scale in each direction is 5 mm by 5 mm, with a minimum resolution of 5 μm.	74
Figure 3.16 Plots of the two-point mass-mass correlation function (formation correlation), for simulated virtual and experimental handsheet paper samples.....	75
Figure 3.17 Plots of the two-point height-height correlation function (roughness correlation) for paper roughness from simulated and experimental handsheets paper samples.	75
Figure 3.18 Generic compression behaviour of a cellular, honeycomb material. (Rodal 1983, Gibson 1988).....	78
Figure 3.19 Two stage compression testing	82
Figure 3.20 Force-displacement behavior for different indenters	84
Figure 3.21 Stress-strain behavior from six samples of handhseet papers of basis	

weight 30.48 g/m ² , under an 855 μm radius indenter head.	85
Figure 3.22 Stress-strain behaviours of varying paper densities under (i) a 505 μm radius and (ii) a 425 μm radius indenter head.....	87
Figure 3.23 Stress-strain behaviours for varying indenter head radius for samples with average density of (i) 30.48 g/m ² and (ii) 92.45 g/m ²	88
Figure 3.24 Schematics of additional effect h.	91
Figure 3.25 Normalized Stress-Strain results from 16 groups of experiments: Four different indenter heads (210 μm, 425 μm, 505 μm, and 855 μm) acting on four different paper thickness (195 μm, 123 μm, 102 μm, and 50 μm).	91
Figure 3.26 The lateral spreading of strain outside the indenter region over the indenter radius h^* (h/R_{ind}) is plotted against R_{ind}/R_{ind}^{max}	92
Figure 3.27 Scaling results of normalized h^* (h/R_{ind}) against R_{ind}/R_{ind}^{max} . Different curves separate into different paper thicknesses.	92
Figure 3.28 Scaling results of h^{**} against sample thickness.....	93
Figure 3.29 Stress vs. strain response of the trend-line of the scaled stress curve in Figure 3.25 shown in cyan.	966

Chapter 4

Figure 4.1 Toner transfer model.....	98
Figure 4.2 Schematics of FMG (Trottenberg 2001)	105
Figure 4.3 Illustration of system geometry and notation for the 1D model. The two dark lines show a 1D slice in which the model of Yang and Hartman are applied.	108
Figure 4.4 Power spectrum of the z-component of electric field obtained from the full solution of the Poisson Equation for a paper surface of the form $H = \bar{H} + \sum_k A_k \sin(2\pi x/\lambda_k)$, where the wave number is in unit of	

$2\pi/L$, with $L = 256 * 5 \mu m$. Other constants include $\lambda_k = L/k$, where $k = 2, 5, 20, 40, 60$, $\bar{H} = 80 \mu m$, $A_k = 6 \mu m$. The inset compares the real-space z-component of electric field obtained from Full Poisson equation solution to the solution of the 1D multi-layer model using principal modes of $k = 2, 5, 20$ to reconstruct the local paper thickness. In the inset, x is in unit of $5 \mu m$ and the electric field is in unit of 10^6 volts/meter..... 113

Figure 4.5 Power spectrum of the z-component of the electric field vs. wave number k for the case of cosine wave perturbation of the paper surface. Frequencies used are the same as in the data of Figure 4.4. The inset compares the real-space z-component of the electric field obtained from the full solution of the Poisson equation to the multi-layer 1D model that uses the principal modes of $k = 2, 5, 20$ to reconstruct the local surface roughness. Other parameters are as defined in Figure 4.4..... 115

Figure 4.6 Power spectrum of the electric field vs. wave number in x direction with $k_y = 2$. In the inset shows the plane $k_y = 5$. Other parameters are as defined in Figure 4.4..... 117

Figure 4.7 Power spectrum of the z-component of electric field obtained from the numerical solution of the Poisson equation for the case where the paper surface is a superposition of sine waves of frequencies $k = 5, 60$ and equal amplitude of $15 \mu m$. Inset: filler particles of size $5 \times 2 \mu m$ are distributed across the surface at a frequency corresponding to $k = 60$. The inset compares the z-components of electric fields obtained from the full solution of the Poisson equation with and without a filler particle in each valley of paper surface. Other

parameters are the same as in Figure 4.4..... 118

Figure 4.8 Plot of the z-component of electric field (solid line) obtained from numerical solution of the Poisson equation for a paper surface described by the form $H = \bar{H} + A \sum_k s \sin(2\pi kx/L)$, where $k = 2, 5, 10$, $\bar{H} = 80 \mu\text{m}$, $A = 10 \mu\text{m}$. The figure also displays the electric fields after the insertion of filler particles in the valleys of the paper surface. In each valley of the paper surface corresponding to $k = 10$, filler agglomerates of size $5 \times 4 \mu\text{m}$ (dash-dotted line), $5 \times 8 \mu\text{m}$ (star line) and $15 \times 8 \mu\text{m}$ (dotted line) are inserted. For comparison, the z-component of electric field with filler particles fully filling the gap between paper surface and the bottom of toner layer (open-circle line) is also shown in the figure. All other units are as in Figure 4.4..... 119

Figure 4.9 Power spectrum of the z-component of the electric field obtained from the full solution of the 3D Poisson equation. Filler particles follow a uniform-random spatial distribution and are deposited near the top surface of the paper (dotted line), bottom paper surface (dash-dotted line), or distributed throughout the entire bulk (solid line). The paper is idealized to have zero roughness and a caliper (thickness) of $81.25 \mu\text{m}$. In all the cases, the total volume fraction of filler particles is 20%. The size of filler particle occupies one unit cell, $5 \times 1.5625 \mu\text{m}$. The thickness of toner and photoconductor layers are the same as in Figure 4.2 In the inset, the z-components of electric fields along the middle of toner layer are shown for the three cases. All other units are the same as in Figure 4.4..... 122

Figure 4.10 Power spectra of: the z-component of the electric field obtained from our 3D Poisson solver (solid line), the integrated filler particle thickness in z direction at each lateral position (dot-dashed line) and

the integrated power spectra from the complete dielectric distribution from all layers across the paper thickness (open-circle line). For this simulation, filler particles are uniformly-randomly distributed inside the entire bulk with 20 % volume fraction. Other parameters are the same as in Figure 4.9. The inset is the blow-up of the plots in long wavelength regime. The vertical scales are arbitrary..... 124

Chapter 5

- Figure 5.1 Power spectra of: the z-component of the electric field obtained from our 3D Poisson solver using a simulated 3D paper web, the surface height of the simulated paper web, and the distribution of integrated pore heights at each lateral position. The x-axis corresponds to wave number k_x and we have set $k_y = 2$. The wave number is in unit of $2\pi / L$, with $L = 512 * 5 \mu\text{m}$ 127
- Figure 5.2 Comparison of power spectra of surface height (open-circle line for $k_y = 2$, starred line for $k_y = 15$) and of the integrated air height distribution (solid line for $k_y = 2$, dash-dot line for $k_y = 15$) for our laboratory handsheets. 129
- Figure 5.3 SEM image for toner particle distribution on a laboratory handsheet sample, under (a) 500x magnification, (b) 100x magnification..... 131
- Figure 5.4 Scanned image for $5 \times 5\text{mm}^2$ area. 131
- Figure 5.5 Power spectrum of toner density distribution obtained from printed zones. The x-axis corresponds to wave number k . The wave number is in units of $2\pi/L$, with $L = 512 \times 5 \mu\text{m}$ 132
- Figure 5.6 Power spectra of: (i) z-component of electric field corresponding to original simulated paper webs (dash-dotted line); and (ii) toner density distribution obtained from experimentally printed zones (solid line).

	The x -axis corresponds to wave number k . The wave number is in units of $2\pi/L$, with $L = 512 \times 5 \mu\text{m}$	133
Figure 5.7	Simulated paper surfaces before (a) and after (b) compression. The axes are scaled in units of $5 \mu\text{m}$. Paper basis weight is 36g/m^2 and average paper caliper before compression is $80 \mu\text{m}$. The paper is compressed to a mean strain of 0.083.	135
Figure 5.8	Illustration of various forces acting on a toner particle.	136
Figure 5.9	Schematic of the toner transfer and paper structure modeling platform	138
Figure 5.10	Circularly averaged power spectra of: (i) toner density distribution obtained from simulation without compression(dash-dotted line); (ii) toner density distribution obtained from simulation under strain 0.05 (dash line); (iii) toner density distribution obtained from simulation under strain 0.10 (dotted line); (iv) toner density distribution obtained from simulation under strain 0.20(shadow line); and (v) toner density distribution obtained from experimentally printed zones (solid line). The x -axis corresponds to wave number k . The wave number is in units of $2\pi/L$, with $L = 512 \times 5 \mu\text{m}$	140
Figure 5.11	Circularly averaged power spectra of: (i) toner density distribution obtained from simulation under strain 0.10 (dotted line) and (ii) toner density distribution obtained from experimentally printed zones (solid line). The x -axis corresponds to wave number k . The wave number is in units of $2\pi/L$, with $L = 512 \times 5 \mu\text{m}$	141
Figure 5.12	Circularly averaged power spectra of: (i) z -component of electric field corresponding to uncompressed simulated paper webs (dash-dotted line); (ii) z -component of electric field corresponding to compressed simulated paper webs (dotted line) and (iii) toner density distribution obtained from experimentally printed zones (solid line).	

The x -axis corresponds to wave number k . The wave number is in units of $2\pi/L$, with $L = 512 \times 5 \mu\text{m}$	142
Figure 5.13 Circularly averaged power spectra of: (i) surface height of a simulated paper webs before compression (dash-dotted line); (ii) surface height of the simulated paper webs after compression (dotted line) and (iii) toner density distribution obtained from experimentally printed zones (solid line). The x -axis corresponds to wave number k . The wave number is in units of $2\pi/L$, with $L = 512 \times 5 \mu\text{m}$	143
Figure 5.14 Circularly averaged power spectra of: (i) overall mass density from simulated paper webs before compression (dash-dotted line); (ii) overall mass density from simulated paper webs after compression (dotted line) and (iii) toner density distribution obtained from experimentally printed zones (solid line). The x -axis corresponds to wave number k . The wave number is in units of $2\pi/L$, with $L = 512 \times 5 \mu\text{m}$	144

Chapter 6

Figure 6.1 Arrangement for measurement of corona charge decay (copied from IEC 61340-2-1 2000)	152
Figure 6.2 Charge decay curves for handsheets paper with different basis weight.	153
Figure 6.3 Charge decay curves for handsheet paper vs. special made paper	153
Figure 6.4 Power spectrum of the filler layer.....	154
Figure 6.5 The power spectra of electrostatic transfer field from (i) filler layer replaces the bottom layer of 3D dielectric (dashed line); (ii) filler layer replaces the middle layer of 3D dielectric (dotted line) (iii) filler layer replaces the top layer of 3D dielectric (solid line)	155
Figure 6.6 power spectrum of electrostatic transfer field from new modified 3D	

dielectric distribuiton.....	156
Figure 6.7 The power spectra of electrostatic transfer field from (i) filler layer added to the top of the modified 3D dielectric (dash-dotted line); (ii) new modified 3D dielectric distribuiton (solid line).	156
Figure 6.8 The power spectra of electrostatic transfer field from (i) filler layer added to the bottom of the modified 3D dielectric (dash-dotted line); (ii) new modified 3D dielectric distribuiton (solid line)	157

LIST OF TABLES

Chapter 2

Table 2.1 Characteristic properties of softwood fibres used in papermaking	18
--	----

Chapter 3

Table 3.1 Properties for six grades of handsheet sample	57
Table 3.2 Average properties for the chosen sample	66
Table 3.3 Experimental Fibre Dimensions (Scott 1995).....	68
Table 3.4 Material and statistical properties for simulated paper and experimental samples.	73

Chapter 4

Table 4.1 Number of iterations for different kinds of iterative methods	101
---	-----

Chapter 1

Introduction

1.1 Background

Electrophotography, a process formally invented by Chester F. Carlson between 1930s and 1940s is the technology that underlies the operation of virtually all copy machines and laser printers today. Electrophotography and Xerography rely upon six fundamental steps: the charging of a photoconductor (image exposure) whereby the photoconductor is exposed to an image, the development of the latent image on the photoconductor, transferring the toner image from the photoconductor to paper or other printing media, fusing the toner permanently onto the printing medium and, lastly, cleaning and restoring the photoconductor for further use. Print quality depends upon the understanding, control and optimization of each step. To date, most scientific investigations of Electrophotography (Xerography) have focused on electrostatic image creation and development steps. Very little attention has been given to the transfer step, which is perhaps the most critical for high quality digital printing.

To obtain high quality and high resolution printing, one of the crucial requirements in Xerography lies in the uniform distribution of toner particles. However, *print mottle* (Figure 1.1) - a non-uniformity of toner particle distribution -

always accompanies the toner transfer, particularly when printing onto paper. This is the case with and without thermal fusing. Although it is clear that the non-uniformity of paper structure and toner attributes will lead to the print mottle, very little is known about the mechanisms by which paper formation (i.e. paper's area mass density distribution), paper thickness, paper moisture distribution, toner charge and size distribution affect the transfer process. It is in this context that this thesis will undertake to study how several measures of paper structure heterogeneity affect the distribution of toner transfer in Xerographic printing. This will be examined mostly by examining the role of the electrostatic toner transfer and, to some degree, the contact adhesion forces at work during Xerography.

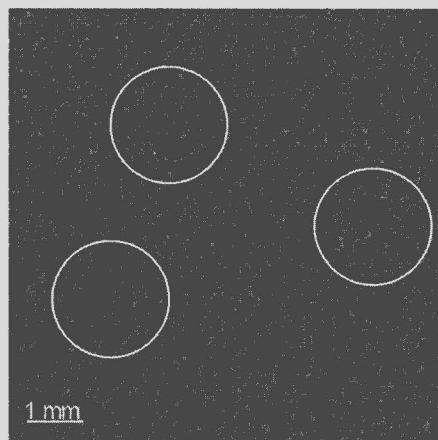


Figure 1.1 A magnified image of a portion of commercial paper that is printed with black toner, indicated by dark black. The circles show typical scales of toner variation, also known as *print mottle*.

1.2 Objectives

The first objective of the project involves the development of a new 3D, parallel Multigrid Poisson solver, which is specially tailored toward: a model to predict electrostatic toner transfer fields during Xerographic printing onto an arbitrary printing substrate. This model is integrated with a recently upgraded 3D fiber-network model of paper structure. This composite modeling platform is used to predict how spatial variations in paper formation, surface height variations (surface roughness), porosity and filler distribution control spatial variations in toner density on digitally printed paper sheets (a process that relies on one of the most critical sub-processes of Xerography: electrostatic transfer of charged polymeric-based toner to paper).

The second objective of this work involves a suite of experiments to characterize the structural heterogeneity of paper structure. Specifically, these include measurements of: mass density distribution in various types of laboratory handsheets, measurements of surface roughness variations and measurements of local paper compressibility and its relation to local mass density and indenter head size. These experiments are used to validate the 3D paper structure model. An additional set of experiments follows to characterize the spatial variation of toner transferred to paper without toner fusing. These experiments are used to validate our toner transfer simulations. Paper structure characterization experiments were done at McMaster

University and at State University of New York, Syracuse, while toner transfer and toner distribution measurements were conducted at Xerox Research Center in Canada (XRCC).

1.3 Organization of the Thesis

Chapter 2 gives a literature review on the following areas: the six steps of the Electrophotography; the physics in toner transfer process in Xerography and the model developed to simulate this process; the paper making process, as well as the paper heterogeneous structure; adhesion forces in toner transfer process.

Chapter 3 gives a detailed introduction on the 3D fibre network model and its calibration against laboratory [uncompressed] handsheets paper samples which are made and characterized using the two-point correlation function applied to mass and surface height distribution.

In chapter 4, an efficient 3D Poisson Solver based on the Multigrid method is presented. This model is used to understand how electrostatic toner transfer fields are affected by variations in surface roughness, filler, porosity and formation of paper. This includes a so-called *principal mode mathematical analysis* to elucidate the relative importance of different frequencies of variation of the paper surface, filler and porosity.

In chapter 5, a composite model involving the 3D stochastic fibre network model of paper, the 3D electrostatic field solver, paper compression in the printing nip of a Xerographic printer, and contact adhesion forces acting on toner particles are combined. The relative importance of paper surface and mass density variations in establishing the electrostatic and contact adhesion forces crucial in controlling toner transfer density distribution during Xerography is studied.

Chapter 6 concludes this work and discusses possible extensions.

Chapter 2

Literature Review

2.1 Electrophotographic Process

In Electrophotographic printing, the image to be duplicated is placed onto a glass surface where, through white light or exposure, the image is transferred to a photo-conducting drum. The photo-conducting drum or semi-conducting drum (i.e. a drum carrying a thin-film optical semiconductor) has been previously exposed to a positive electrostatic charge. When the reflected light from the original image contacts the drum surface, areas of illumination cause the positive charge to be neutralized while areas not illuminated (image areas) retain their positive charge. The drum is then passed through the area holding negatively charged powdered toner, which is attracted to positively charged areas on the drum. The drum continues to rotate and reaches the in-feed of the printing substrate (e.g. paper). The toner particles are transferred to the substrate by an electrostatic field created between the toner layer and the substrate. The toner is subsequently heated to its glass transition temperature, whereupon it is fused onto the paper surface (Schaffert 1975, Schein 1988, Williams 1984). Electrophotography is thus a complex process, usually including six distinct steps, listed below in a clockwise fashion, starting from the twelve o'clock position in

figure 2.1.

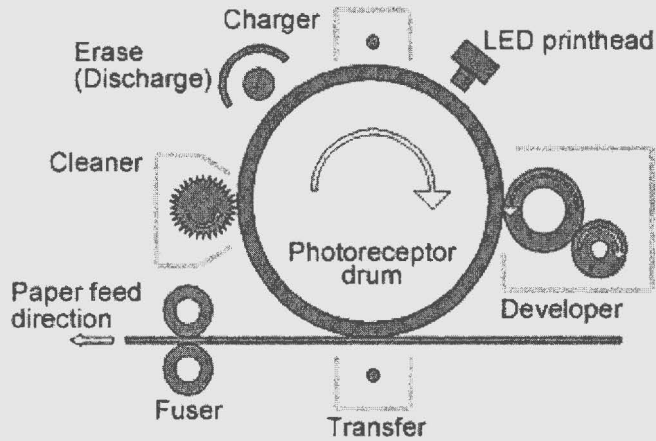


Figure 2.1 Six steps of Electrophotographic process.

- a. Charge - A corona discharge generated by air breakdown charges the surface of the photoconductor uniformly.
- b. Exposure - Light, which is reflected from the image (in a copier) or produced by a laser (in a printer), discharges the normally insulating photoconductor producing a latent image- a charge pattern on the photoconductor that mirrors the information to be transformed into the real image.
- c. Development - Electrostatically charged and pigmented polymer particles named as toner, roughly about 10 micron meters in diameter, are brought into the vicinity of the latent image. By the electric field created by the charges on the photoconductor,

the toner adheres to the latent image, transforming it into a real image.

- d. *Transfer* - The developed toner particles on the photoconductor is transferred onto paper by corona charging the back of the paper with a layer of charge opposite to that of the toner particles. In some other designs applying a “bias” voltage across the transfer gap also does this process.
- e. *Fusing* - The image is permanently fixed to the paper by melting the toner into the paper surface.
- f. *Clean* – By using coronas, lamps, brushes and scraper blades, the photoconductor is discharged and the excess toner particles are cleaned.

The transfer of toner particles from a photo-conducting surface to a substrate is of fundamental importance to the scope of this PhD project.

2.2 Toner Transfer Process

2.2.1 Overview

When a substrate (e.g. paper) is placed under the negatively charged toner particle layer, there is a three-layer system formed, paper layer - toner particles layer - photo conductor layer. When a voltage is applied across this three-layer structure, an electric field is created; this is presumed to provide the major force that transfers the

toner to the paper. The strength of this transfer field depends on the local dielectric of the printing substrate, toner and photoreceptor (See figure 2.2). In the toner particle layer, there are adhesion forces at play in addition to the electrostatic forces described above. The adhesion forces¹ serve to attach the toner particles to the photoconductor drum. These forces act to prevent toner particles from transferring onto the substrate. At asperities in the toner layer where the electrostatic transfer force is large enough to overcome the adhesion forces, toner particles will detach from the drum and transfer to the paper substrate. This is the basic process of toner transfer.

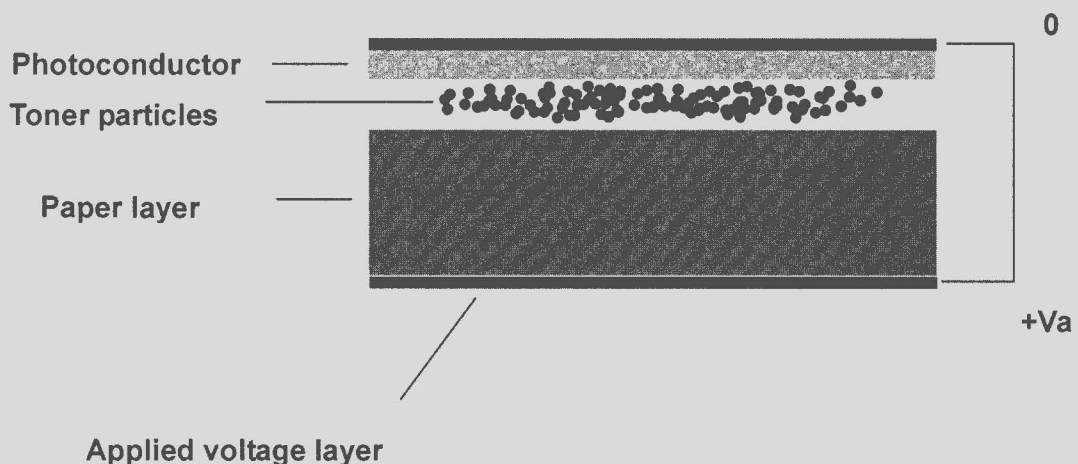


Figure 2.2 The toner transfer process in Xerography. Typically, the toner layer is one-particle thick.

¹ Adhesion forces are intentionally not mentioned here and in much of this thesis as we do not wish to speculate about the nature of forces that the community itself seems to be undecided about. Indeed we merely wish to show and model the interplay between the obvious electrostatic (i.e. Bias) field and the “other” adhesion forces that have a molecular origin and serve merely to cause the toner to adhere toward a surface, such as the photoconductor.

2.2.2 Previous Models for Toner Transfer Process

The work of Yang and Hartmann (Yang 1976) is one of the earliest references giving a quantitative model to simulate the transfer process. Below is an abridged treatment of their paper. The toner particle layer and electrode geometry is shown in figure 2.3.

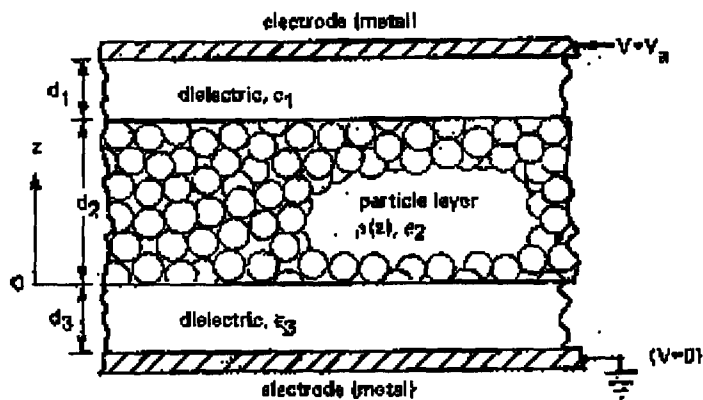


Figure 2.3 Toner transfer model (copied from Yang 1976).

There is a layer of toner particles which is sandwiched between two dielectric layers (1 is print medium and 3 is photoconductor layer). A constant potential V_a is applied to the two metal electrodes adjacent to the dielectric layers. The layer of toner particles is in a state of stress from mechanical (adhesion) and electrostatic forces. This net stress in the toner layer, $P(z)$, is given by the relation

$$P(z) = \int_0^z \rho(z)E(z)dz + P_m - \varepsilon_p E_p^2 \quad (2.1)$$

where $\rho(z)$ is the charge density of the toner layer, $E(z)$ is the electric field in the toner layer, P_m is the mechanical adhesion strength between the toner particles and paper layer, compression force $\varepsilon_p E_p^2$ is due to the electrostatic attraction of the two metal electrodes, E_p is the electric field in paper layer. Thus, $P(z)$ is equal to the total electrostatic and mechanical stress within the particle layer. The cohesive strength $C(z)$ of the particle layer has its origin in particle-particle interactions and particle-electrode adhesive forces.

Consider the boundary between layers 2 and 3: when the mechanical stress is tensile, the particle layer separates when $P(z)$, the sum of the electrostatic stresses, and P_m first exceeds the cohesive strength $C(z)$. The location of layer separation is $z = z_s$, and this locus is found by solving for the minimum extremum in total stress $P(z) - C(z)$. Finally the mass fraction F remaining attached to dielectric layer 1 after rupture can be defined by transfer efficiency

$$F = 1 - \frac{z_s}{d_2} \quad (2.2)$$

The work of Yang and Hartmann established a 1D triple layer model. It was among the first models to provide quantitative way to obtain the toner mass after toner transfer process. Its main limitation was that it is a mean-field model, i.e. it applies only in an average sense, assuming that paper is uniform, described entirely by a constant dielectric that enters the above formalism. In reality, paper is a highly

heterogeneous medium. The most common stochastic components of paper structure include mass density, surface roughness, thickness, moisture and filler distribution, all of which affect the local dielectric property of paper. Another limitation of this model is that it assumes a uniform toner charge distribution through the multi-particle toner layers. In modern Xerography there is typically only 1 (perhaps 2) layers of toner particles in the print nip.

The work of Butler and Hoburg (Butler 1991) uses a model (figure 2.4) for the electrophotographic toner transfer process in which some toner particles are assumed to become airborne when the electric field between photoconductor and paper surfaces becomes large enough to overcome adhesive forces (Scharfe 1984). In their work, they described a dynamic process in which the toner and its associated charge are detached from the photoconductor surface, and deposited onto the paper surface. They assumed that the toner and charge are transported on both moving surfaces.

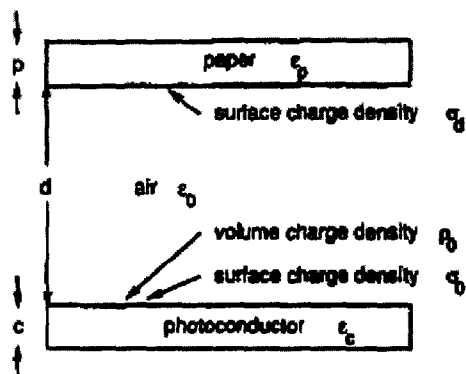


Figure 2.4 1-D transfer model (copied from Butler 1991).

In figure 2.4, voltage V_0 is applied across the photoconductor with height c and permittivity ε_c , air gap with height d and permittivity ε_0 , as well as paper with height p and permittivity ε_p . The surface charge density of the toner layer on the photoconductor surface is σ_0 and the toner surface charge density on the paper surface is σ_d . The toner particle flux begins at the photoconductor surface with a specified space charge density ρ_0 , depleting σ_0 , and terminates at the paper surface where σ_d accumulates.

According to steady-state conservation of charge, they assume the current density at each vertical position within the air gap be the same

$$J = J_0 \hat{x} \quad (2.3)$$

According to the constitutive law, they related the current density J_0 to the particles with mobility b , charge density $\rho(x)$ and electric field $E(x)$

$$J_0 = b\rho(x)E(x) \quad (2.4)$$

From Gauss' law, they related the electric field and charge density in the air gap

$$\varepsilon_0 \frac{dE}{dx} = \rho(x) \quad (2.5)$$

Combining equation (2.4) and (2.5), they solved the resulting differential equation and obtained

$$E(x) = (E_0^2 + \frac{2\rho_0 E_0 x}{\varepsilon_0})^{1/2} \quad (2.6)$$

They denoted the Electric fields across the photoconductor and paper by E_c and E_p respectively. From the Gauss's law boundary conditions at the photoconductor and paper surfaces, they obtained

$$\varepsilon_0 E_0 - \varepsilon_c E_c = \sigma_0 \quad (2.7)$$

and

$$\varepsilon_p E_p - \varepsilon_0 \left(E_0^2 + \frac{2\rho_0 E_0 d}{\varepsilon_0} \right)^{1/2} = \sigma_d \quad (2.8)$$

Plus the constraint for applied voltage V_0

$$V_0 = \int_0^d \left(E_0^2 + \frac{2\rho_0 E_0 x}{\varepsilon_0} \right)^{1/2} dx + cE_c - pE_p \quad (2.9)$$

From equation (2.7), (2.8) and (2.9), they obtained the equation as below,

$$V_0 = p \frac{\sigma_d}{\varepsilon_p} - c \frac{\sigma_0}{\varepsilon_c} + \frac{\varepsilon_0}{\varepsilon_c} cE_0 + \int_0^d \left(E_0^2 + \frac{2\rho_0 E_0 x}{\varepsilon_0} \right)^{1/2} dx + \frac{\varepsilon_0}{\varepsilon_p} p \left(E_0^2 + \frac{2\rho_0 E_0 d}{\varepsilon_0} \right)^{1/2} \quad (2.10)$$

For given applied voltage V_0 , the injected space charge density ρ_0 , and surface charge densities σ_0 and σ_d , can be used to determine E_0 . Finally they used the secant root-finding algorithm (Hornbeck 1975) to obtain E_0 , and then E_c and E_p . E_0 , E_c , E_p are the electric fields across the air gap, photoconductor and paper respectively. They also developed a two-dimensional model on this process.

The previous model gives an insight of airborne toner transfer process and the basic physical parameters that govern it. However, once again, the main limitation of

the model is that it assumes the paper and toner particles are uniformly distributed materials.

The work of Cassidy, Grant and Provatas (Cassidy 2004) sets up the 4-layer capacitor-structure model for toner transfer process (figure 2.5).

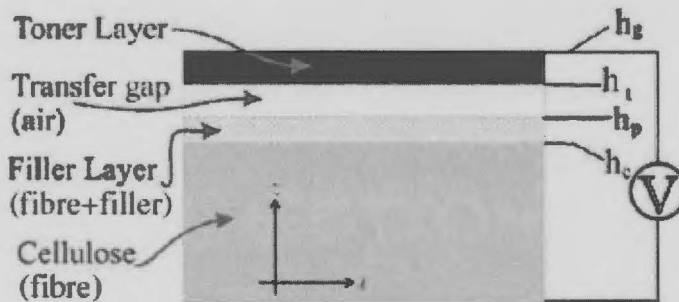


Figure 2.5 The four-layer model for toner transfer process (copied from Cassidy 2004).

They used finite element method to solve the Poisson equation within a continuous dielectric distribution comprising a four-layer system (paper, filler layer, air gap, and toner layer) between two parallel plates at a fixed voltage. The effect of filler particle concentration and depth through the paper was examined using mathematically designed distributions. Using experimental SEM paper images from which to derive dielectric constant distribution of paper, this work also indicated a link between spatial thickness variations in paper and toner transfer forces. The limitation of this work is that it used experimental paper structure as input, and it is based on an

electrostatic solver that is impractically slow. As a result, the approach of this work is diagnostic, not predictive, i.e. it characterizes how a paper sample affects toner transfer. It does not systematically consider how various hypothetical (virtual) paper making strategies will affect toner transfer.

This PhD work will extend the work of Cassidy et. al. by making a predictive simulation model that can simulate real as well as virtually synthesized paper structures and which is aimed at predicting their effect on electrostatic transfer of toner to paper.

2.3 Paper Structure

2.3.1 Paper Making Process

The paper making process follows the progression below:

Fiber extraction → Stock Preparation → Sheet Formation → Pressing → Drying
→ Calendering → Paper

Native wood is put through mechanical chipping to reduce it to small, chip-like pieces (Scott 1995). These pieces are rigid in nature and require that the lignin, a polymeric material that adheres the wood fibres together (Kolseth 1986), be removed through chemical extraction. Once the lignin is removed the fiber clusters are separated and exhibit a more relaxed structure. The fibers are then refined causing

their surfaces to become rough and the internal walls to separate, allowing water to enter the cellulose region - the main chemical constituent of the fibers. After water is absorbed, the cellulose swells, making fibres more flexible. The individual fibers are then combined with excess water to produce a slurry (i.e. a suspension of fiber and water). Sometimes additions of a second or third fiber type are included. Inorganic components may also be added to the slurry, the most important being filler, which is added to (1) reduce surface roughness, (2) improve brightness and opacity, and (3) increase density. Typical fillers added to commercial type paper include clay, precipitated calcium carbonate (PCC) and titanium oxide (TiO_2). The slurry is then sprayed through a slit into a forming section where rolls and wire mesh webs are set up in such a way as to reduce the water content and increase the material consistency for forming. Simply put, the water is drained from the suspension, leaving on the wire mesh a felt-like paper web. At this stage the average thickness of the paper web can be several millimeters (Sundholm 1999).

The press section further dewateres the formed sheet, reduces the surface roughness and improves the overall strength by the rolling pressure exerted. The fibers are pressed together creating more fiber-fiber contact area allowing an increase in bonding between fibers. The sheet then enters a drying stage where much of the mechanically trapped moisture is removed and further fiber bonds are created, increasing the overall strength of the paper web. During drying, the sheet tends to take on the smoothness of the surface on which it was dried. The sheet is then moves to the

calendering stage. The calendering process feeds the sheet through another set of rolls, where the pressure plastically deforms fibers, further reducing surface roughness and bringing the final thickness to the scale of tens of microns.

2.3.2 Paper Composition

The most important components of the paper are cellulosic fibres, made from wood or other similar natural origins (e.g. cotton fibres), and the pore space formed by and in between the fibres. Typical dimensions are listed in table 2.1. The key characteristic of fibres is their length, which is a few millimeters in general.

Table 2.1 Characteristic properties of softwood fibres used in papermaking
(copied from Alava 2006)

	Coarseness (mg/m)	Length (mm)	Width (μm)	Basis weight (g/m^2)
Scots pine (spring wood)	0.16	2.1	37	4.3
Scots pine (summer wood)	0.31	2.1	30	10.3
Western hemlock	0.20	2.4	31	6.5
Douglas fir	0.25	2.8	34	7.1

In commercial paper grades, a carefully optimized combination of appropriate pulp fibre types and other constituents are included in the paper network. Usually two different fibres, i.e. softwood fibres and hardwood fibres, are blended to obtain better paper property, e.g. surface and mechanical property. Paper can be coated by a layer of

mineral particles, and the ‘bulk’ can contain similarly small-scale fillers that act to change the porosity and the optical properties. Thus, the fibre fragments, mineral fillers, colloids and many at micrometer-scale add to the complexity of the random fibre network.

Figure 2.6 shows a scanning electron microscope image of a commercial paper, from which we can see, (1) a random network of fibres; (2) white filler particles, which are randomly distributed around fibres; (3) different sizes of hole (pore) in the network, also randomly distributed. The process of papermaking is such that the resulting material exhibits a stochastic random network of cellulose fibres, fillers and air (main components) (Deng 1994).

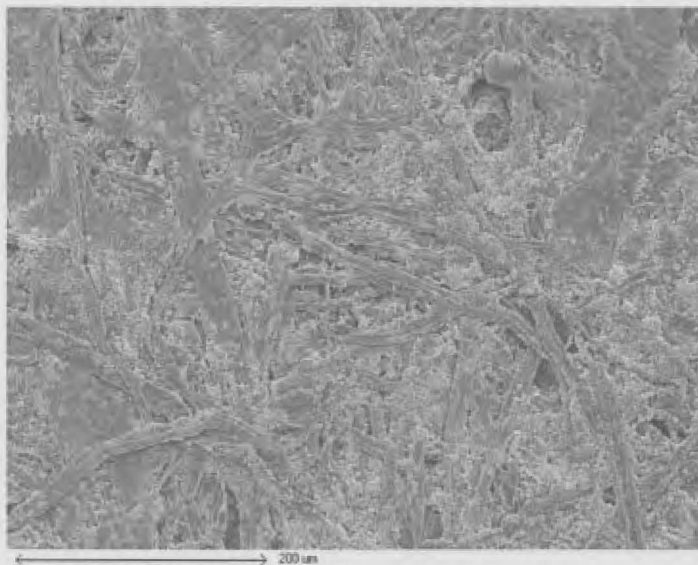


Figure 2.6 A SEM micrograph showing the surface structure typical of commercial paper sheet.

2.3.3 Inhomogeneous Paper Structure

2.3.3.1 Paper Formation

The origin of the inhomogeneity in paper comes from the sheet forming process. A turbulent flow of a suspension of water, fibres, colloids, fillers and other additives are generated in the paper making process. Then the combination of all the components above is filtrated and deposited on a wire. Thus, the stochastic nature of the whole paper making process leads to a planar network structure where the positions, orientations and shapes (i.e. curl, kinks, undulations, etc) of fibres are random (Soux 2008), as well as the distribution of fillers, colloids and other additives.

Figure 2.7 shows the structure of a paper surface.

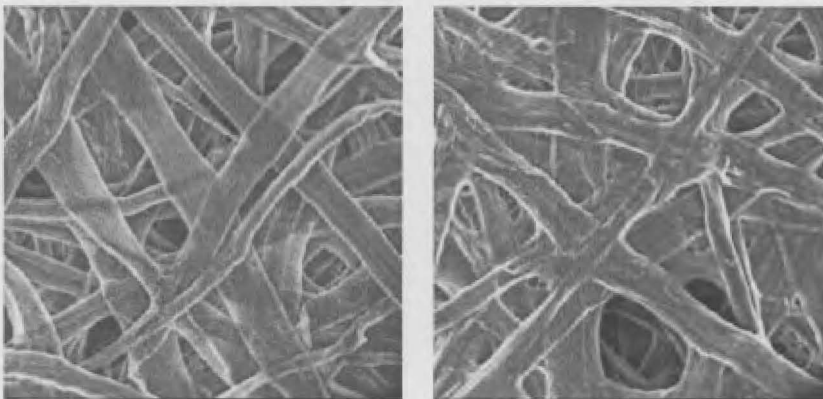


Figure 2.7 The Scanning Electron Microscope image of a paper surface. Two cases, paper dried under tension (left) and free of tension (right), are shown (copied from Alava 2006).

An important quantity used to determine paper formation (i.e. mass) distribution

is the areal mass per unit area, measured in units of grams per square metre. In the paper making industry, the uniformity of basis weight is considered to be one the most important properties of paper. Much of the effort in the development of paper making has gone into achieving uniformity of paper formation (Alava 2006).

Beta Radiography can be used to obtain the basis weight over a large number of small areas within a sample. One method is that of so-called contact Beta Radiography can be made of the whole sample and the variations in density of the radiography is analyzed with a microdensitometer. Several investigators have examined small-scale basis weight variations using the beta radiography (Norman 1976, Attwood 1962, Tydeman 1965, Ooij 1969, Norman 1974).

Originally, the X-ray film was used as detectors in the beta radiography imaging to obtain the paper formation. A source with uniform radiation intensity over its area is placed in contact with the sheet to be tested, and the transmitted radiation is recorded on an X-ray film. The result of exposure and subsequent development is a decreased transmission of light by the X-ray film. The optical density D of the film ('film absorbance') is proportional to the amount of radiation transmitted by the paper sample, and thus to the exposure time and to the transmission factor T_β (transmission coefficient for beta particles), so that

$$D = c \cdot t \cdot \exp(-\mu \cdot W) + D_\infty \quad (2.11)$$

$$T_\beta = \exp(-\mu \cdot W) \quad (2.12)$$

Where μ is the absorption coefficient, W is the basis weight of the sheet, c is a proportionality factor, t is the exposure time, D_{∞} is the optical density for infinite basis weight and can be determined on an unexposed part of the film.

Note that for zero basis weight, equation (2.11) becomes

$$D_0 = ct + D_{\infty} \quad (2.13)$$

Equations (2.11) and (2.12) can be rearranged as follows

$$\begin{aligned} \mu \cdot W &= \ln(ct) - \ln(D - D_{\infty}) \\ &= \ln(D_0 - D_{\infty}) - \ln(D - D_{\infty}) \\ &= \ln\left(\frac{D_0 - D_{\infty}}{D - D_{\infty}}\right) \end{aligned} \quad (2.14)$$

Thus the basis weight variations can be obtained by examination of the optical density D ('film absorbance') distribution on the X-ray film.

In another recently developed approach for beta radiography, the storage phosphor screens were used as detectors for the beta-radiography imaging of paper, which was a replacement for the X-ray film (Keller 2001). *This is the approach used in for beta radiography in this work.* In this approach, the paper sample was compressed between a ^{14}C radiation source and a phosphor screen detector. After exposing the paper sample for about 1 hour, the phosphor screen, which stored the amount of radiation, could be digitized and a data array was obtained. Finally, the formation distribution of the paper sample could be obtained. In this thesis work, the Beta Radiography, with storage phosphor screens as detectors, was used to obtain the

formation (mass density distribution or basis weight variation) for paper samples. The facility used for the examination was from Dr. Steven Keller, Faculty of Paper Science and Engineering, State University of New York.

Filler Distribution

Fillers, such as calcium carbonate (CaCO_3), titanium dioxide (TiO_2) or talc ($\text{Mg}_3(\text{OH})_2\text{Si}_4\text{O}_{10}$), are included in the paper pulp to increase some of the properties of paper (whiteness, printability, opacity, etc.). When a paper sheet is formed on a traditional *Fourdrinier* paper machine, pulp is delivered onto wire from a flow spreader termed the ‘headbox’ and water drains from the suspension to leave a mat on the wire. The evolving fibrous mat captures fillers preferentially towards the top surface and fillers entrained towards the bottom surface are washed out during the drainage process. Thus, the amount of fillers in a Fourdrinier- formed sheet decreases from the upper to the lower surface. Figure 2.8 shows a Z-direction distribution of the filler particles. The so-called burnout method can be used to reveal filler distributions near the paper surface (O’Neill 2000). Light reflected from the burned-out paper surface thus gives a reasonable indication of the filler distribution in x-y plane, by which the non-uniformity of filler distribution can be obtained (see also Provatas and Cassidy).

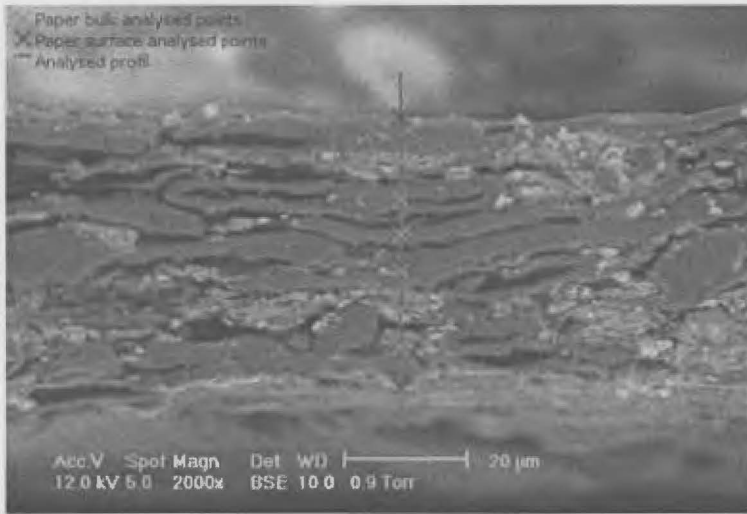


Figure 2.8 Example of paper cross section showing fibre (grey) and fillers (white) (copied from Alava 2006).

Paper Coating

High quality printing papers are typically coated (figure 2.9). The coating layer is analogous to the fill the holes in a wall before painting. This coating layer improves the uniformity of the paper surface and reduces the characteristic pore sizes from tens of microns at uncoated paper surface to fractions of a micrometer. Nevertheless, even with the finest of coatings, non-uniformity exists, which can influence micron-scale print quality.



Figure 2.9 Cross-sectional image of a coated paper sheet (The thickness is of the order of 0.1mm) (copied from Alava 2006).

Paper Thickness Variation

Another measure of paper non uniformity is paper surface or thickness variations. Cassidy (Cassidy 2004) used digitized surface electron micrographs (SEM) obtain maps of paper cross sections, which exhibited non-uniformity in their thickness. The bottom half of the figure 2.10 shows one such cross-section of a paper sheet obtained by SEM. Their modeling work demonstrated that such thickness variations could lead to non-uniformity in Xerographic transfer force, which could subsequently influence print density variations.

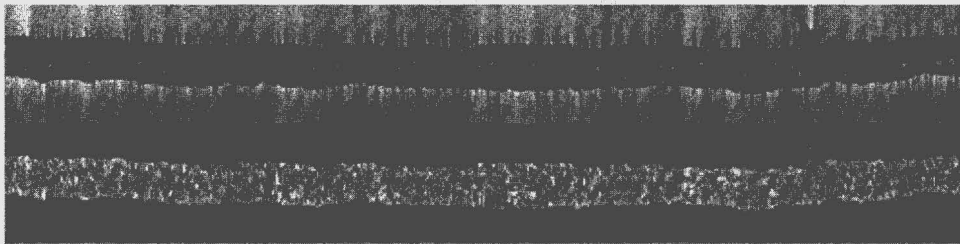


Figure 2.10 SEM cross-section (bottom) for a 7460 μm filled-paper substrate (copied from Cassidy 2004).

2.3.3.2 Pore Distribution

Paper is a network of fibres. The network of fibres embraces and creates a network of pores, and paper is thus a two phase system in which the pores and voids between the fibres are an important part of the paper structure. The experiments (Andrade 2005, Corte 1958) have proved that the pore distribution of a conventional paper is also non-uniformly distributed.

Thus, the microstructure of paper can be characterized in terms of a number of

stochastic variables, (hereafter referred to as fields because they assume different values at different positions in the paper): thickness variation, surface variations, mass density distribution (formation), filler distribution and pore distribution. These measured fields, as well as the fundamental mechanical and chemical properties of the individual fibers, completely determine the properties of paper.

2.3.4 Paper Structure Simulation

A typical paper sheet contains an order of ten fibres in the thickness direction. The fibre length is more than ten times larger than the sheet thickness. Thus a ‘two-dimensional random fibre network’ approximation is good for many purposes (Corte 1960, Bronkhorst 2003). However, for applications where the thickness, roughness or internal porosity variations are important, a three-dimensional (3D) paper structure is required.

The first successful 3D paper structure model was developed by Niskanen, et al. (Niskanen 1994). They started with a two-dimensional square lattice of linear size $L = 10, 100, 1000$. Periodic boundary conditions were applied. The fibres were initially straight beams of unit width and thickness, $w_f = t_f = 1$, and the emphasis was given to large fibre lengths $l_f \gg 1$.

Fibres were positioned and aligned in the two principal directions at random (Kirkpatrick 1981) in such a way that the local coverage c (number of fibres covering

the cell) was always an integer. A ‘bending flexibility’ T_f gave the largest allowed vertical deflection of the fibres from one lattice cell to the next. A high T_f through $T_f = [cw_f(WFF)]^{1/4}$, where c and WFF depended on experimental details. Measured values of the wet fibre flexibility (Paavilainen 1993) and known dimensions of paper-making fibres yield $w_f T_f \geq 1$. In the simulation, fibres were deposited independently, one after another, as if they were sedimenting from a dilute suspension. Each fibre was kept straight and parallel to the substrate until the first contact was made with the underlying network. Thereafter the fibres were deformed so as to lie as low as possible – not below the substrate – still obeying the deflection constraint T_f . Figure 2.11 shows a staircase pattern because of the finite width of real fibres.

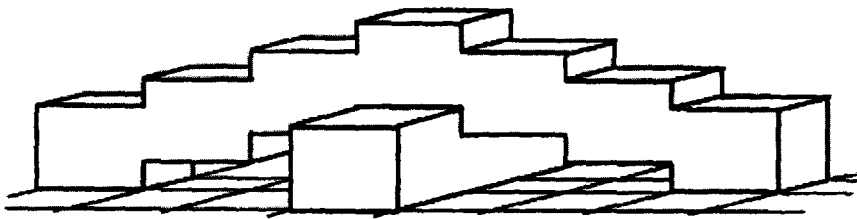


Figure 2.11 Two crossing fibres on the square lattice (copied from Niskanen 1994).

This model featured a 3D stacking of bendable fibers that could emulate various statistical properties of paper bulk and surface structure. However, it did not incorporate paper-press interactions, nor did it allow for a robust control on the spatial distributions of fibres during deposition.

More recently, Provatas, et al. (Provatas 2003) developed an extension of the model in Niskanen 1994, which incorporated a phenomenological local formation control parameter, distributed fiber dimensions and fiber orientations, fiber collapsibility and, *most importantly*, local, effective, elastic and plastic z-direction deformation of the paper surface and bulk due to paper-press interactions. This model is utilized in this work and will be introduced in detail in chapter 4.

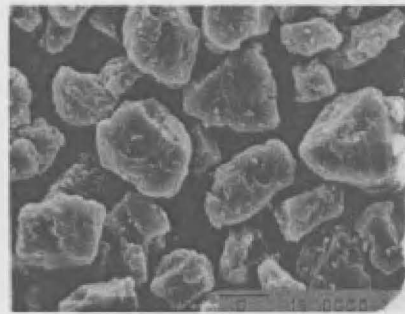
2.4 Physical Properties of Toner

2.4.1 Toner Fabrication

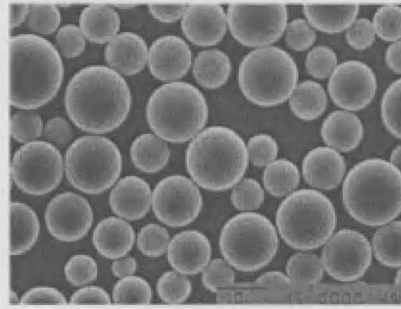
Commercial toner products are mainly composed of binder resin, colorant, and additives. They are mostly manufactured by the melt-mixing method. In general, the preparation process is as follows: colorants such as carbon black (or iron black) are first dispersed uniformly by blending into a melted thermoplastic resin; by extruding and cryogenic air-jet grinding, these are classified into the desired particle size distribution (PSD); finally, these are mixed with other additives, such as fumed silica, to obtain the final product (Grushkin 1992, Demejo 1992, Fox 1992, Fuller 1993, Mahabadi 1994).

The grinding and classifying in producing toners are energy intensive and of low efficiency. Thus, several polymerization routes have been proposed. (Yang 2003) Patented polymerization methods for toner preparation include suspension polymerization, emulsion polymerization, dispersion polymerization, interface/free

radical polymerization, and aggregation processes. All of these methods build the toner particle from droplets of monomers or micelles directly, which is distinct from the breaking down from bulk materials. Among them, the suspension polymerization method has the advantages of preparing toner particles with nearly perfect spherical shape and being less stabilizer adsorption in comparison to emulsion polymerization (Yuan 1991, Vivaldo-lima 1997).



(a) Pulverized toner



10 μ m

(b) Polymerized toner

Figure 2.12 SEM photograph of (a) pulverized toner and (b) polymerized toner (copied from Grushkin 1992).

Figure 2.12 compares the toner particles made by two different schemes: (a) grinding and classifying technique (pulverized toner); (b) polymerization technique (polymerized toner) (Hasegawa 1999).

2.4.2 Size of Toner Particles

The commercially used toner particles in standard Xerographic processes are produced using a grinding and classifying technology. All the components of the toner particles are molten, solidified and then ground to the desired particle size. By using this process, a diameter distribution of toner particles is obtained. A normal distribution with the standard deviation σ can be used to characterize the toner size distribution. According to Hoffmann 2004, the “probability density function” can be expressed as below:

$$q(d) = \frac{1}{\sqrt{2\pi}} e^{-\frac{1}{2}\left(\frac{d-d_{50,3}}{\sigma}\right)^2} \quad (2.15)$$

Where d is the diameter of toner particles; $d_{50,3}$ is the average diameter.

A log-normal distribution is often used, since the particle size can not be negative value. After making the transition, equation (2.15) becomes

$$z = \frac{1}{\sigma} \ln \frac{d}{d_{50,3}} \quad (2.16)$$

Coulter Counter, which uses the Coulter principle, can be used to measure the toner particle size distribution. The toner particles are dissolved in a weak electrolyte solution. The suspended solution flows through a small aperture, which is set up by two parallel electrodes. And the voltage is applied between the two electrodes, by which there is an electric field in the aperture. As particle solution passes through the aperture, each particle will change the impedance ΔR between the two electrodes.

From Coulter principle, the value of ΔR can be related to the particle sizes (Hunter 1995):

$$\Delta R = \frac{4d^3}{1.5\pi D^4} \rho_0 \left(1 - \frac{\rho_0}{\rho}\right) \quad (2.18)$$

Where d was defined as the particle diameter, D is the aperture diameter, ρ_0 the density of the liquid and ρ the density of the particle.

Thus, the number and size of particles suspended in the electrolyte can be obtained. And the distribution of the toner particles can be calculated from the software of Coulter Counter. Figure 2.13 shows the resulting distribution of a measurement of a sample of the toner from Hoffmann 2004

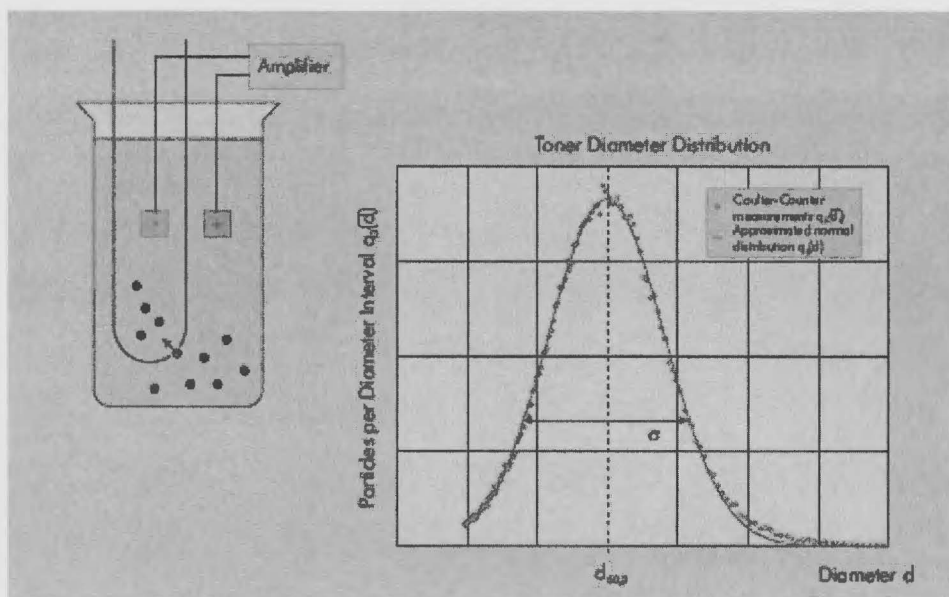


Figure 2.13 Coulter Counter (copied from Hoffmann 2004).

In our modeling work, we mainly study the effect from paper heterogeneity. Thus, the transferred toner particles are assumed to be the same size, 10 μm in diameter, which are mostly used for commercial Xerographic printing. But in future work, we suggest that the distribution of toner particles should be included in the modeling platform.

2.4.3 Charge of Toner Particles

Toner particles are conventionally charged by contact electrification in Xerographic printing, also named as Triboelectrification (Law 1994, Schein 1999, Hirakawa 1996). The amount of charge on toner particles thus obtained (Schein 1996) is the primary material property that determines the behavior of any Xerographic development system and toner transfer process.

Toner charge distribution can be determined by using toner-charge-spectrometer (Kuttner 1998). Figure 2.14 (copied from Hoffmann 2004) shows the principle of toner charge examination. Toner and carrier particles are triboelectrically charged with a magnetic stirring unit inside a developer. Then by using sharp air jet, toner particles are separated from the carriers. The charged toner particles are airborne with almost homogeneous velocity and move into the measurement chamber. Inside chamber, there are two diagonally aligned electrodes, by which the toner particles will be attracted with a perpendicular electrical field. Finally, these deflected toner

particles are deposited onto one of these two electrodes, on which there is a layer of thin film. The thin film can be removed and evaluated afterwards using an optical microscope combined with image analysis software. The diameter and charge of the particles can be obtained from their position on the thin film.

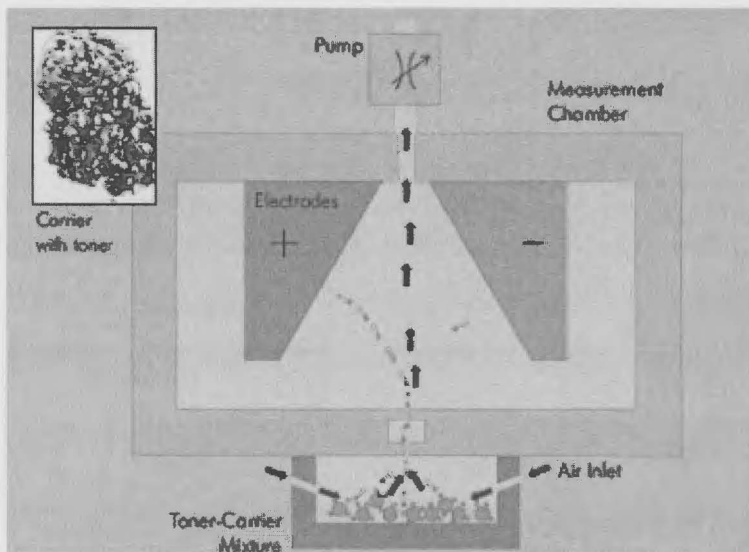


Figure 2.14 Schematic charge test (copied from Hoffmann 2004).

Hoffmann’s work (Hoffmann 2004) concluded that it is diameter of the toner particle which mostly controls the charge distribution. Their work proved that the charge distribution of the smallest particles shows a nearly perfect Gaussian distribution. However, for particles with larger diameters, “an increasing part of correctly charged negative particles appears”. Fig. 2.15 shows the charge distributions for different diameter classes. At lower right of the figure, they proved that an

exponential distribution replaced the negative side of the Gaussian distribution for toner particles with larger sizes.

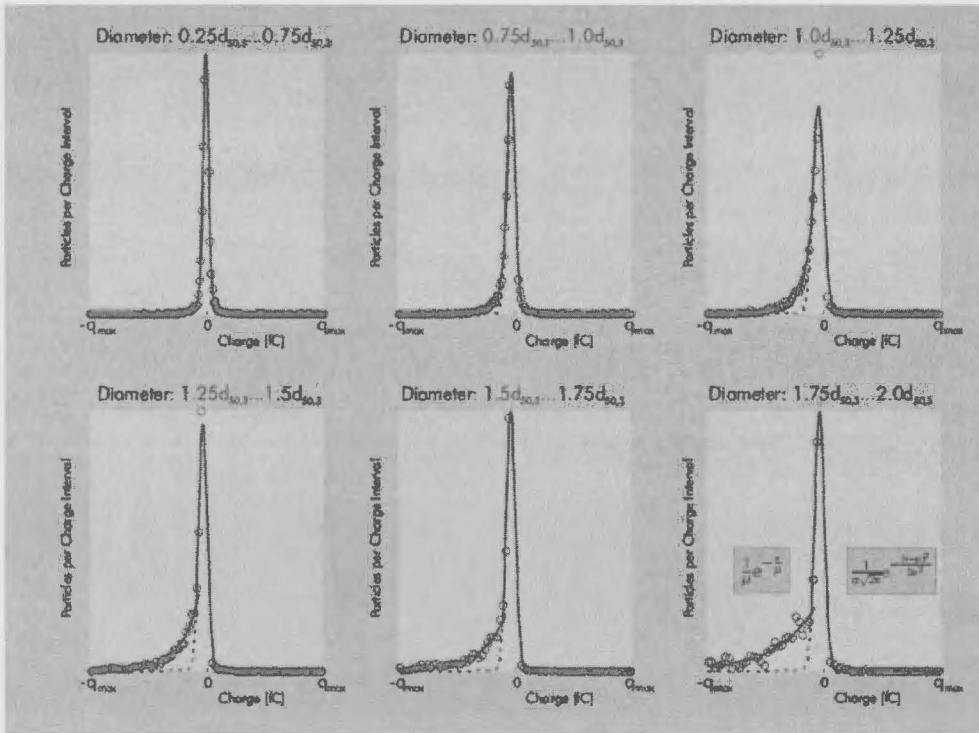


Figure 2.15 Experiments on charge distribution (copied from Hoffmann 2004).

The investigation of the complex charging processes and charging theory is beyond the scope of this work. We will hereafter assume a uniform toner charge distribution of 32.43 C/m^3 present in the toner layer. This is related to the commercially used toner particles (toner sizes are of the order of $10 \text{ }\mu\text{m}$ and with a charge of $1.0 \times 10^{-14} \text{ C}$) (Rimai 2001). While the examination of non-uniform toner distributions was outside the scope of this thesis, our modeling platform can

implement different toner distributions once these are known.

2.4.4 Toner Adhesion Force

In the toner transfer process, particle adhesion can play a significant role in the Xerographic process. More specifically, it is the complex interactions between electrostatic forces (particle-to-particle or particle-to-charged substrate, such as paper) *and* electrodynamic forces (i.e. van der Waals interactions between toner and photoreceptor or paper) that govern this process.

2.4.4.1 Measurement of Adhesion Force

The tape measurement could be used to estimate the average adhesion force (George 1996). A tape strip was pressed onto the toner particles layer under a certain pressure for a specified time. Then the tape was removed and the amount of detached toner particles could be obtained by measuring the optical density. However, this method did not give the exact value of toner adhesion force. For a better measurement of the adhesion force, there are three methods commonly used:

1. Centrifuge measurements (Howard 2000): In Figure 2.16, toner particles are put onto the sample substrate in the test tube. With the rotation of an ultracentrifuge, toner particles will be detached from the substrate. The adhesion force can be obtained by the accelerating force, and the transferred toner properties can be

measured by image analysis software.

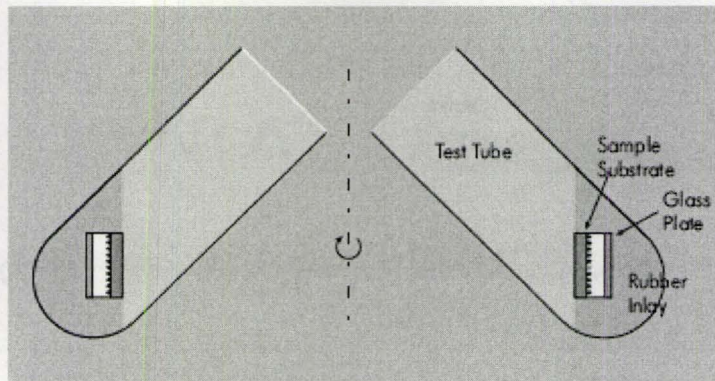


Figure 2.16 centrifuge measurements for adhesion force (copied from Hoffmann 2004).

2. Atomic force microscope (AFM) measurements (Gady 1996): This method is good for measurement of adhesion force for a single toner particle with some known radius and amount of charge. The toner particle is fixed onto an AFM cantilever. The adhesion force between any toner particles and any substrate with some specific properties can be obtained repeatedly. (Figure 2.17, 2.18)

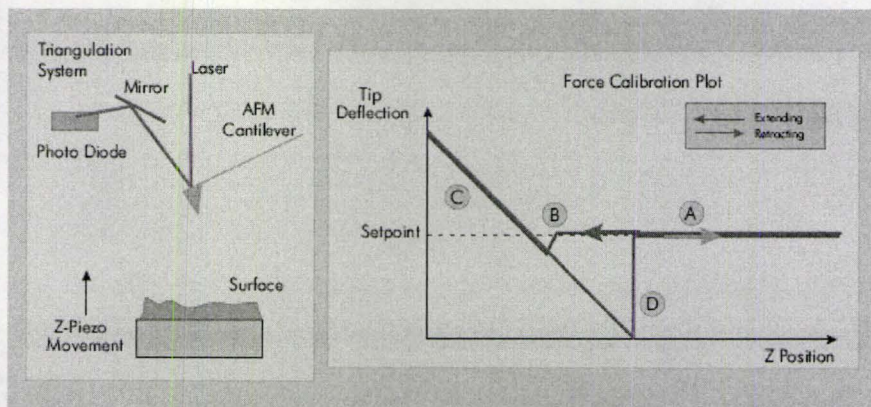


Figure 2.17 AFM measurements for toner adhesion (copied from Hoffmann 2004).

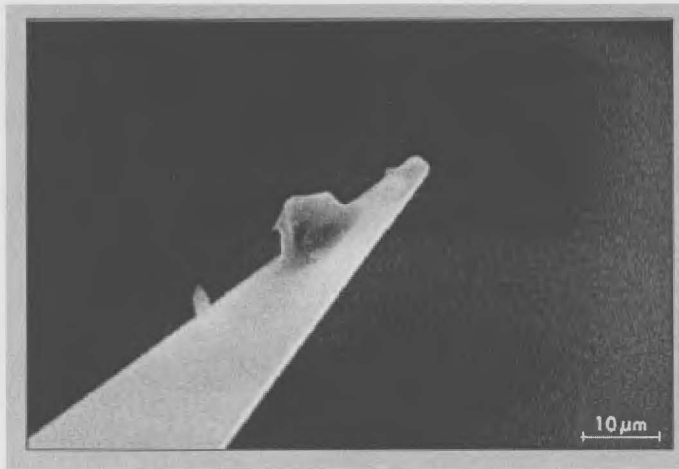


Figure 2.18 Toner on AFM cantilever (SEM image) (copied from Hoffmann 2004).

3. Electrostatic detachment measurements (Rushing 2001): Charged toner particles are deposited onto the test substrate. By applying the electric field forces these charged particles will be dragged away from the test substrate. By varying the magnitude of the electric field, the different amount of toner particles detached from the test substrate can be measured. (Figure 2.19)

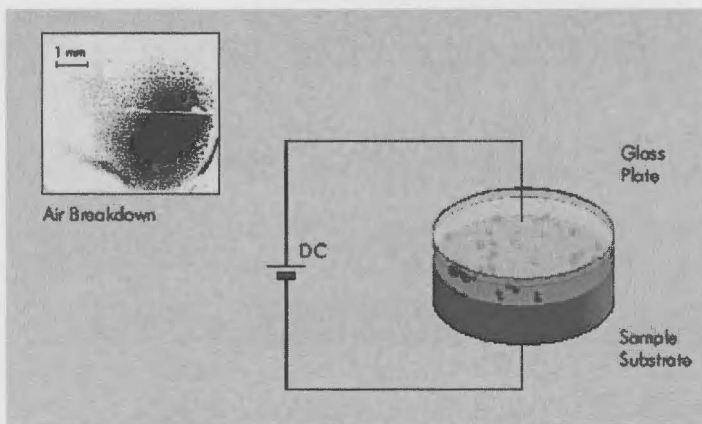


Figure 2.19 Electric field detachment measure of toner adhesion (copied from Hoffmann 2004).

The centrifuge measurement can be used to measure the adhesion force for large quantities of toner particles, especially for those with some distribution of particles size. It is important since the magnitude of the adhesion forces differ widely (up to three orders of magnitude) with different sizes of toner particles. This method is good to obtain the average adhesion force for some kind of commercial toner products. In contrast, the AFM method can examine only one single particle at a time. However, it is easy to study the adhesion force for toner particles with different size on different substrates. Although, the AFM method is the best method to study the adhesion theory, yet it is difficult to obtain the average adhesion force for large amount of toner particles. The method of electrostatic detachment measurement can only be used to examine the charged particles. It offers a good way to measure the relation between the adhesion force and the amount of charge on the toner particles.

We briefly review here several previous works comparing various measurements on toner adhesion forces. Hays found that the separation force needed to detach 13 μm diameter toner particles from 250 μm diameter nickel carrier particles was about 500 nN (Hays 1995). Mastrangelo (Mastrangelo 1982) used centrifugation to measure the separation force of toner particles having diameters between 6 μm and 20 μm . He found that the removal force for 10 μm diameter toner particles from a photoconductor was approximately 1000 nN. Lee and Ayala (Lee 1985) found that the removal force of 20 μm toner particles is between approximately 1000 and 2000 nN. Lee and Jaffe (Lee 1988) reported similar removal forces, (between 100 and 8000 nN) for 20 μm

diameter toner particles.

2.4.4.2 Toner Adhesion Theory

In toner transfer process, an electrostatic field is applied to toner particles to generate the electrostatic force (electrostatic toner transfer force), by which the toner particles will be detached from the photoconductor surface and transferred onto paper surface. To successfully transfer the toner particles, this electrostatic force must be sufficiently strong to overcome the adhesion force which holds the toner particles to the photoconductor. The electrostatic transfer field E is applied to the toner particles with a radius R and charge q . The electrostatic transfer force F_T can be calculated as below:

$$F_T = qE \quad (2.19)$$

(The electrostatic field is determined by the applied voltage and the sandwiched structure in Figure 2.2)

The adhesion force, which holds the toner particles onto the photoconductor have two origins:

The first is an electrostatic imaging force F_I caused by the charged toner particles. The toner particles generated image charges within the photoconductor and this force is given by (Hays 1996)

$$F_I = -\beta \frac{q^2}{4\pi\epsilon_0(2R)^2} \quad (2.20)$$

the constant β is the polarization factor, and its value is still under investigation (Rimai 1990, Rimai 1993).

The second terms of adhesion force comes from surface interactions, such as van der Waals forces. From Johnson-Kendall-Roberts (JKR) equation (Johnson 1971), this surface interactions force can be expressed as F_s , which is given by the equation as below

$$F_s = -\frac{3}{2}\omega_A\pi R \quad (2.21)$$

Where ω_A is the thermodynamic work of adhesion and it depends on the surface free energy γ_{TS} as $\omega_A = \gamma_T + \gamma_S - \gamma_{TS}$.

Therefore, the total adhesion force F_A could be obtained as below

$$F_A = -\frac{3}{2}\omega_A\pi R - \beta \frac{q^2}{4\pi\epsilon_0(2R)^2} \quad (2.22)$$

Gady's work (Gady 1999) studied a toner particle on an organic substrate, they obtained ω_A as 0.05 J/m^2 . Thus, for a spherical toner particle with diameter of 10 μm , they estimated F_A to be around 1200nN.

Schein and et. al showed that "Replacing the toner charge with a single point charge in the center of the sphere is only true for an isolated sphere". However, in the toner transfer process, the spherical toner particles are in contact with a

photoconductor plane, hence the quantized nature of the charge should be taken into account and simply applying the Gauss's law is no longer correct in equation (2.22). Schein and et. al used finite element analysis to model the charge distribution by a uniform distribution of charge points along equally spaced annuli and the image charges are located below the conductive plane by the usual method (Stanley 2004).

According to their work, the adhesion force, which includes two parts: electrostatic force and van der Waals force, could be obtained as below:

$$F_A = -\frac{1}{4\pi\epsilon_0} \frac{Q^2}{(2R)^2} - \frac{3}{2} \omega_A \pi R - n_p \frac{4}{\pi} \frac{1}{4\pi\epsilon_0} \frac{Q^2}{(2R)^2} \quad (2.23)$$

where R is the radius of toner particles, Q is the toner charge, n_p is the number of contacts between toner particles and conductive plane, and last term is named as the proximity force.

Actually the complex shapes, size distribution, surface additives and other properties of toner particles will all complicate the value of toner adhesion force. Therefore, the adhesion force used in our model is treated as a generic "adhesion force" and estimated from published experiments (Hays 2005, Zhou 2003, Takeuchi 2006, Gotzinger 2004, Schein 2004, Dejesus 2006, Rimai 2003) and theoretical studies (Gady 1998, Czarnecki 2004, Schein 2005, Schein 2004, Rimai 2004, Rimai 2001, Rimai 2002, Wright 2005, Rimai 2001, Goel 1975).

Chapter 3

Modeling Paper Structure

As mentioned in the literature review, the first successful stochastic model of paper structure was the PAKKAA model (Niskanen 1994). Their model combined many features of fibre flexibility and deposition that went into the development of a paper web. The PAKKA model was able to capture some statistical features of paper (Nilsen 1998), including bulk properties and fluid flow through paper (Rasi 1999). In a recent work by Provatas and Uesaka (Provatas 2003), another stochastic fibre network model was introduced, which extended the PAKKA model. The new features of Provatas's model include incorporating local formation control, distributed in-plane fibre orientations and fibre dimensions, non-uniform fibre collapsibility and, *most importantly*, local paper consolidation and paper-press interactions. As mentioned above, one of the major objectives of this thesis will be to use the model of Provatas et al as a “front end” into a new model of toner transfer. The ability to change paper density and surface characteristics, will enable, for the first time, the ability to understand and predict how the patterning of paper constituents affects toner transfer.

3.1 Introduction to 3D Fibre Network Model of Paper

Paper web (i.e. fibre network) generation begins with random fibre sedimentation, and also depends on the mechanical features of fibres, such as bending and collapse, which occur during the initial stage of paper forming.

3.1.1 Fibre Deposition

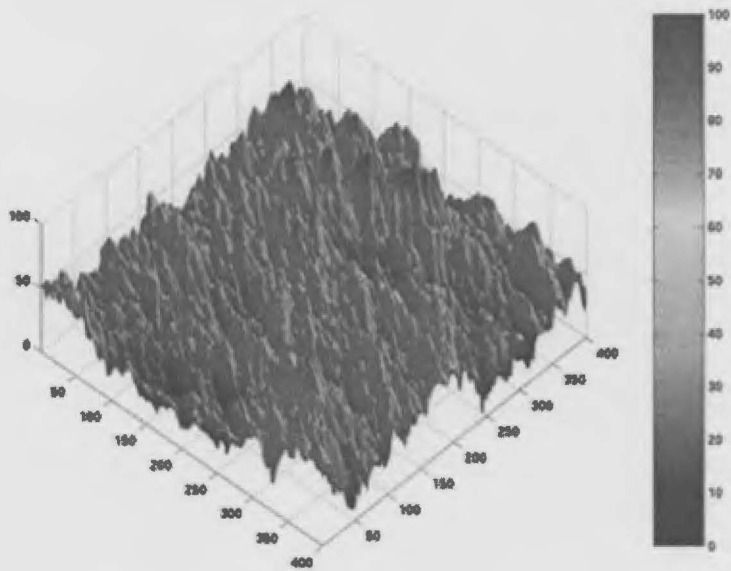
In the model, the initial fibre web is constructed by depositing, one at a time, particles (fibres, fillers or fines) onto a 3D-fibre web situated in the x-y plane. Particle centers are distributed randomly within a system of dimensions $-S_x < x < S_x$ and $-S_y < y < S_y$. Their angle of orientation θ is distributed according to an angular distribution $f(\theta)$, it can be either uniformly distributed in the range $[-\pi/2, \pi/2]$, which corresponds to the case of handsheet, or follow some anisotropic angular distribution functions by which to simulate Machine made papers (Dodson 1994).

Fibres are modeled effectively as rods of length L , width W and height H , where L , W and H are each derived from a distribution function specific to a fibre species. Fibres also possess a cell wall thickness δ , defined implicitly through their coarseness (mass/length of a species of fibre), fibre dimensions and cell wall density.

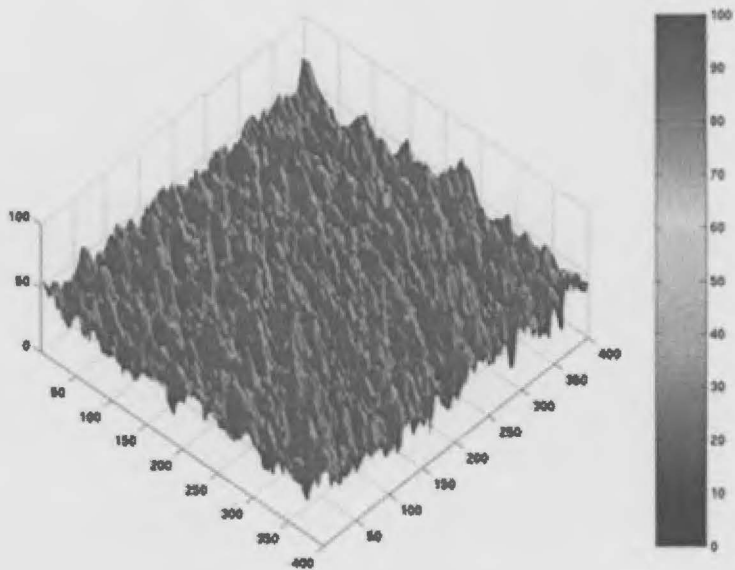
3.1.2 Fibre Interactions

In order to simulate the effect of fibre-fibre and fibre-web interactions, a Monte-Carlo fibre deposition rule is defined in this model. A deposition event is always accepted if a fibre is deposited on a section of the web whose mean height is $\zeta \leq \alpha \bar{S}$, where ζ is the average thickness of the paper over the projected area of the deposited fibre, α is a constant in the range $[0,1]$, and \bar{S} is the average thickness of the entire paper. A deposition event not satisfying this condition is accepted only with a probability $0 < \rho < 1$, known as the acceptance probability (Provatas 2000). If the fibre is not accepted under these conditions, the deposition trial is repeated until it is accepted. Particle deposition occurs until the required basis weight of the simulated paper is attained.

Varying α and ρ can give different paper formation and, through these parameters, the degree of fibre flocculation and mass density uniformity is controlled in simulated paper. The choice $\rho = 1$ produces uniformly-random fibre networks for all values of α , and as $\rho \rightarrow 0$ the network can be made progressively more uniform (ultra-uniform) as α decreases. Figure 3.1 shows paper structures with different formation.



(a)



(b)

Figure 3.1 Paper surfaces with different formation (a) Uniformly-random fibre networks ($\rho = 1.0$); (b) ultra-uniform fibre networks ($\rho \rightarrow 0, \alpha = 0.5$). (Units of axis: $5 \mu\text{m}$)

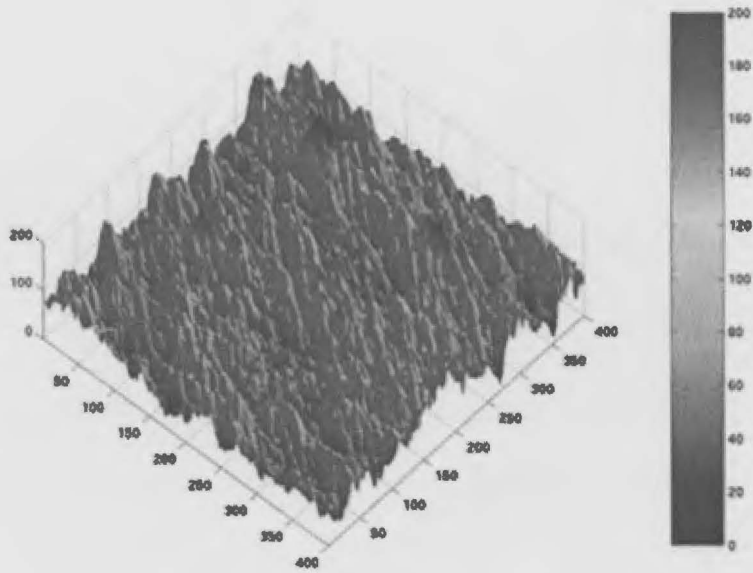
3.1.3 Fibre Collapse and Flexibility

During deposition of the initial fibre web, prior to consolidation, fibres undergo bending and some collapse due to the draining force. These two processes are related to fibre mechanical properties and a pressure exerted on the fibres in the forming section.

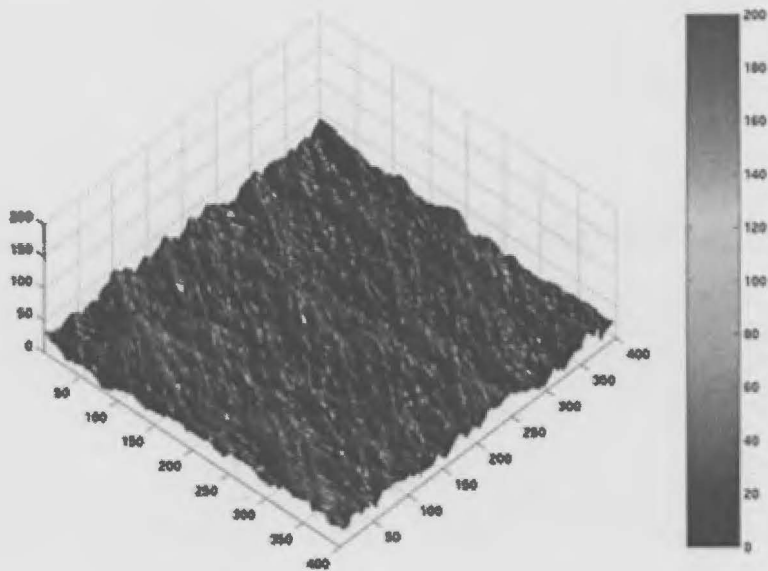
Deposited fibres are represented by a collapsed thickness $h = H / C_i$. The degree of collapse is represented by C_i and depends on a fibre's cross sectional area, collapse due to drainage pressure during deposition (Jang 2002, Jang 2001) or due to the prior treatment of fibres. Fig 3.2 shows paper structures with different fibre collapse indices. The mathematical formalism of C_i is expressed as

$$C_i = 1 - \{1 - \exp(-[\frac{W}{\delta} C(\theta_{FA}) f]^2)\}^{1/2} \quad (3.1)$$

Where f , we assume, is proportional to a uniform pressure acting on the top surface of all fibres during deposition, $C(\theta_{FA})$ is a dimensionless function of the cell wall fibril angle θ_{FA} , representing the effect of the fibril angle on the transverse Young's modulus of a fibre (Fang 2001).



(a)



(b)

Figure 3.2 Simulated paper surfaces with (a) Low fibre collapse index ($C_f = 1.0$); (b) High fibre collapse fibre index ($C_f = 3.0$) (Units of axis: 5 μm).

During deposition, fibres also bend around the developing paper surface, denoted by

$$z = S(x, y) \quad (3.2)$$

Where z is the surface height of the developing paper web. To obtain the new surface after bending, first the fibre is discretized in units of a *numerical discretization* length scale Λ , which is in this work set equal to 5 μm in the model. Discrete positions along the fibre are denoted by (i, j) , and the height of the fibre is denoted by $Z_B(i, j)$ (measured relative to the plane onto which the fibre network is being formed). Each point of the fibre is pressed into the z direction as low as possible such that it does not move through the existing paper surface (described by Equation 3.3), and such that any two neighboring points (i, j) , and (i', j') on the fibre satisfy

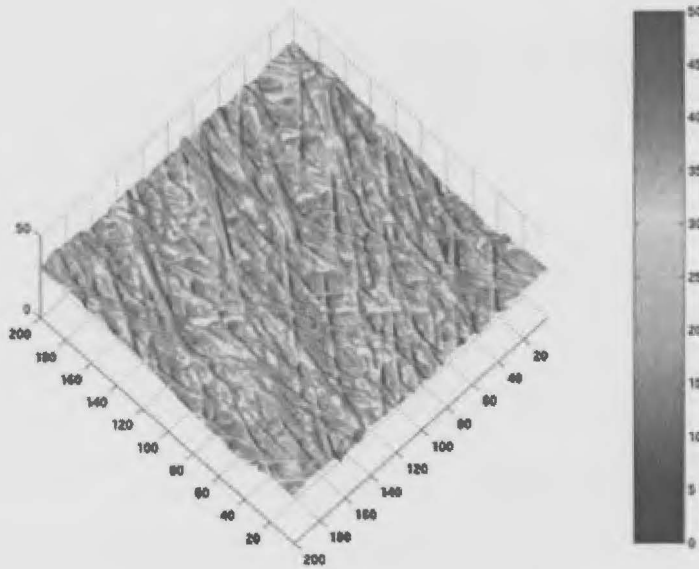
$$\frac{|Z_B(i, j) - Z_B(i', j')|}{h} \leq T_f \quad (3.3)$$

The specific form of the flexibility parameter T_f is given by

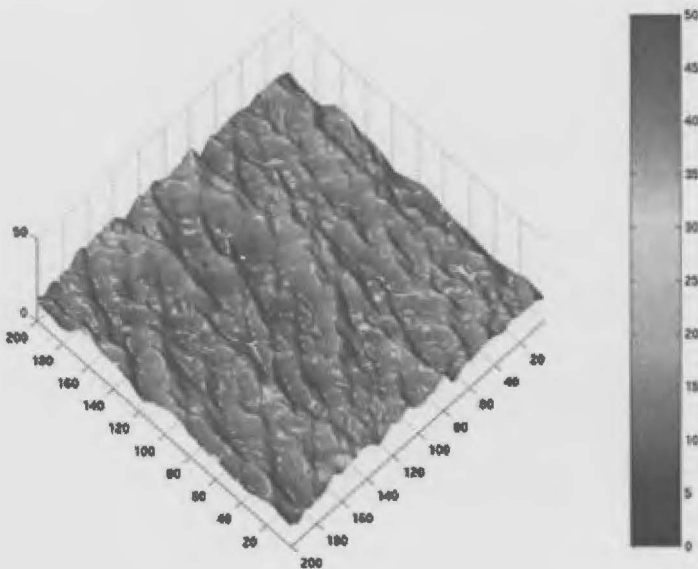
$$T_f \approx \frac{f' \Lambda^4 C(\theta_{FA})}{h^4 [1 - (1 - \frac{\delta}{W})(1 - \frac{h}{W})^3]} f \quad (3.4)$$

where f' is a dimensionless geometric parameter related to the deviation of a typical fibre in the network from a perfect beam element (Landau 1959, Provatas 2003).

The flexibility criterion in Equation 3.4 is empirical, but can be related to the mechanical properties of the fibre in bending. Fig 3.3 shows paper surfaces formed with two different values of fibre flexibility.



(a)



(b)

Figure 3.3 Simulated paper surfaces with different fibre flexibility (a) stiff fibre network ($T_f = 0.1$); (b) flexible fibre network ($T_f = 1.0$). (Units of axis: $5 \mu\text{m}$)

3.1.4 Consolidation of Simulated Paper Webs

After fibres are deposited, the paper web thickness is reduced in the z-direction due a wet and dry end pressing processes. In general this pressing process is far too complex for any model to accurately capture without the need for very complex computing methodologies, hydrodynamics, constant mechanics. Our model aims to capture the net effect of the paper web consolidation through a simple spring-based model for affecting a z-direction compression model of paper. The model builds in several empirical controls for emulating the effective elastic and plastic deformation the paper experiences from the point after deposition to the final product. It should be noted that this approach is not correct for describing paper making but is suitable for generating “virtual” (and realistic in the sense of stochastic geometry) paper templates for end use in a Xerographic simulator.

When the paper is pressed, particularly during printing, it behaves locally very much like a cellular material. Moreover, the highly disordered state of its constituent fibres, its small thickness relative to spatial variations of its in-plane mass distribution, as well as the empty space within fibres serves to damp stress propagation in the x-y direction and limit its influence to distances quite close to the point of stress at the surface of the paper (Rodal 1983, Gibson 1988, Garboczi 1995).

Exploiting these properties, the paper structure model defines a short-range cutoff ξ , which defines the limit of lateral influence of a concentrated stress at some point.

The [simulated] paper web is then *coarse grained* (i.e. homogenized) into a series of independent regions of lateral (i.e. in-plane) extent ξ . The precise value and definition of the length scale ξ are still unknown. A reasonable estimate is to make ξ equal to the decay range of the two-point mass-density correlation function, with an upper bound set by the average paper thickness. This hypothesis will be examined in a later chapter of this thesis.

Each region of the paper is treated as independent cellular material (“spring element”) of in-plane size $\xi \times \xi$, with a z-direction *tangent modulus* $E_{\xi}^T(x, y)$, which is a function of the local mass density lying within the $\xi \times \xi$ area. When the paper is incrementally pressed, each independent spring undergoes a corresponding z-direction strain increment.

The strain created in each spring is then transferred homogeneously to the corresponding fibre segments that pass through the “spring’s” $\xi \times \xi$, domain. In so doing compression of the paper and paper surface can be simulated after the initial paper web has been deposited. This process is only expected to be accurate on length scales greater than ξ , which is still many times greater than some of the common printing defects.

To simulate the paper compression process, the first information required is the elastic modulus affecting compressibility over the local region ($\xi \times \xi$) of a given “paper spring”, denoted $E_{\xi}(x, y)$ (i.e. $E_{\xi}^T(x, y) = E_{\xi}(x, y)$). The simplest description

of local paper compression can be modeled by the piecewise elastic-plastic stress-strain behaviour seen in cellular materials. It has been found that the compressive modulus of a wide variety of cellular and porous materials is described, to a high accuracy, by a function of their local density as

$$E_{\xi}(x, y) = E_c \left(\frac{\rho_{\xi}(x, y)}{\rho_c} \right)^m \quad (3.5)$$

where ρ_{ξ} is the local mass density, ρ_c is the density of the cell wall and E_c is the Young's modulus of the cell wall. The value of m is presently unknown.

For paper making, pressing, *particularly during wet pressing*, involves plastic deformation of the paper fibres due to the plastic collapse and buckling of individual fibre walls. In this case the surface does not recover much from the strain of initial compression (Roberts 2000). Plastic compression of our virtual paper is modeled via an effective non-linear stress-strain curve using the local tangent method (Yamauchi 1989). Specifically, when the stress in a local paper “spring” exceeds a certain plastic collapse stress $\sigma_c = S_{PL} E_{\xi}(x, y)$, where S_{PL} is a constant, discussed below, we allow the local paper spring element to plastically flow according to the relation $E_{\xi}^T(x, y) = F_{PL} E_{\xi}(x, y)$, where F_{PL} is a constant satisfying $0 < F_{PL} < 1$ (also discussed below) and $E_{\xi}(x, y)$ is the initial modulus determined from Equation (3.5) using the local density of the paper web prior to compression.

When consolidation pressure is removed from the pressed paper web, in regions where plastic collapse occurred during initial consolidation, partial strain recovery

will occur. This is modeled by a linear stress-strain relationship whose slope is set to a factor F_{RE} of the initial elastic modulus, and the formalism is the same as plastic compression. The factor F_{RE} increases with larger consolidation loads, since the more fibres are collapsed the less they recover.

Subsequent to the initial consolidation (and partial recovery) described above, paper becomes “strain-hardened”. Since most of the fibres are completely collapsed, they will exert considerable pressure upon further application of pressure (such as further pressing during printing). Further compression in this regime is thus assumed to occur elastically, with a strain-hardened local modulus re-assigned to the local fibre “springs” of the network. In this case the higher density of consolidated sheets gives rise to a much higher modulus in this phase.

The parameters F_{PL}, S_{PL}, F_{RE} and m are not known for paper. And they vary depending on whether one characterizes them based on the initial mass distribution or incrementally as compression proceeds. They also will vary dramatically on whether we consider wet-pressing (what happens during the paper-making process) or dry pressing (what happens, say, when the Xerox photoconductor presses the toner layer onto the paper layer during printing).

In this work, we will model wet-end compressive deformation during forming of laboratory handsheets using *effective* choices of $F_{PL}, \sigma_{PL}, F_{RE}$ and m that give good agreement of our simulated paper structure with experiments reported below. For dry

paper compression, which occurs during printing, we will explicitly determine and use the stress vs. strain response of paper from new experiments, also reported later in this Chapter. This was done in two steps. First we conducted new micro-indentation experiments. Second, our experimental data was fit to a strain-hardening model and input into the paper structure code.

3.2 Experimental Validation of Fiber Network Model of Paper

We now turn our attention to experimental calibration and validation of the paper structure model described above. We will experimentally characterize the mass distribution (“formation”) and surface height distribution of laboratory-made handsheet paper samples. Using the two-point correlation function as a measure, the unknown parameters of the paper structure model will be effectively calibrated such as to reproduce the statistical structure of handsheet paper samples. The two-point correlation function is a statistical measure that relates the correlation of two measurable quantities (terms “field”) to their separation in space.

3.2.1 Laboratory Handsheet Preparation

Laboratory handsheet paper sample were prepared according to TAPPI (the Technical Association of the Pulp and Paper Industry) standards (TAPPI 2006).

Two species of fibres were used - hardwood bleached kraft pulp (HBK) and softwood bleached kraft pulp (SBK) in the ratio of 75:25 wt% to a total of 24 ± 0.5 g.

(Pulp & Paper TAPPI 1995) Pulp was immersed in 1500 mL of de-ionized water and torn apart while immersed into small pieces (approximately 30 mm²). The mixture was covered with aluminum foil and allowed to soak for a minimum of 4 hours.

After soaking, an additional 500 mL of water was added to the pulp for a total of 2000 mL, and transferred into a disintegrating container. A standard disintegrator was used and was run at 3000 rpm for 3 minutes and then transferred to the hand-sheet making apparatus (See figure3.4).

The fibres were drained and collected from screen. The handsheet was then separated in half in the thickness direction and broken into pieces about 10cm x 5cm and placed around the walls of the bin in the beating machine. The fibres were then beaten for 5 minutes at 15000 revolutions/minute. The beater was lifted and thoroughly rinsed to ensure minimum fibre loss, fibres were then collected and 2000 mL of de-ionized water was added. The suspension was re-disintegrated and diluted with de-ionized water to 8000 mL total (~0.3%). The mixture was allowed to sit over night.

When ready to form handsheets, the suspension was thoroughly mixed and divided into separate 400 mL beakers. During this separating stage, steps were performed as fast as possible to avoid fibre settling. (Note: 400 mL of water-fibre mixture is required for producing the standard 60 g/m² average density sheet, when preparing different densities this volume is varied between 200-600 mL). One 400 mL

mixture was then added to the standard 159-mm-diameter sheet machine and filled to set volume with de-ionized water see Figure 3.4.



Figure 3.4 Standard 159-mm-diameter sheet machine, opened to reveal mesh on which handsheet forms. (Courtesy of Dr. R. Pelton, Chemical Engineering department, McMaster University)

The suspension was then agitated for 10 seconds followed by settling for 10 seconds, the mixture was then drained. Two pieces of standard blotting paper were centrally put onto the drained handsheet with the felt, smoother side of the lower blotter against the wet sheet. The handsheet and blotting paper were couched for 10 seconds. The blotters were discarded, and the handsheet was fit onto the drying disc (mirror polished, 160 mm diameter) smoothly. The drying ring was put onto the disc with the rubber seating holding the sheet to the polished disc. Finally the handsheet was allowed to dry in the atmosphere of a 50% RH (Relative Humidity) and 23°C for approximately 24 hours.

Six different grades of handsheet paper were prepared (three pieces for every grammage grade). Their average grammage (basis weight), thickness and volume density are listed in Table 3.1. These samples will be used to validate the paper structure model and conduct the micro-indentation tests.

Table 3.1 Properties for six grades of handsheet sample

Samples	Standard Grammage g/m ²	Grammage (average) g/m ²	Thickness (average) (mm)	Volume density g/cm ³
200	30.30	30.48	0.050	0.610
250	37.88	36.00	0.080	0.450
300	45.45	45.97	0.102	0.451
350	53.03	-	-	-
400	60.60	62.41	0.123	0.507
450	68.18	-	-	-
500	75.76	76.78	0.125	0.614
550	83.33	-	-	-
600	90.90	92.45	0.195	0.474

3.2.2 Structure Analysis for Uncompressed Handsheet Paper

3.2.2.1 Formation Distribution-Beta Radiography

The classical method for estimating the variation of local mass (known as *formation*) is based on light transmission (Kallmes 1987). However, results from this method are influenced by non-uniformity in the light absorption and scattering

properties that depend on the sheet composition and compressive processing. In such cases, the distribution measured by light may depart from the actual mass distribution. In order to determine accurate representation of mass distribution, alternate irradiation sources such as Beta-rays and X-rays (more energetic sources) have been utilized. In our formation experiments, we used Beta-Radiographic Imaging, (Keller 1998) done in collaboration with Dr. Steven Keller's lab from Department of Paper Science and Engineering at State University of New York, Syracuse.

Formation is measured on our paper samples over an area of 10cm×10cm. Figure 3.5 shows an example of Beta-radiographic image for one of the handsheet paper (basis weight 36g/m²).

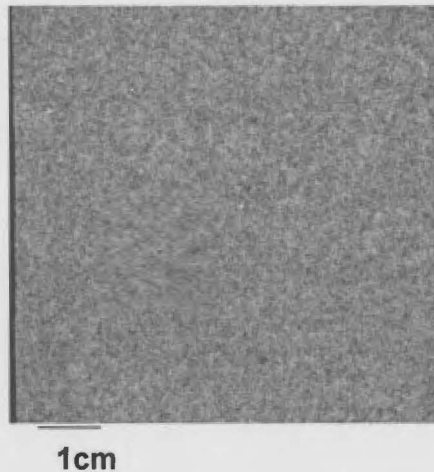


Figure 3.5 Beta-Radiographic image for handsheet paper (basis weight 36g/m²).

3.2.2.2 Surface Scan-Wyko Surface Profiler

The Wyko NT1100 surface profiler in the chemistry department (McMaster University) was used to conduct the 2-D surface scan, by which the experimentally surface height distribution for our samples is obtained.

There are two modes for this profilometer. One is Phase-shifting interferometry (PSI) which is for accurately measuring smooth surfaces, the other is called vertical scanning interferometry (VSI) which is for measuring rougher surfaces like paper (Wyko Menu).

The VSI mode was used in this thesis work. A white light beam, which is filtered by a “neutral density filter”, preserves the “short coherence length” from the original white light. Then this “short coherence light beam” illuminates onto the “test surface” through an “interferometer objective”. By the function of the “interferometer beam splitter”, half of the incident beam can be reflected to the “reference surface”. Finally, the beams, which are reflected from the “test surface” and the “reference surface”, recombine together and form the “interference fringes”. Figure 3.6 shows a schematic of an interference microscope (Wyko Menu).

When the measurement was conducted, the “reference surface” was moved by a “piezoelectric transducer (PZT)” with some small steps. This caused a phase shift between the reflected beams from the “test surface” and “reference surfaces”. The test facility measured the degree of “fringe modulation” or “coherence”. During the test,

the “interferometer objective” moved vertically and scanned the surface for different heights. The movement of the objective was controlled precisely from an “LVDT (linear variable differential transformer)”. Since the white light only preserved the “short coherence length”, “the interference fringes presented only over a very shallow depth for each focus position”. When the sample was just passed through the focus position, fringe contrast at this single sample point reached a peak. So at evenly-spaced intervals, the system scanned all the focus positions when the camera captured interference data frames (Wyko Menu).

With the test facility scanning downward, an interference signal for each point on the surface was recorded. The envelope of the fringe signal was demodulated by using a series of advanced computer algorithms. Finally the vertical position corresponding to the peak of the interference signal was extracted for each point on the surface. As a result, a data file showing all the waves for every sampling point was generated. By multiplying with the wavelength value (given as machine parameter), a surface profile for paper sample was obtained (Wyko Menu).

The lateral resolution we used in the test was 5 μm . Figure 3.7 shows a 3-D surface profile for a handsheet paper sample (basis weight 36 g/m^2).

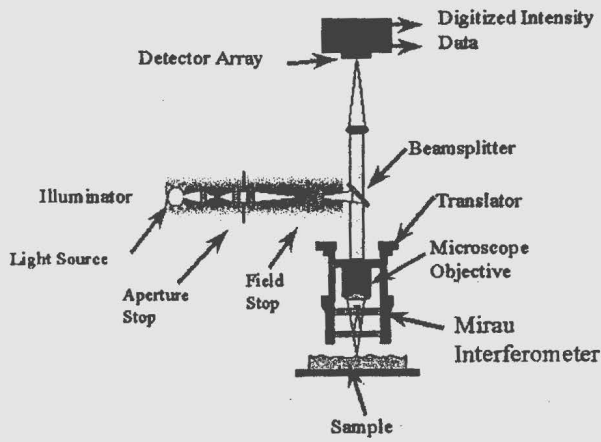


Figure 3.6 An interference microscope (copied from Wyko Menu).

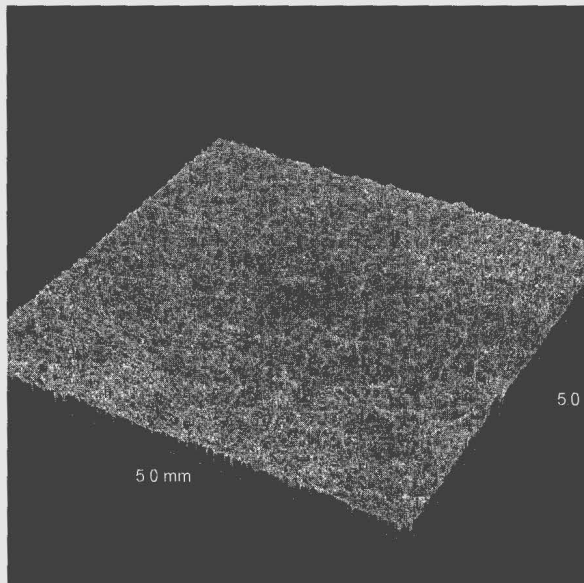


Figure 3.7 A 3-D surface profile for a handsheet paper sample (Basis weight 36 g/m²).

3.2.2.3 Characterizing Random Fields: Two-Point Correlation Functions

The so-called two-point correlation function (related to the auto-correlation function) is a well know and widely used measure in the paper science and condensed matter physics literature to quantify the spatial length scales that contribute to variation of various fields near the critical points of a phase transformations (e.g. divergence of magnetic domains near the critical point) (Chaikin 1995). We will borrow this methodology and apply it to our work. Here, the term “*field*” refers to mass density, surface height, etc. The definition of the two-point correlation function is

$$G(x, y) = \langle (m(i, j) - \langle m \rangle)(m(i + x, j + y) - \langle m \rangle) \rangle \quad (3.6)$$

Where $m(i, j)$ represents any one of formation, filler, surface height, print density fields. The indices i, j are discrete pixels in the zone where the data is defined. The variables x, y are also discrete, and are defined in the same range. The quantity $\langle m \rangle$ denotes the mean value of the field over the area of a zone. The angled brackets denote a spatial and ensemble average of the quantity in the brackets. For example, the product in equation (3.6) is spatially averaged over all points (x, y) in the zone. (For data running off the edges periodic boundary conditions are used). The ensemble average represents the average of the correlation over all zones in the sample.

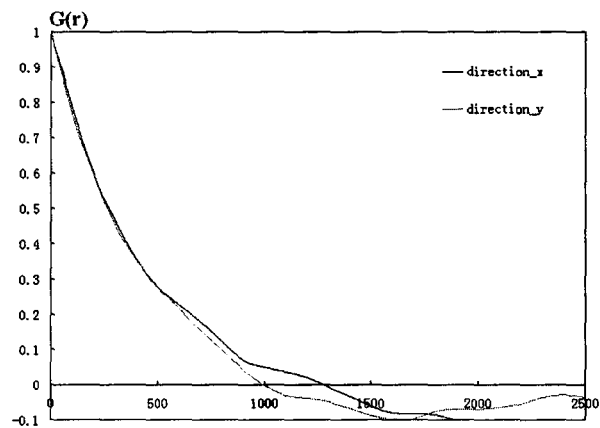
The value $G(x, 0)$ may be interpreted as the degree of correlation of the two points separated in the x -direction by a distance x . If the field has a periodic

fluctuation in the x-direction, $G(x,0)$ shows the same periodicity. If the field is completely “random” (no correlation between any two points, as in the case of white noise), $G(x,0)$ is zero except at $x=0$. The meaning of $G(0,y)$ is similarly interpreted in the y-direction. And likewise $G(x,y)$ represents the likelihood of correlation of two measurements separated by a distance of x in the x-direction and y in the y-direction.

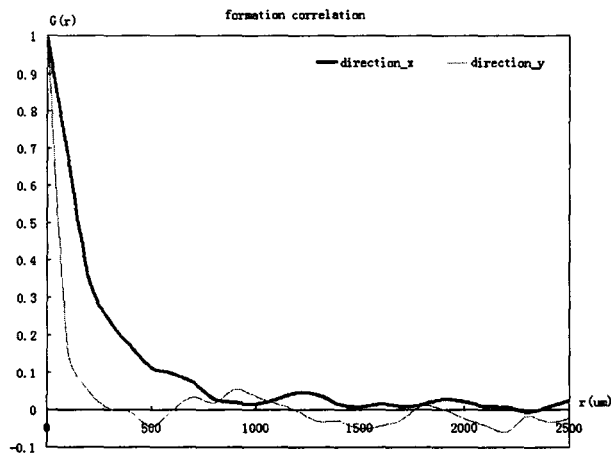
In isotropic samples $G(x,y) = G(\sqrt{x^2 + y^2})$, i.e., the correlation function depends only on distances between measured points. So, for some instance, if the paper is isotropic, only $G(x,0)$ is used to show the correlation of the paper sample. However, most paper is not isotropic, e.g. commercial sheets, and thus $G(x,0) \neq G(y,0)$, correlation function in both directions of paper samples should be examined. Figure 3.8(a) shows a typical two-point mass correlation function for a piece of laboratory made handsheet paper, (b) shows the two-point mass correlation function for a commercial paper. If G decrease very fast with distance, then distant points are relatively uncorrelated and the system can be seen as homogenized on this length scale. On the other hand, a slow decrease of G would imply that distant points have a large degree of correlation or influence on each other. The decay length of the correlation function will be used to identify the length scale over which two points of a given field are statistically correlated.

If two paper networks show the similar correlation function of surface height variation, mass density and filler distribution, it can be assumed that they have the

similar structure, at least in the statistical sense, which is the only correspondence we can expect between two stochastic structures. For ease of comparison, the normalized two-point correlation function is used, which is obtained by dividing the two-point correlation function with the covariance $G(0,0) (= \sigma^2)$.



(a)



(b)

Figure 3.8 Two-point mass correlation function of: (a) an area of laboratory made handsheet paper; (b) a piece of commercial paper. The two curves denote different directions in the paper.

In this work, we dealt with laboratory handsheet paper, which are isotropic since there was no moving wire and, as a consequence, no preferential wire direction during forming. Thus only $G(x,0)$ was used to characterize the structure and formation distribution. A FORTRAN program was written to compute $G(x,0)$ of mass distribution (formation correlation) and surface height distribution (roughness correlation), by inputting a 2-D array for mass or surface distributions.

Experiments of Beta radiography and surface profiler (Wyko NT1100) were conducted on handsheet samples. For each basis weight paper (30.48g/m², 36.00 g/m², 45.97 g/m², 62.41 g/m², 76.78 g/m², 92.45 g/m²), six measurements of mass density and surface height (i.e. roughness) variations were obtained (two areas are chosen on three samples of the same basis weight). The two-point correlation function from each area was obtained and these [six] functions were then averaged to obtain a representative statistic of the two-point correlation function for a given basis weight of our handsheets.

Table 3.2 shows the average roughness, mass density and the respective covariance of roughness and mass density (i.e. formation) for the 36.00 g/m² handsheets. Figures 3.9 and 3.10 show the individual and averaged two-point correlation functions of the mass density and roughness, respectively, of the 36.00 g/m² handsheets.

Table 3.2 Average properties for the chosen samples

Properties	Samples
Mean Mass	0.922mg (±5% water)
Mean Thickness	80um
Covariance of thickness	1.697
Covariance of formation (*10 ⁻³) mg m ⁻¹)	1.219

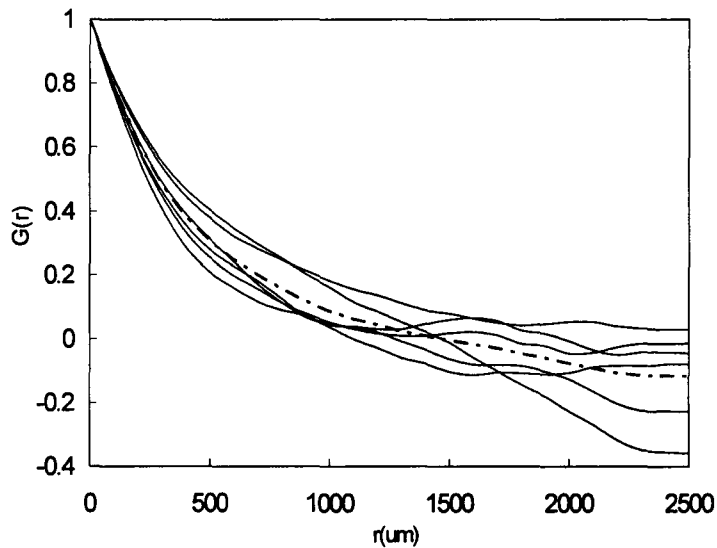


Figure 3.9 Plots of the two-point mass-mass correlation function (formation correlation) for six different samples (solid lines) and their average (dash-dot line) of the 36.00 g/m² handsheets. (Paper sampling area used in each correlation function was 5mm by 5mm).

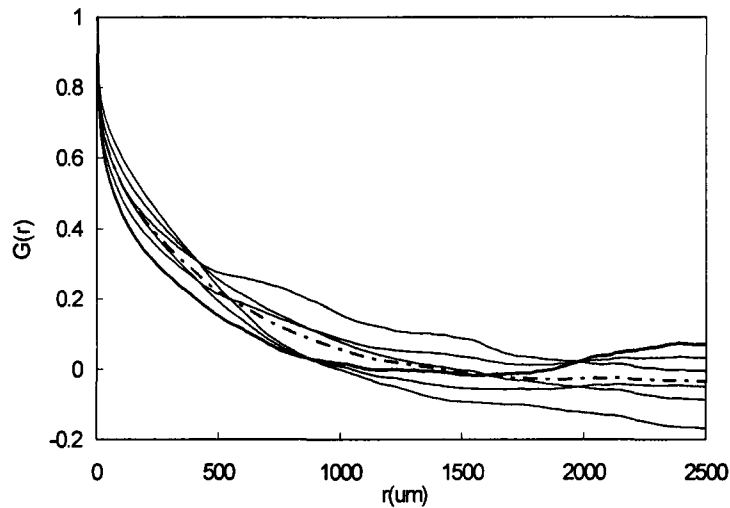


Figure 3.10 Plots of the two-point height-height correlation function (roughness correlation) for six different samples (solid line) and averaged result (dash-dot line) of the 36.00 g/m² handsheet. (Paper sampling area used in each correlation function was 5mm by 5mm).

3.2.3 Calibrating the Paper Structure Model from Experiments

We utilized the experimental data for our 36 g/m² handsheet to calibrate the parameters of the 3D fibre network model, as well as to validate the ability of our model to faithfully reproduce several key statistical measures of handsheets. Some parameters of the model, such as the fibre dimensions, their number and fibre collapse index are well known (and independent of basis weight) and can be determined from experimental data pertaining to the grades of fibres used in our handsheets. Those controlling fibre flocculation, fibre flexibility and wet-end compression (which do depend of basis weight) can not be easily determined experimentally, and must be

determined in an effective manner so as to achieve the correct agreement between simulated and real paper with regards to average properties and spatial correlations in the mass formation and roughness.

3.2.3.1 Fibre Dimensions and Number of Fibres

Typical average fibre dimensions can be obtained from literature (Scott 1995); these values can be used to calculate a number of important fields within the 3D fibre network model and are listed in Table 3.3.

Table 3.3 Experimental Fibre Dimensions (Scott 1995)

Species	Hardwood (μm)	Softwood (μm)
Average Length (μm)	1100	3300
Average Width (μm)	19	36
Wall Thickness (μm)	2.7	5
Coarseness (kg/m)	1.5×10^{-7}	1.0×10^{-7}

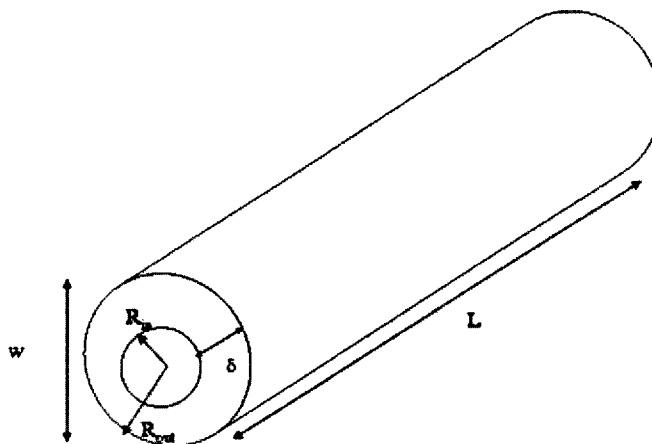


Figure 3.11 Schematic of Fibre Dimensions (The interior of the fibre is hollow and is termed the lumen) (Deng 1994).

The volume of a fibre is calculated as below:

$$\begin{aligned} V_f &= \pi R_{out}^2 L - \pi R_{in}^2 L \\ &= \pi \left[\left(\frac{W}{2} \right)^2 - \pi \left(\frac{W}{2} - \delta \right)^2 \right] L \end{aligned} \quad (3.7)$$

Mass of single fibre 1(hardwood fibre)

$$M_{f1} = \rho_1 \cdot V_{f1} \quad (3.8)$$

Mass of single fibre 2 (softwood fibre)

$$M_{f2} = \rho_2 \cdot V_{f2} \quad (3.9)$$

The number of fibres in a handsheet sample can be calculated using equations (3.10) and (3.11),

$$N_{f1} = \frac{75\%b \cdot A_p}{\rho_1 \cdot V_{f1}} \quad (3.10)$$

$$N_{f2} = \frac{25\%b \cdot A_p}{\rho_2 \cdot V_{f2}} \quad (3.11)$$

Where b is the basis weight (36 g/m^2), A_p is the area of the handsheet, N_{f1} and N_{f2} are the number of fibres for each species (standard is 75: 25 wt% hardwood: softwood).

Species 1 represents hardwood and species 2 represents softwood.

In the calculations above, the numerical discretization of fibres was set to be 5 μm . Using Table 3.3 and the above equations, the length of the hardwood fibre was 220 (in units of 5 μm), the width was 4 (in units of 5 μm), and the number of hardwood fibre in the 3D fibre network model was 9092; the length of softwood fibre

was 660, the width was 7, and the number of softwood fibre was 606. The total mass of the simulated fibre network was approximately 0.876 mg.

3.2.3.2 Fibre Collapse Index and Fibre Flexibility

After the beating process in handsheet making, some fibres were put onto the blotting paper and allowed to dry in the atmosphere under 50% RH (Relative Humidity) and 23°C for approximately 24 hours, which was the same as the drying condition in the handsheet making process. These fibres were characterized using scanning electron microscopy (SEM, Department of Materials Science and Engineering, McMaster University). (See figure 3.12)

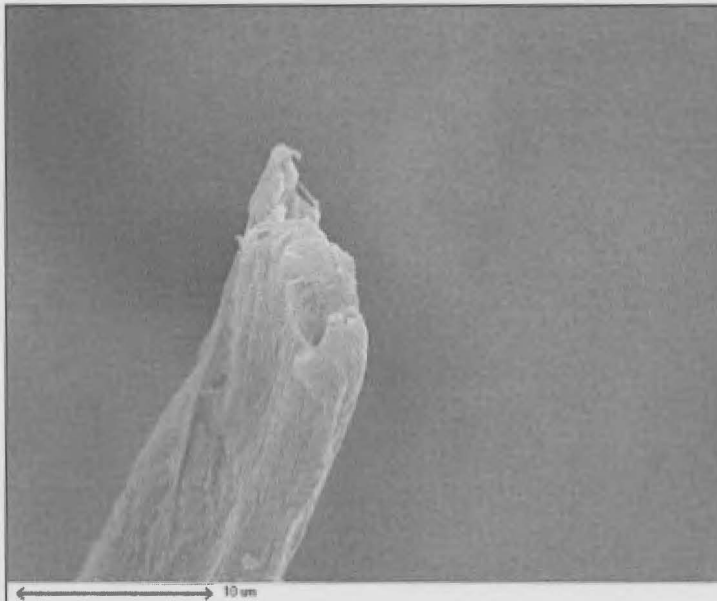


Figure 3.12 SEM image of hardwood fibre after beating.

From SEM data, we found that most of the fibres in the paper samples were nearly fully collapsed. And the collapse index defined in paper structure model can be calculated according to the fibre properties in table 3.3.

The collapse index is given in Equation 3.12,

$$C_i = H / h \quad (3.12)$$

Where h is the height of the collapsed fibre, H (thickness W) is the height of the original fibre, see figure 3.11.

For 100% fibre collapse we approximated the thickness as $h = 2 \delta$, and thus equation 3.12 gives:

$$C_i = H/2 \delta \quad (3.13)$$

According to table 3.3 and the above calculation, the fibre collapsibility index under fully collapsed condition is 3.5 for hard wood fibre and 3.0 for soft wood fibre. This is, of course, a simplification, since paper making is a stochastic process, and the collapsibility of hardwood fibres and softwood fibres will vary from fibre to fibre. We do not, however, expect this simplification to have too large an effect on the statistical fluctuations calculation of electrostatic transfer field.

The index of fibre flexibility describes the degree to which typical fibres bend during the deposition process. Figure 3.13 shows a pulp fibre, which has been soaked for about 24 hours. It is evident that the fibre is ribbon like, which is consistent with

the assumption that fibre is nearly fully collapsed. The image also shows that the fibre is flexible and easily bent. We thus assume that the index of the *flexibility of our model fibres must be close to or greater than 1*. (The index of fibre flexibility was defined in 3D fibre network model, value 0 means the fibre is completely inflexible, while a value 1 (or more) means the fibre is almost ribbon-like.)



Figure 3.13 Optical microscope image of fibre after beating

According to paper average thickness value, the flexibility T_f for hardwood fibre and softwood fibre were taken as 0.95, 0.85, respectively.

3.2.3.3 Paper Web Properties

From numerical experiments, it was found that the formation index α and ρ and the corresponding values of F_{PL} , σ_{PL} , F_{RE} (mechanical properties describing the elastic – plastic response of a $\xi \times \xi$ section of a simulated paper web, where ξ was described in Chapter 3) in the compression process will change the value of the final paper thickness (average thickness in table 3.2), mass distribution (Covariance of

formation in table 3.2), paper roughness (Covariance of thickness in table 3.2), formation correlation and roughness correlation.

We found that good correspondence between our simulated and experimental paper webs was obtained when $\rho=0.00001$ and $\alpha=0.01$, and the corresponding values of $F_{PL}, \sigma_{PL}, F_{RE}$ for the compression process, were set to 0.1, 0.15, 0.525, respectively.

Using these parameters above, a simulated 36g/m^2 basis weight paper was simulated from the 3D fibre network model. The simulated surface is shown in Figure 3.14. As a comparison, an experimental paper surface profile of one of our 36g/m^2 handsheets samples is shown in Figure 3.15. The mean statistical properties of our simulated and experimental samples are summarized in Table 3.4. The two-point correlation functions for formation and roughness from simulations and experiments are compared in Figures 3.16 and 3.17, respectively.

Table 3.4 Materials and statistical properties for simulated paper and experimental samples (Basis weight is 36g/m^2).

Properties	Samples	Simulation
Mean Mass	0.922mg (5% water)	0.876
Mean Thickness	80um	79.49
Covariance of thickness	1.697	1.698
Covariance of formation (* 10^{-3} mg m $^{-1}$)	1.219	1.266

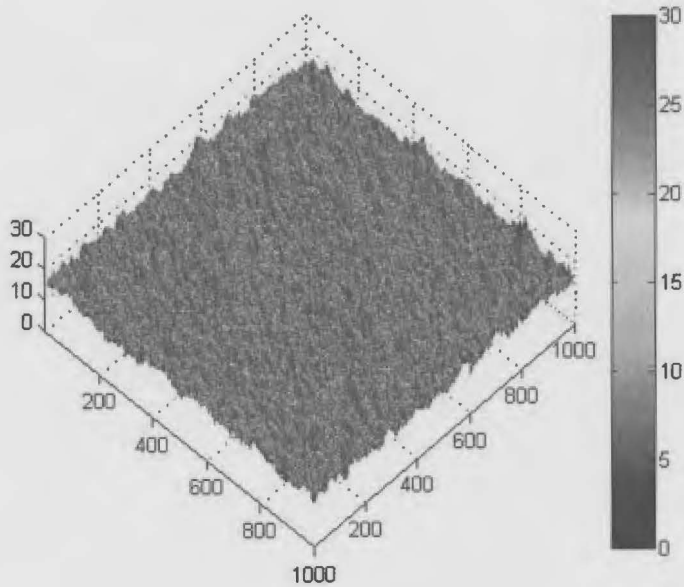


Figure 3.14 The simulated paper surface, the size in the x and y directions is 5mm by 5mm in unit of 5 μ m, with a minimum resolution of 5 μ m.

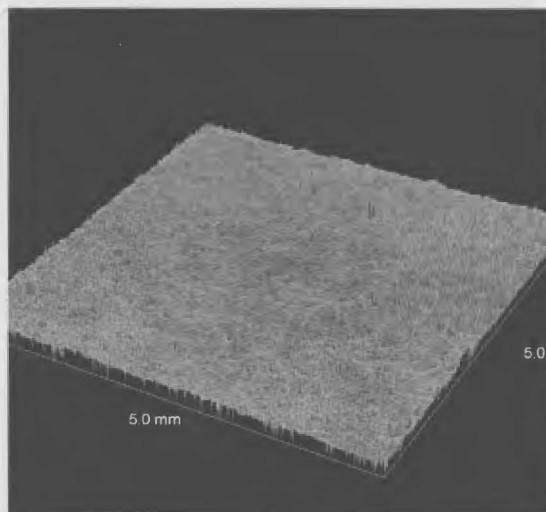


Figure 3.15 Handsheet surface profile obtained by Wyko NT1100 surface profiler, the scale in each direction is 5mm by 5mm, with a minimum resolution of 5 μ m.

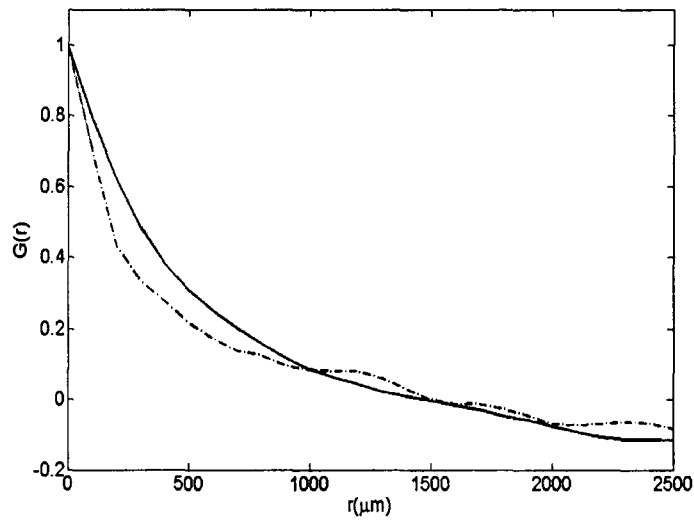


Figure 3.16 Plots of the two-point mass-mass correlation function (formation correlation), for simulated virtual (solid line) and experimental (dash-dot line) handsheet paper samples. Basis weight is 36g/m^2 .

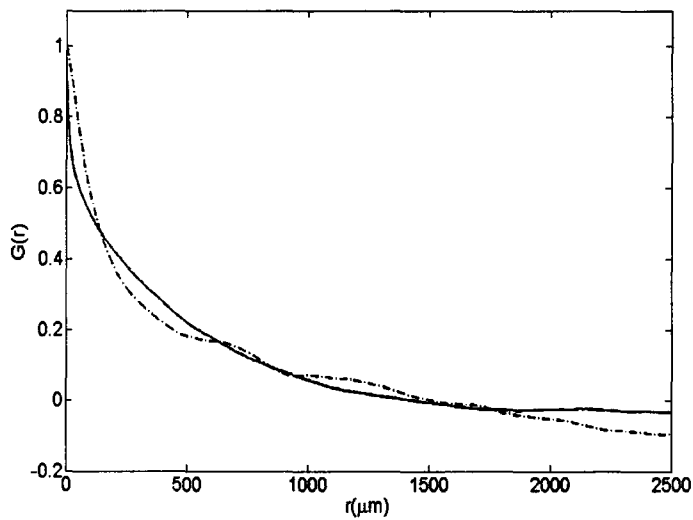


Figure 3.17 Plots of the two-point height-height correlation function (roughness correlation) for paper roughness from simulated (solid line) and experimental (dash-dot line) handsheet paper samples. (Basis weight is 36g/m^2).

As shown in Table 3.4 and the data in Figure 3.16 and Figure 3.17, it is relatively straightforward to select the parameters of our 3D fibre network model such as to reproduce the statistics of handsheets paper webs, as well as to simulate various key statistical properties of handsheets paper webs.

3.3 Improvement of “dry” Paper Compression Formalism

In the work reported below on toner transfer, it will be necessary to include paper deformation in the print nip. As such, it is necessary to model compression of dry handsheets paper, in order to capture paper-nip interactions as accurately as possible. The precise conditions of paper compression are presently very poorly understood - let alone exceedingly difficult to model in a practical manner. To our knowledge our paper structure model reported above is the first attempt to model the microscopic properties of stochastic 3D paper structure in a way that can account, to some degree, for paper deformation. The response to paper deformation during the “forming” process has thus far been made by using certain phenomenological, piece-wise, approximations of the assumed flow stress and strain behaviour or paper has been assumed. While this may be satisfactory in wet pressing of paper where the paper web essentially undergoes an extreme amount of irrecoverable plastic deformation, this is not the case in dry compression – as may happen in a print nip - where only a small amount of elastic and plastic deformation occurs.

In light of the above comments, one of the aims of this thesis is to improve the deformation phenomenology for dry-end pressing to be used in the paper structure model. This formalism will be based on knowledge gained by new experiments, which we carried out to elucidate the stress-strain characteristics of paper. These are described next.

3.3.1 Experimental Characterization from Micro-Indentation Testing

The behaviour of paper under compression is often linked to that of cellular, honeycomb materials. Figure 3.18 is a generic characterization of the stress-strain behaviour of a honeycomb material under compression; this material exhibits a five - stage compression behaviour. The first stage is linear and measures the elastic bending of the cellular walls, the second and third stages represent the buckling of cellular walls - there is a large change in strain with a small change in stress. The fourth stage is the strain hardening region where the majority of pore structure in the hardwood fibre or softwood fibre has collapsed – there is a small change in strain with an increasing stress. The fifth stage is densification where cell walls are touching and the situation begins to resemble the elastic compression of pure cellulose. It is our aim to obtain analogous information such as that of Figure 3.18 for paper handsheets.

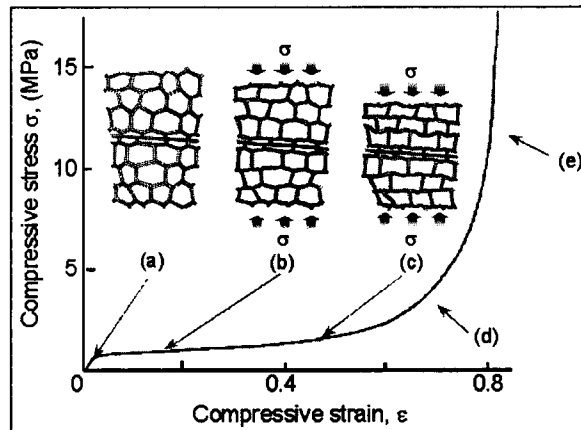


Figure 3.18 Generic compression behaviour of a cellular, honeycomb material (Rodal 1983, Gibson 1988).

Micro-indentation experiments were used to characterize the specific response of our paper samples as a function of mass density and indenter radius. The micro-indentation system, which includes a force transducer apparatus and a movement control system, was developed under the supervision of Dr. Kari Dalnoki-Verress in the Department of Physics at McMaster University, in collaboration with Andrea Collis from the Department of Chemical Engineering. It was modified for our needs by Adam Raegan, Ph.D.

The force transducer apparatus is fastened onto the movement control system, which can move in the x, y and z directions with steps as low as $0.1 \mu\text{m}$. The indenter, which can be changed for our needs (i.e. different indenter radius) is screwed onto the force transducer. When the system moves down in the z direction, the indenter will press the samples, which are put onto the sample holding platform. The magnitude of

force applied is then obtained by the force transducer. Thus, the micro-indentation system will record the value of force for every step that the indenter moves down. The whole system is interfaced with the Labview7.0 software and the output sent to an excel file, in which the force and the position of indenter in z direction are recorded for every deformation step.

A silicon chip is used to hold the paper samples. There are two reasons for this: the surface of the silicon chip is smooth; and the silicon is hard enough that it will not change its shape by the applied force (about 80 gram).

Experiments are carried out in two stages. Figure 3.19 shows a schematic of the process (not to scale). The first step involves measuring force-displacement on the silicon chip (without the paper sample on the chip). This is performed for two reasons: the first is to measure the elastic behaviour of the system plus the silicon chip under the applied force, to ensure that the system of any offset due to the silicon chip can be removed from the compression of the paper. Thus, when compressing paper, the contribution to the strain arising from the silicon chip can be subtracted, yielding deformation information of the paper alone.

In the second step of the deformation process, a piece of paper (chosen to be of area 5mm by 5mm to avoid paper crinkle), is placed onto the silicon chip shown as in Figure 3.19 (b). The indenter is moved in x, y direction to ensure that it is located at the center of the paper surface. It then descends downward in the z direction in steps

of 0.1 μm . The position and the magnitude of force will be recorded in an excel file, by which the displacement - force relationship can be obtained, after the offset displacement due to the silicon substrate is subtracted. The method to obtain and subtract the contribution from the silicon chip is as follows:

Without paper present, when the indenter just contacts the silicon surface, the position is $h_0(1)$. When the indenter moves down, the position changes to h_1 , and the force is F . So the displacement is calculated by

$$\Delta h(1) = h_1 - h_0(1) \quad (3.14)$$

According to Hooke's law, the $\Delta h(1)$ and F should have a linear relationship, denoted by

$$F = -k \cdot \Delta h(1) \quad (3.15)$$

The quantity $(h_1 - h_0)$ is proportional to F , and k can be calculated by equation (3.15). We found that this relationship does not change with different indenters.

When paper is present, as the indenter descends, it contacts the paper surface, and that position is denoted $h_0(2)$. Subsequent descent of the indenter causes the indenter to move to a lower position still, denoted by h_2 . The force F is obtained from the output file. The displacement is now calculated by

$$\Delta h(2) = h_2 - h_0(2) \quad (3.16)$$

Under the force F , and assuming the paper - silicon system is in equilibrium, the displacement due to the silicon chip can be obtained by

$$\Delta h(1) = -F / k \quad (3.17)$$

The resulted displacement from compression of paper sample is thus

$$\Delta h = \Delta h(2) - \Delta h(1) \quad (3.18)$$

Thus the stress and strain can be calculated by equations 3.19 and 3.20

$$\sigma = \frac{F * 1000 * g}{A_0} \quad (3.19)$$

$$\varepsilon = \frac{\Delta h}{t_0} \quad (3.20)$$

where F (in grams) is the force measured in the second step, g is gravity (9.81 m/s^2), and A_0 is the area of the indenter head and t_0 is the initial paper thickness. This procedure can be repeated with different indenter radius and different paper samples (i.e. different basis weights).

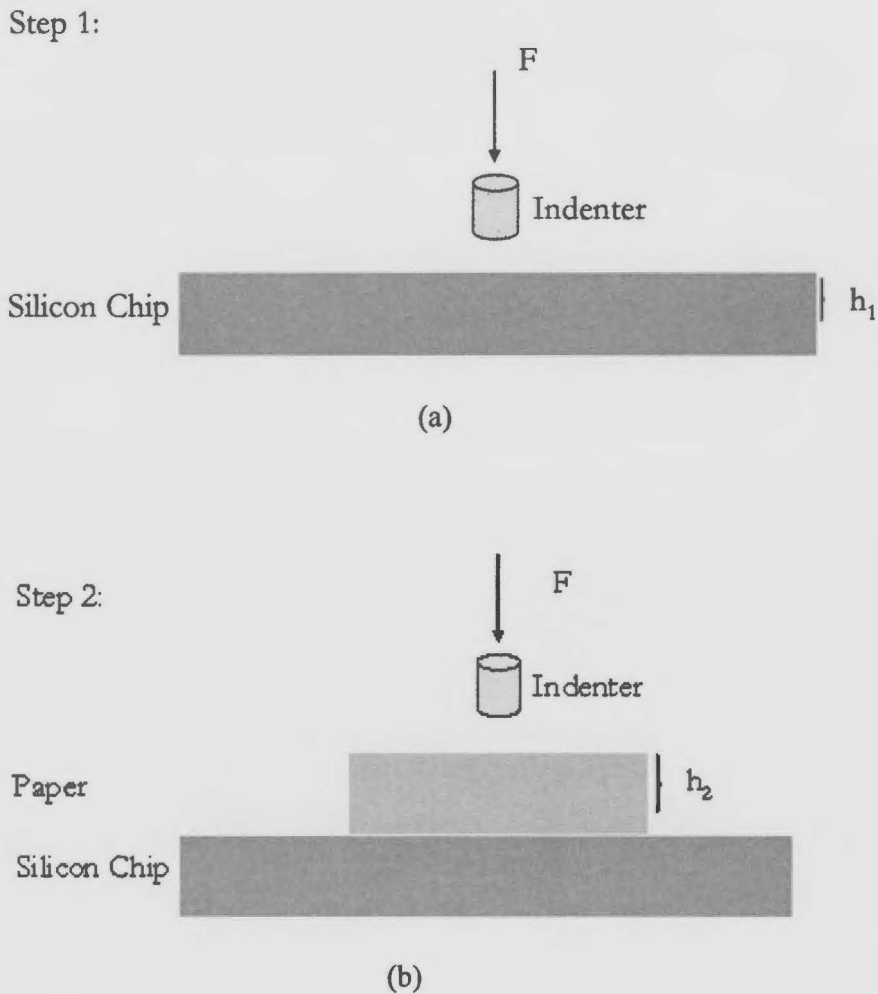


Figure 3.19 Two stage paper compression testing

3.3.2 Experimental Results and Discussion

Four indenter radii were used in our paper compression tests, 855 μm , 505 μm , 425 μm and 210 μm . These indenters were polished with sand paper to make sure that the tip on every indenter was flat. Thus, the indenter heads used in the micro-indentation tests did not rip into the paper. The paper samples used in the tests involved four grades, 30.48 g/m^2 (thickness 50 μm), 45.97 g/m^2 (thickness 102 μm),

62.48 g/m² (thickness 123µm) and 92.45 g/m² (thickness 195µm).

The following sets of micro-indentation experiments were conducted: (1) The 855 µm indenter was used to compress six paper sections from the 30.48 g/m², 45.97 g/m², 62.48 g/m² and 92.45 g/m² basis weight handsheets (the six sections comprised two regions on each of three 5mm by 5mm pieces cut out from a handsheet sample of each basis weight); (2) the 505 µm indenter was used to compress six paper sections from the 30.48 g/m², 45.97 g/m², 62.48 g/m² and 92.45 g/m² basis weight handsheets; (3) The 425 µm indenter was used to compress six paper sections from the 30.48 g/m², 45.97 g/m², 62.48 g/m² and 92.45 g/m² basis weight handsheets; (4) The 210 µm indenter on was used to compress six paper sections from the 30.48 g/m², 45.97 g/m², 62.48 g/m² and 92.45 g/m² basis weight handsheets.

3.3.2.1 Force-Displacement Characterization of Silicon Substrate

Figure 3.20 shows the calibration from the indentation of the silicon for the four indenter heads. These curves follow essentially the same linear relation, and it is proved that the system used for paper samples tests is reliable. By using the method discussed above, k was obtained and found to be 11432 N/mm.

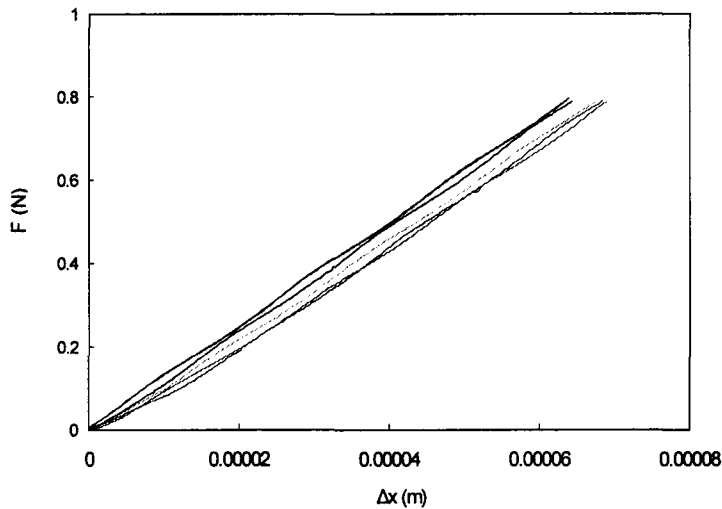


Figure 3.20 Force-displacement behaviors for different indenters.

3.3.2.2 Typical Stress-Strain Characterization of Paper

Figure 3.21 shows the result of stress vs. strain curves from one indenter radius (855 μm) pressing on the six different areas of one handsheet paper of density (30.48 g/m^2 , 50 μm average thickness). Six tests are shown, corresponding to the six different areas, as mentioned above. We note that for all measurements, the indenter heads were large enough to encompass from several tens to hundreds of fibre crossings, thus avoiding the ripping of the indenter head through the paper. Data obtained differed from that of generic honeycomb cellular materials were shown in Figure 3.18. Whereas generic honeycomb materials exhibited 5 compression stages, the handsheet compression data appears to exhibit only the final 2 stages of compression referred to in Figure 3.18. This can be explained by noting that in handsheet paper – as well as in most commercial papers -- fibres lumens (the hollow in the centre of a fibre) are

almost fully collapsed. As a result the stress - strain curve of a paper web comprising such fibres will exhibit mainly strain harden because of densification. The strain hardening stage is shown by the rapid increase of stress resulting from a small change in strain. This is the phenomenon of pore collapse. The following high-slope linear region is the densification stage where most pores have collapsed, and many cell walls have started to contact. It is likely that the scatter seen within one density, shown in Figure 3.21, is due to the variation of local mass density (which incorporates thickness variation) away from the average density. The heterogeneity of paper structure results in point-to-point variations in all measurable quantities. *To obtain representative data specific to a given basis weight and indenter head, data such as that shown in Figure 3.21 is averaged over the six curves (i.e. over the six paper regions in each sample). This process is hereafter referred to as “ensemble averaging”.*

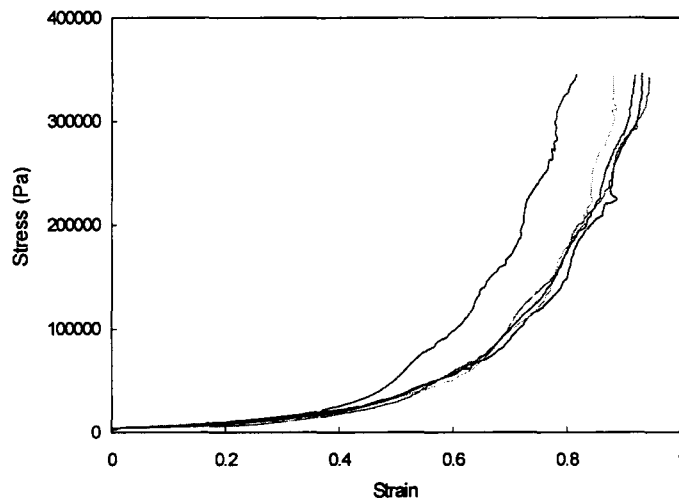
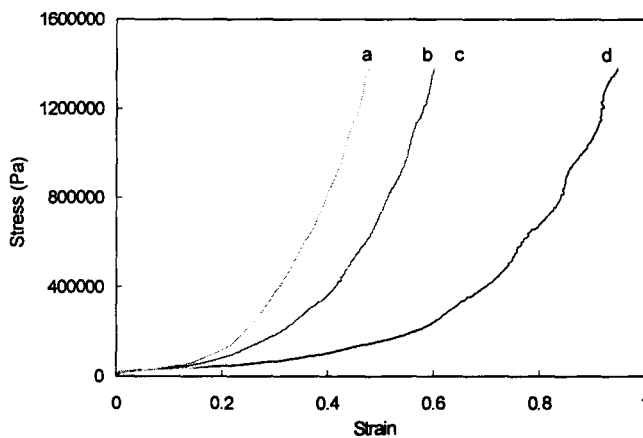


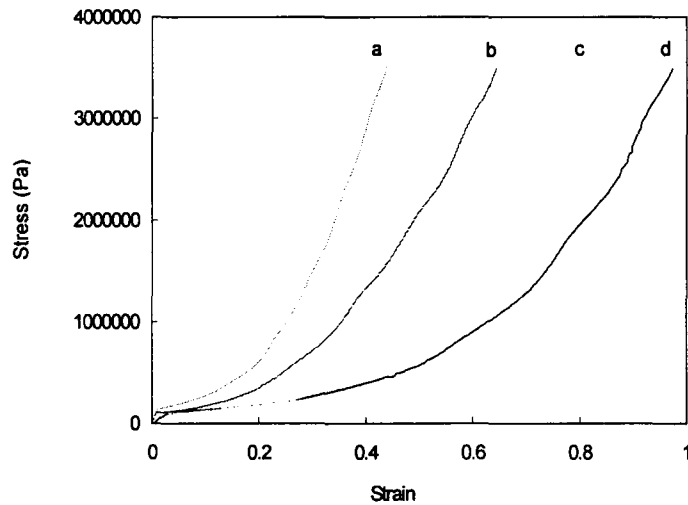
Figure 3.21 Stress-strain behavior from six samples (i.e. areas) of handset papers of basis weight 30.48 g/m^2 , under an $855 \text{ }\mu\text{m}$ radius indenter head.

3.3.2.3 Stress-Strain Characterization of Paper vs. Paper Basis Weight and Thickness

Figure 3.22 shows the ensemble-averaged stress vs. strain curves for the four paper densities (basis weights) examined (92.45 g/m^2 , 62.41 g/m^2 , 45.97 g/m^2 and 30.48 g/m^2). The data in part (i) of the figure was obtained with a $505 \text{ }\mu\text{m}$ radius indenter while that in part (ii) with a $425 \text{ }\mu\text{m}$ radius indenter head. In the figure, paper with lowest basis weight has the smallest stress for the same strain. With the increase of the paper basis weight, the stress increases for the same value of strain. Since the handsheets were allowed to air-dry after deposition, without any wet pressing, each basis weight shown in Figure 3.22 also corresponded to a separate average paper thickness. Thus, it is evident from the data in Figure 3.22 that different paper thicknesses (termed “caliper” in the paper industry) compress differently. Indeed, it is evident that the larger the thickness, the larger the effective area required to normalize the different stress-strain curves.



(i)

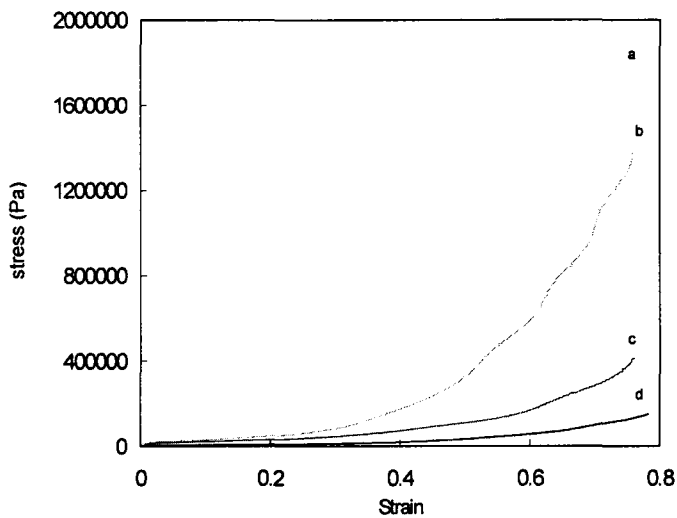


(ii)

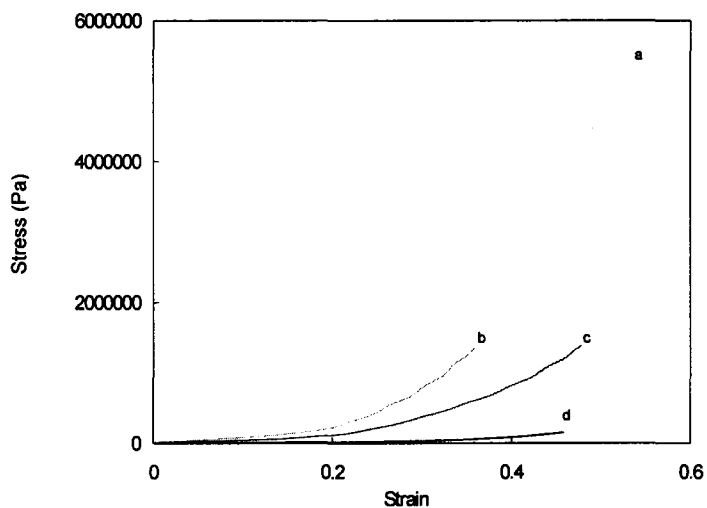
Figure 3.22 Stress-strain behaviours of varying paper densities under (i) a 505 μm radius and (ii) a 425 μm radius indenter head. The curve 'a' is representative of an average handsheet density of 92.45 g/m^2 , the curve 'b' 62.41 g/m^2 , curve 'c' 45.97 g/m^2 and curve 'd' 30.48 g/m^2 .

3.3.2.4 Stress-Strain Characterization of Paper vs. Indenter Head

Figure 3.23 shows the ensemble-averaged stress-strain curves for varying indenter head radius (210 μm , 425 μm , 505 μm , and 855 μm). The two figures show this data for the case of (i) 30.48 g/m^2 and (ii) 92.45 g/m^2 basis weight handsheet papers.



(i)



(ii)

Figure 3.23 Stress-strain behaviours for varying indenter head radius for samples with average density of (i) 30.48 g/m² and (ii) 92.45 g/m². The curve ‘a’ is the representative of an indenter head radius of 210 μm, curve ‘b’ 425 μm , curve ‘c’ 505 μm and curve ‘d’ 855 μm.

The resulting stress-strain behaviour will be typically dependent on different indenter head areas. On the same type of paper, the largest indenter head (largest radius) generates the largest strain for the same stress. This can be attributed to the number of fibre cross-links influencing the effective area over which the applied force is distributed. It is evident for each indenter head, the effective area required to normalize the different stress-strain curves should actually be greater than the indenter head itself.

3.3.2.5 Scaling of Experimental Results

It is instructive to incorporate the effects of indenter size and paper thickness into a unified description. The effect of indenter radius is particularly useful in the context of the compression module of the paper structure model discussed earlier in this chapter. It is to be recalled that the model decomposes the paper sheet into zones of dimensions $\xi \times \xi$, where ξ was defined as the lateral length scales beyond which the “mass springs” --composed of fibres in their interior-- decouple (i.e. stop interacting with one another). Understanding at what point indenter head size scales out of the stress strain curve of the paper, and relating this to the properties of the paper web can thus allow us to estimate the parameter ξ .

It was found that the experimental curves from the ensemble-averaged stress strain curves for the 16 sets of experiments, which were obtained by four different indenter heads (210 μm , 425 μm , 505 μm , and 855 μm) on four thickness samples

(195 μm , 123 μm , 102 μm and 50 μm), could be approximately collapsed onto one master stress strain curve. (In the following section, the thickness of the sample will be used, since the different stress-strain properties were correlated to different paper thickness, not paper basis weight.) This is seen by noting that the loading force in each experiment can be normalized according to

$$\sigma = F/[\pi(R_{\text{ind}} + h)^2] \quad (3.21)$$

where R_{ind} is the indenter radius. Equation 3.21 can be re-arranged as,

$$\sigma = F/[\pi R_{\text{ind}}^2(1 + h^*)^2] \quad (3.22)$$

where we have defined a h^* as

$$h^* = h/R_{\text{ind}} \quad (3.23)$$

where F is the applied force, R_{ind} is the radius of the indenter head, and h is an effective length scale over which the applied force acts (See figure 3.24). The length scale h , which is called the “*additional radius*”, has been estimated for each curve by requiring all 16 stress strain curves from the different indenter heads and paper thickness to collapse onto one “master” scaling function. The philosophy of this approach generally has three stages: (1) assumes the existence of such a master curve; (2) establish if scaling parameters can be found to achieve such a scaling; (3) connect the scaling parameters to a physical process or property.

The collapsed (scaled) curves can be seen in Figure 3.25 below. The factor h^* in Equations 3.23, which was used to scale each curve to the master curve, is plotted

against normalized $R_{\text{ind}}/R_{\text{ind}}^{\text{max}}$ in Figure 3.26, where $R_{\text{ind}}^{\text{max}}$ is the largest indenter radius we used. The different curves in Figure 3.26 separate into different paper thicknesses: 'x' 195 μm (92.45 g/m^2), '▲' 123 μm (62.41 g/m^2), '■' 102 μm (45.97 g/m^2) and '◆' 50 μm (30.48 g/m^2). For all paper thicknesses, increasing the indenter head radius will greatly decrease the factor h^* .

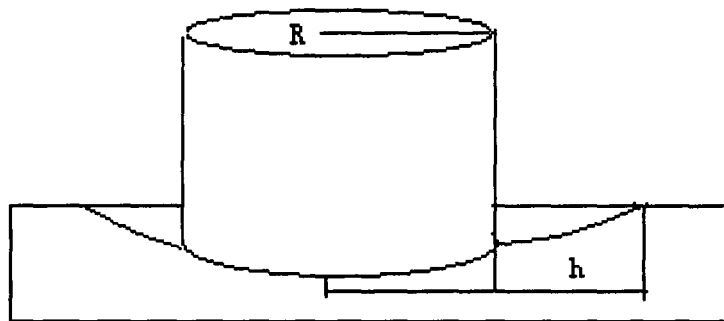


Figure 3.24 Schematic of additional length scale h .

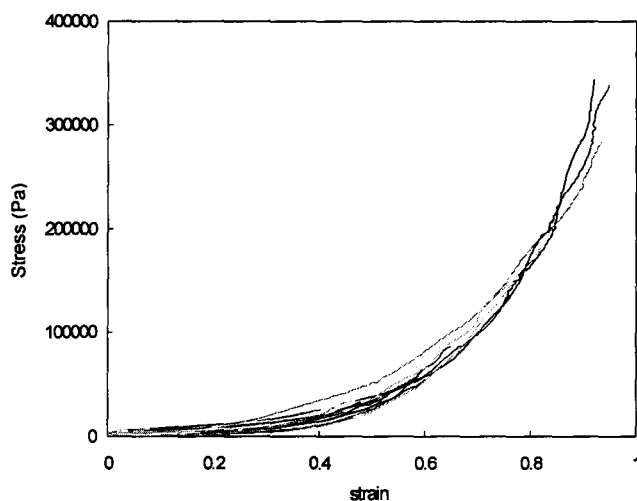


Figure 3.25 Normalized Stress-Strain results from 16 groups of experiments: Four different indenter heads (210 μm , 425 μm , 505 μm , and 855 μm) acting on four different paper thickness (195 μm , 123 μm , 102 μm , and 50 μm).

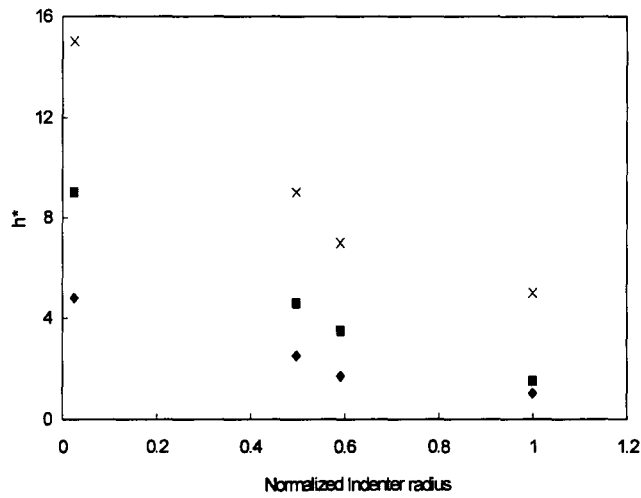


Figure 3.26 The lateral spreading of strain outside the indenter region over the indenter radius h^* (h/R_{ind}) is plotted against R_{ind}/R_{ind}^{max} . Different curves separate into different paper thicknesses: ‘x’ 195 μm (92.45 g/m^2), ‘▲’ 123 μm (62.41 g/m^2), ‘■’ 102 μm (45.97 g/m^2) and ‘◆’ 50 μm (30.48 g/m^2).

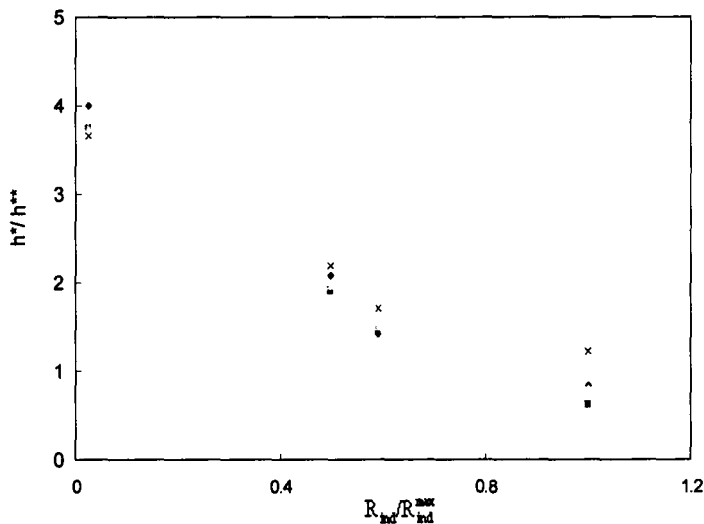


Figure 3.27 Scaling results of h^*/h^{**} against R_{ind}/R_{ind}^{max} : ‘x’ 195 μm (92.45 g/m^2), ‘▲’ 123 μm (62.41 g/m^2), ‘■’ 102 μm (45.97 g/m^2) and ‘◆’ 50 μm (30.48 g/m^2).

To further correlate the stress strain behaviour of our handsheets with their thickness (δ), an index $h^{**}(\delta)$ is defined, chosen in such a way that all the h^*/h^{**} vs. R_{ind}/R_{ind}^{max} curves in Figure 3.26 collapse onto one another. These scaled results are plotted in figure 3.27. Figure 3.28 shows a linear relationship between h^{**} and δ . This relation does yield as good a collapse as is the case that different paper thickness with indenter radius (i.e. Figures 3.25 and 3.26). However, this scaling can still be treated as “semi-empirical”, at least at a practical level. Further work is required to more precisely elucidate the nature of $h^{**}(\delta)$.

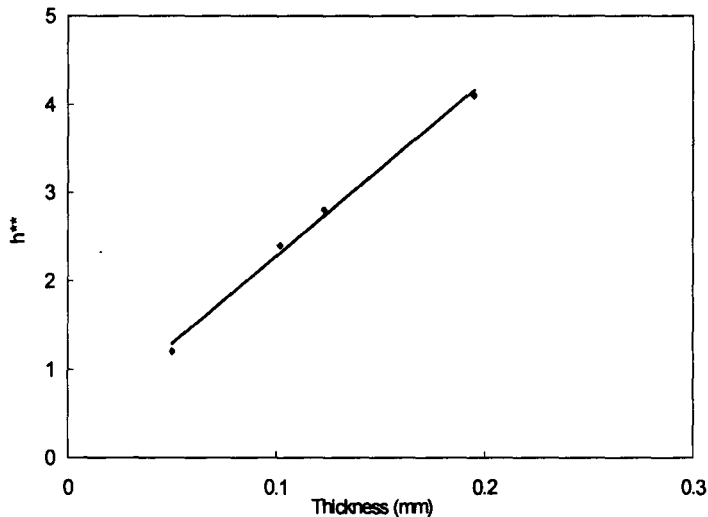


Figure 3.28 Scaling results of h^{**} against sample thickness.

Thus, if the stress-strain property of a certain thickness of handsheet paper is known, from the scaling methods above, that of other thickness of handsheet paper can be obtained, at least approximately. Considering Figure 3.28, the index h^{**} can be

fit to thickness in the approximate form

$$h^{**} = 19.84\delta + 0.29 \quad (3.24)$$

Meanwhile the relation between h^*/h^{**} and normalized indenter radius R_{ind}/R_{ind}^{max} is approximately fit to the scaling results in Figure 3.27 (using the 50 μm curve) according to

$$h^*/h^{**} = 4.19\exp(-1.63(R_{ind}/R_{ind}^{max})/0.855) \quad (3.25)$$

From equation (3.25) we can thus approximate h^* for handsheets with different thicknesses as

$$h^* = 4.19(19.84\delta + 0.29)\exp(-1.63(R_{ind}/R_{ind}^{max})/0.855) \quad (\text{unit:mm}) \quad (3.26)$$

Finally, the “*additional radius*” h for known paper basis weight (or thickness) being compressed under known indenter head of radius R can be approximated as

$$h = 4.19R_{ind} \cdot (19.84\delta + 0.29)\exp(-1.63(R_{ind}/R_{ind}^{max})/0.855) \quad (3.27)$$

To summarize, the results above show that the differences of stress-strain behaviour for different paper samples (basis weight) under different indentation radius can be explained by the additional effective radius h (3.21), which arises from the fibre cross-links in the paper increasing the effective area over which the applied force is distributed. From our experiments this additional effective radius h is correlated to the paper thickness and indenter head radius and for handsheets approximately

follows the relationship in equation (3.27).

The effective area of each such zone (referred to as ξ in the paper structure model description above) can be found from Equation 3.27 as follows: By requiring h/R_{ind} in Equation (3.27) to be smaller than some cutoff (e.g. a conservative estimate is approximately $h/R_{ind} \sim 0.1$), we can extract an effective indenter head, R_{ind}^* . The spring decoupling length ξ then becomes $\xi \approx R_{ind}^*$. For most realistic paper thicknesses ($\sim 70\mu m$), Figure 3.26, (or Equation 3.27) gives $\xi \sim 800\mu m$ as the effective length scale beyond which the deformation behavior of our simulated paper webs is expected to be realistic. This is still smaller than most printing defects, which occur on mm-cm scale.

3.3.3 Incorporating Paper-Nip Compression into Paper Structure Model

A stress-strain curve corresponding to the collapsed stress strain data in Figure 3.25 was fit to a polynomial form

$$\sigma_s = \sum_{n=1}^4 c_n \varepsilon_s^n \quad (3.28)$$

where σ_s and ε_s are the scales stress, Equation 3.22 and the strain, respectively, and where $c_1=38972$, $c_2=-169461$, $c_3=422003$ and $c_4=103117$ (the units are Pa, N/m²). The polynomial in Eq. (3.28) is shown in Figure 3.29.

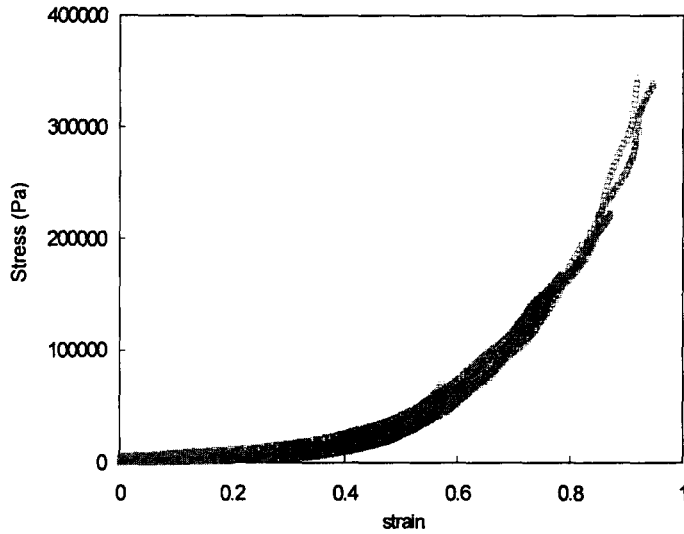


Figure 3.29 Stress vs. strain response of the trend-line of Eq. (3.28) (dashed-dotted line) compared to the scaled stress curves in Figure 3.25, averaged and shown in cyan.

From equation (3.22), (3.27) and equation (3.28), *the engineering stress-strain behavior for known paper basis weight (thickness) being compressed under known indenter head of radius R_{ind} can be approximated as*

$$\begin{cases} \sigma = \sum_{n=1}^4 c_n \varepsilon_s^n \cdot \left(\frac{R_{ind}}{R_{ind}^{max}}\right)^2 \cdot \left(1 + \frac{h}{R_{ind}}\right)^{-2} \\ h = 4.19 R_{ind} \cdot (19.84\delta + 0.29) \exp(-1.63(R_{ind}/R_{ind}^{max})/0.855) \end{cases} \quad (3.29)$$

We note that in the limit of $h/R_{ind} \ll 1$, Equation (3.28) can be input directly into the paper structure model to describe the stress strain properties of individual zones of the paper webs.

Chapter 4

Analysis of Electrostatic Toner Transfer Forces

Having established a modeling platform for generating virtual paper microstructure and its effective compressibility properties in a printing nip, we now shift our attention to the role that paper structure plays in controlling the electrostatic forces responsible for transferring (or biasing) toner onto paper from the photoreceptor.

We start by formulating a model to describe electrostatic transfer forces in a printing nip. The model is first used to conduct a mathematical analysis elucidating the response of electrostatic forces to variations in mass density, surface profile, filler and porosity distributions. Following this analysis, the combined effect of variations of all these measures –the case in real paper-- will be examined.

4.1 Toner Transfer Physics Revisited

Motivated by the original toner transfer system envisioned by Yang and Hartman described in chapter 2, we set up the toner transfer system as illustrated in figure 4.1. There are three layers in the transfer system, photoconductor layer, toner particle layer and paper layer. (According to different transfer schemes, we also can consider four layers, by adding a layer of air between the toner particle layer and paper layer.) The photoconductor layer is assumed to have a perfectly uniform structure; the toner layer

has a mass distribution that can be set as uniform or distributed by some known function. The paper substrate has a heterogeneous structure, which can be generated analytically or through input from the paper structure model discussed in chapter 3.

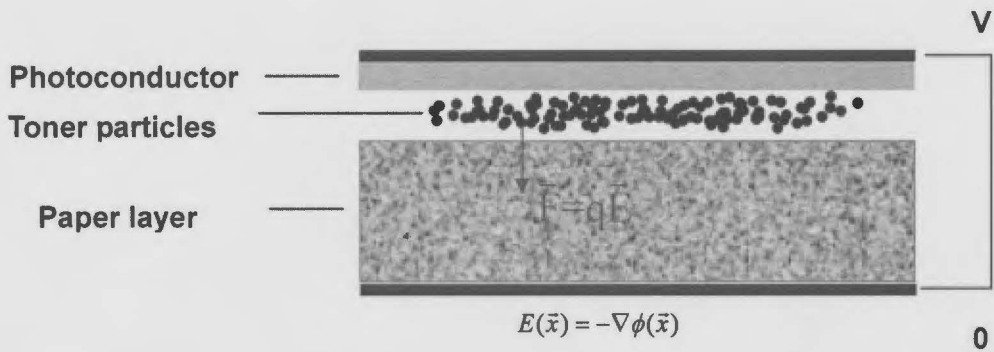


Figure 4.1 Toner transfer model.

This spatially extended model (shown in figure 4.1) of toner transfer thus can proceed by considering Gauss's law (Page 1928),

$$\nabla \cdot D(\vec{x}) = \rho(\vec{x}) \quad (4.1)$$

where D is the electric displacement, ρ is the charge distribution between the transfer sandwiched layer. The displacement field D is related to the electric field E by

$$D(\vec{x}) = \varepsilon(\vec{x})E(\vec{x}) \quad (4.2)$$

where $\varepsilon(\vec{x})$ is the spatially distributed dielectric of the paper and toner layers. The relation between the intensity of electric field and potential $\phi(\vec{x})$ is given by

$$E(\vec{x}) = -\nabla\phi(\vec{x}) \quad (4.3)$$

Combining the equations above leads to the well-known Poisson equation describing the electrostatics of toner transfer process, which will be of the form

$$\vec{\nabla} \cdot (\varepsilon(\vec{x}) \vec{\nabla} \phi(\vec{x})) = -\rho(\vec{x}) \quad (4.4)$$

For any toner charge distribution $\rho(\vec{x})$, the complete simulation of the toner transfer forces in any dielectric configuration can thus be computed using equation (4.4). After solving equation (4.4), the electrostatic potential distribution $\phi(\vec{x})$ in the sandwiched print-nip region can be obtained, from which the electrostatic transfer field distribution active within the toner layer and toner transfer force can be computed according to

$$E(\vec{x}) = -\nabla\phi(\vec{x} : \text{toner layer}) \quad (4.5)$$

$$F(\vec{x}) = q(\vec{x}) \cdot E(\vec{x}) \quad (4.6)$$

Where $q(\vec{x})$ is the toner charge distribution, $F(\vec{x})$ is the transfer force distribution in the toner layer.

4.2 Multigrid Solver for the Poisson Equation with Random Dielectric Field

There are several standard iterative techniques to solve the toner transfer model defined by Equation (4.4). These include Jacobi, Gauss-Seidel and SOR (Successive

Over Relaxation) (Metcalf 1992). These iterative procedures remove high frequency components of the error in a few iteration steps. However, the removal of the low frequency components of the error becomes much more difficult, resulting in the slow convergence of relaxation methods on a fixed grid, so these kinds of iterative procedures are computationally very expensive and impractical.

The so-called Multigrid (Trottenberg 2001) method is the most efficient iterative procedure to solve Poisson equation-like steady state boundary-valued problems. Multigrid method works on a sequence of grids from coarsest grid to finest grid $m = 1, \dots, M$, where the grid size ratio $\Delta_{m+1}/\Delta_m = 1/2$. The low frequency component on a fine grid becomes a high frequency component on a coarse grid and so it can be effectively smoothed. Consequently, in multi-grid methods, the smoothed error on a fine grid is transferred to the coarser grid using a restriction operation; such restriction procedure is repeated until the coarsest grid is reached where exact solution can be obtained. Next, the solution of the error on the coarse grid is transferred to next finer grid by an interpolation operation and adds up to the initial solution on this finer grid; such interpolation procedure is repeated until the finest grid is reached where the numerical solution is sought. Therefore, the total number of numerical operations in multigrid is approximately

$$\alpha N^3 \sum (1 + 1/8 + 1/8^2 + \dots + 1/8^N) \approx (8\alpha/7) \propto o(N^3) \quad (4.7)$$

where N is the number of grids in each direction (assume equal number of grids in

each direction, i.e. x, y, z.), α is a number smaller than 10, which takes into account the number of iterations (usually several) on each grid level plus restriction and interpolation operations.

Thus, the total number of numerical operations in Multigrid is linearly proportional to total number of grid points. On the contrary, other iterative methods require at least on the order of the total number of grid points raised to the power of 3/2. (See table 4.1) Therefore, the multigrid method is far superior to any other iterative methods. For example, for a computational domain containing around 2 million grids (128^3), multigrid method is at least a thousand times faster than other iterative methods.

Table 4.1 Number of iterations for different kinds of iterative methods (Metcalt 1992, Trottenberg 2001, 3-dimension, N grid points in every dimension are assumed)

Iteration Methods(3D)	Number of iterations
Gaussian elimination	N^6
Jacobi	N^6
Gauss-Seidel	N^6
Fourier Transform	$(N \log N)^3$
Multigrid	N^3

To solve equation (4.4), a finite volume approach was first used to discretize the equation on a cell-centered Cartesian grid. The region under consideration was divided into $N_x \times N_y \times N_z$ (power of 2) finite volumes with dimension h_x , h_y , h_z in

each direction. In x and y directions, zero-flux boundary condition was applied. In the z direction, Dirichlet boundary conditions were adopted; more specifically, the bottom surface was held at $\phi = 0$, and the top surface is held at $\phi = V_g$, where V_g is a given electric potential. The values of known functions $\varepsilon(\vec{x})$, $\rho(\vec{x})$ (the first comes from the paper model and the second from the properties of charged toners) and unknown function $\phi(\vec{x})$ (here denoting the electrostatic potential) are placed on the cell centers. Applying Gauss divergence theorem on equation (4.4), we obtained

$$\iiint \nabla \cdot (\varepsilon(\vec{x}) \nabla \phi) dV = \iint \varepsilon(\vec{x}) \nabla \phi \cdot d\vec{S} = - \iiint \rho(\vec{x}) dV \quad (4.8)$$

For an arbitrary finite volume cell with label P , surrounded by neighboring cells labeled as E, W, N, S, T and B , referring to cells to the east, west, north, south, top and bottom, Equation (4.8) can be discretized as

$$F_e - F_w + F_n - F_s + F_t - F_b = -\rho_P \times h_x \times h_y \times h_z \quad (4.9)$$

Where F_e, F_w, F_n , etc. denote the flux across surfaces of cell P normal to the east, west, north, etc. For example, the flux across the surface with outer normal in the east direction is

$$F_e = \varepsilon_e \left. \frac{d\phi}{dx} \right|_e \times h_y \times h_z = \frac{2\varepsilon_P \times \varepsilon_E}{\varepsilon_P + \varepsilon_E} \frac{\phi_E - \phi_P}{h_x} \times h_y \times h_z \quad (4.10)$$

Where harmonic average of the dielectric constants of cells P and E is used for the dielectric on the surface normal to the east.

Equation (4.10) was expressed in stencil form involving cell P and its six neighboring cells. The implementation of no-flux boundary condition in x and y directions is trivial. However, in the implementation of Dirichlet boundary condition along z direction, to be consistent with the discretization shown in equation (4.9), discretization of second-order accuracy is preferred for higher numerical accuracy. For the purpose of exposition, let's assume cell P is bounded with the bottom surface with Dirichlet boundary condition, e.g., $\phi = V$, where V is a given constant. The cell to the top of cell P was labeled as T . Then

$$\phi_P = V + \left. \frac{\partial \phi}{\partial z} \right|_{z=0} \frac{h_z}{2} + \frac{1}{2!} \left. \frac{\partial^2 \phi}{\partial z^2} \right|_{z=0} \left(\frac{h_z}{2} \right)^2 + O(h_z^3) \quad (4.11)$$

$$\phi_T = V + \left. \frac{\partial \phi}{\partial z} \right|_{z=0} \frac{3h_z}{2} + \frac{1}{2!} \left. \frac{\partial^2 \phi}{\partial z^2} \right|_{z=0} \left(\frac{3h_z}{2} \right)^2 + O(h_z^3) \quad (4.12)$$

Multiplying equation (4.11) by 9, then subtracting the resulting equation with equation

(4.12), results in

$$\left. \frac{\partial \phi}{\partial z} \right|_{z=0} = \frac{9\phi_P - \phi_T - 8V}{3h_z} + O(h_z^2) \quad (4.13)$$

Then the flux through the bottom surface is obtained as

$$F_b = \left. \frac{\partial \phi}{\partial z} \right|_{z=0} \times h_x \times h_y = \frac{9\phi_P - \phi_T - 8V}{3h_z} \times h_x \times h_y \quad (4.14)$$

In Multigrid, the restriction operation is done by a simple summation over volumes, i.e. a coarse-grid volume is just a sum of the eight fine-grid volumes. The interpolation operation is done by trilinear interpolation.

For computational domain with unequal number of cells in each direction, e.g., $N_x > N_y > N_z$, first, semi-coarsening in x direction was performed (two finer cells in x direction were combined into a coarser cell) till the number of cells in x direction reaches that in y direction; then semi-coarsening in xy plane was performed (four finer cells are combined into a coarser cell) till the numbers of cells in x and y directions reached that in z direction; finally full coarsening was implemented till reaching coarsest grid. Conversely, for interpolation from coarser to finer cells, bilinear and linear interpolations were chosen for the reverse of above two semi-coarsening steps.

Iterative smoothing was implemented using the Full Multi-grid (*FMG*)

implementation, which began each iteration from the coarsest grid where an exact solution can be obtained, see figure 4.2. Red-and-black point-wise relaxation was used in the xy plane, while alternating plane relaxation in the z direction was used in FMG, for cases where the aspect ratio $((N_x/h_x)/(N_z/h_z))$ of the simulation box was not large. For large aspect ratios, line relaxation in z -direction was performed instead.

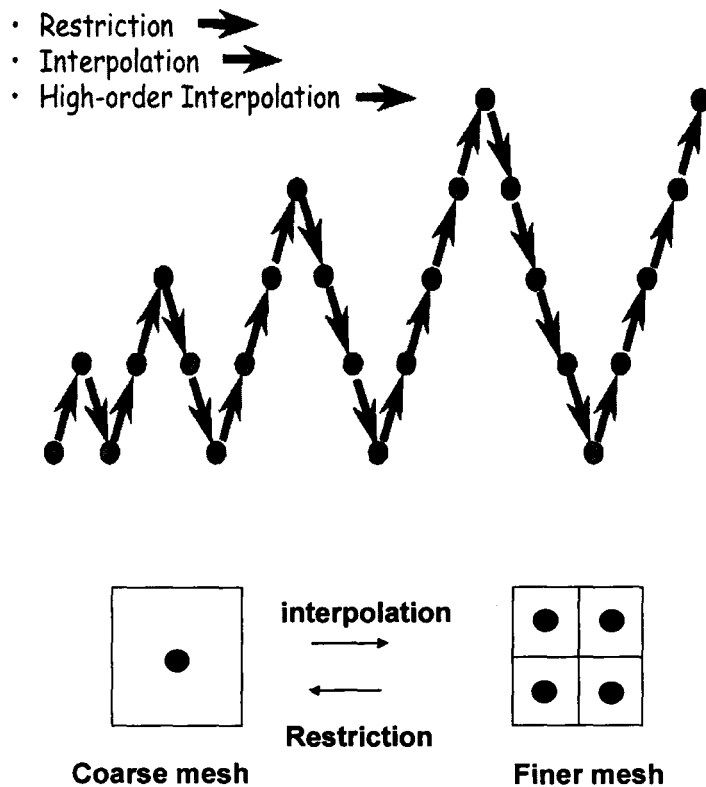


Figure 4.2 Schematics of FMG (Trottenberg 2001).

A parallelized MPI version of FMG was implemented to speed up computation.

The computational domain was evenly decomposed along z direction without change to the sizes in x and y directions, such that the system size in each process was $N_x \times N_y \times (N_z / np + 2)$, where np (power of 2) denotes number of processors in the computation, 2 was added to account for two extra ghost layers (top and bottom) for exchange data between neighboring processors. Except for exchanging data between neighboring processors, each processor worked independently, coarsening down to a single cell.

On the coarsest grid level, the np unknowns together with their stencils in the whole processors were distributed to each processor, such that in each processor the computation of the np unknowns corresponds to one dimensional three-point finite difference scheme in z direction, and the exact solution of the np unknowns were easily obtained by Gauss elimination.

Our Multigrid code was bench-marked by comparing with the known analytical result in a simple case. It was an effective one-dimensional model, with bottom-half of the computational domain filled with uniform dielectric of ε_2 , and top-half with uniform dielectric of ε_1 . There is no space charge in our test example, and the analytic result for the electric potential can be trivially obtained as follows

$$\phi_2 = \frac{2\varepsilon_1}{\varepsilon_1 + \varepsilon_2} V_g \cdot z \quad z \in \left(0, \frac{1}{2} N_z h_z \right) \quad (4.15)$$

$$\phi_1 = \frac{2\varepsilon_2}{\varepsilon_1 + \varepsilon_2} V_g \cdot z + \frac{\varepsilon_1 - \varepsilon_2}{\varepsilon_1 + \varepsilon_2} V_g \quad z \in \left(\frac{1}{2} N_z h_z, N_z h_z \right) \quad (4.16)$$

The numerical result from the Multigrid code converged within 0.1% relative error of the analytical result.

As an example of demonstrating the efficiency of our code, a completed simulation on a 1024 x 1024 x 64 system (with minimum cell size resolution corresponding to a 5 x 5 x 2 μm cell on 8 Dual Optron CPUs) was in approximately 7 minutes. This computational domain corresponds to a 5 x 5 mm section of paper of thickness $\sim 0.1\text{mm}$.

4.3 One-Dimensional Electrostatic Transfer

To compliment the full 3D electrostatic transfer model discussed above, the simpler 1D model of Yang-Hartmann, which solves the Poisson equation only in one dimension (i.e. the thickness (z) direction), was also extended to incorporate multiple dielectric layers, whose total thicknesses can be locally (i.e. at each point in the plane of the paper) either, (a) pre-specified analytically or (b) calculated directly from the simulated paper webs generated by the 3D fibre network model.

A schematic of the one-dimensional model for the case of four layers is shown in Figure 4.3. The thickness and dielectric constant of each of the four layers, comprising

paper, air, toner and photoconductor, is denoted d_i ($i=1,\dots,4$) and ε_i ($i=1,\dots,4$), respectively. In what follows, it will be implicitly assumed throughout that $d_i = d_i(x, y)$ and $\varepsilon_i \equiv \varepsilon_i(x, y)$ but the x, y dependence (in-plane position) will not be written for convenience. The charge density in toner layer is ρ ($\rho > 0$), and the charge density in other layers is for simplicity assumed to be zero.

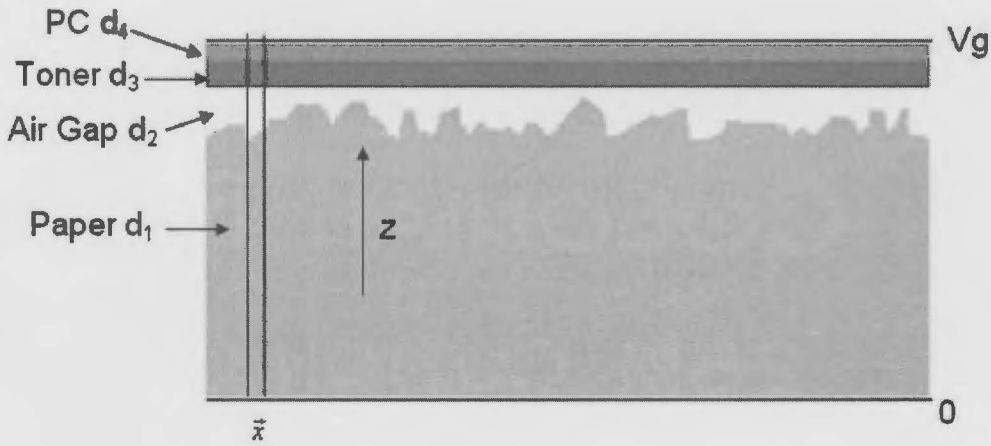


Figure 4.3 Illustration of system geometry and notation for the 1D model. The two dark lines show a 1D slice in which the model of Yang and Hartman are applied.

The 1D Poisson Equation was solved at position $\bar{x} \equiv (x, y)$ along the z -direction using local information about the thicknesses of various layers. In this case, there are four layers, corresponding to paper, air, toner and photoconductor. Local information can be input from the 3D fiber network model or generated analytically.

In this work, the total thickness of the system is $128 \mu\text{m}$ with $d_1 + d_2 = 110 \mu\text{m}$, $d_3 = 10 \mu\text{m}$ and $d_4 = 8 \mu\text{m}$. The relative dielectric coefficients of air, fiber, filler, toner

and photoconductor are 1, 4, 10, 3 and 3, respectively. The toner charge density is 32.43 C/m^3 . The applied voltage across the system equals 1500 Volts.

Poisson's equation for electric potential ϕ in each layer of a 1D slice shown in Figure (4.3) can be written as:

$$\frac{d^2\phi_i(z)}{dz^2} = -\rho_i / \varepsilon_i \quad (4.17)$$

The above equation is subjected to the following external boundary conditions:

$$\phi(z=0) = 0 \quad ; \quad \phi(z=d_1+d_2+d_3+d_4) = V > 0 \quad (4.18)$$

At each interface between different layers, continuity of electric potential and electric flux is obeyed. Simple algebra leads to the following expression for electric potential in the toner layer:

$$\phi_3(z) = -\left(\frac{\rho}{2\varepsilon_3}\right)z^2 + \left[\frac{\left(V + \frac{\rho d_3 d_4}{\varepsilon_4} + \frac{\rho d_3^2}{2\varepsilon_3}\right)}{\varepsilon_3 \alpha} + \frac{\rho(d_1+d_2)}{\varepsilon_3} \right] z + \left(\frac{d_1}{\varepsilon_1} + \frac{d_2}{\varepsilon_2} - \frac{d_1+d_2}{\varepsilon_3} \right) \cdot \frac{\left(V + \frac{\rho d_3 d_4}{\varepsilon_4} + \frac{\rho d_3^2}{2\varepsilon_3}\right)}{\alpha} - \frac{\rho(d_1+d_2)^2}{2\varepsilon_3} \quad (4.19)$$

Where

$$\alpha = \frac{d_1}{\varepsilon_1} + \frac{d_2}{\varepsilon_2} + \frac{d_3}{\varepsilon_3} + \frac{d_4}{\varepsilon_4} \quad (4.20)$$

Using $\phi_3(z)$, the electric field in toner layer is written as

$$\vec{E}_3(z) = -\vec{\nabla}_z \phi_3(z) = \left(\frac{\rho}{\epsilon_3} \right) (z - d_1 - d_2) - \frac{\left(V + \frac{\rho d_3 d_4}{\epsilon_4} + \frac{\rho d_3^2}{2\epsilon_3} \right)}{\epsilon_3 \alpha} \quad (4.21)$$

Equation (4.21) is quite useful in estimating the effect of air gap thickness and surface roughness on toner particles. Because the dielectric constant of air is smaller than that of paper, it can be seen from Equation (4.20) that when the thickness of the air gap d_2 is decreased while $d_1 + d_2$ is fixed, the strength of electric field acting on a toner particle will increase.

Therefore, it is expected that the surface roughness of paper will affect the electric force acting on toner particles, as will variations in the thickness of paper. This conclusion is in agreement with the results obtained by Cassidy, et al. (Cassidy 2004) for commercial copy paper.

The above analysis can also be applied to the study of effect of paper coating on toner transfer. For example, the air gap layer can be replaced by a coating layer which has higher dielectric constant than paper. It can be easily deduced that a thicker coating, i.e. larger d_2 , when $d_1 + d_2$ is fixed, will lead to higher electric field strength acting on toner particles.

It is straightforward to extend Equation (4.21) to a multi-layer configuration

with a total of N layers, with photoconductor and toner corresponding to the N th and $(N-1)$ th layers, respectively. The analogue of Equation (4.21) in such a multi-layer configuration is:

$$\vec{E}_{N-1}(z) = -\vec{\nabla}_z \phi_{N-1}(z) = \left(\frac{\rho}{\epsilon_{N-1}} \right) \left(z - \sum_{i=1}^{N-2} d_i \right) - \frac{\left(V + \frac{\rho d_{N-1} d_N}{\epsilon_N} + \frac{\rho d_{N-1}^2}{2\epsilon_{N-1}} \right)}{\epsilon_{N-1} \alpha'} \quad (4.22)$$

Where $\alpha' = \sum_{i=1}^N d_i / \epsilon_i$. Since the main dielectric materials in commercial paper are air, fiber and filler, we can re-express α' as

$$\alpha' = \frac{\sum_{i_{air}} d_{i_{air}}}{\epsilon_{air}} + \frac{\sum_{i_{filler}} d_{i_{filler}}}{\epsilon_{filler}} + \frac{\sum_{i_{fiber}} d_{i_{fiber}}}{\epsilon_{fiber}} + \frac{d_{toner}}{\epsilon_{toner}} + \frac{d_{photo}}{\epsilon_{photo}} \quad (4.23)$$

Where the sums of $d_{i_{air}}$, $d_{i_{fiber}}$ and $d_{i_{filler}}$ represent the total thickness of air (pore volume), filler and fiber at a given in-plane location in the paper web. It will be shown below that Equations (4.22) and (4.23) can only be used to accurately calculate the z -component of the electrostatic transfer force on long wavelength scale. For short wavelengths, the full 3D solution of the Poisson equation must be used.

4.4 Spectral Analysis of Electrostatic Field Variations

Principal Mode Analysis

The surface of paper can be seen –like any random signal in space or time - as a

simple superposition of a discrete number of sinusoidal frequencies of known amplitudes. As a result, understanding how individual frequencies of a surface undulation affect the electric field can be valuable to elucidate the role of a more complex surface on the electric field used to transfer toner in Xerography. The 3D electrostatic model(s) presented above will be used in this section to study the response of the electrostatic transfer field from a set of frequencies of the paper surface, filler or mass distributions.

4.4.1 Effect of Surface Fluctuations

We began first with a monolithic substrate placed in the [virtual] print nip, with a distorted surface comprising 4 sinusoidal frequencies. Specifically, the form of the surface variations imposed on the surface were $H = \bar{H} + \sum_k A_k \sin(2\pi x/\lambda_k)$, where the wavelength is λ_k , and A_k is constant for each wavelength. The resulting electrical field in the middle of a uniform toner layer was computed, and its Fourier transform calculated. The power spectrum, which is the squared magnitude of the Fourier transform, is plotted in Figure 4.4. The solution is obtained using our full 3D Poisson solver.

It can be seen from Figure 4.4 that besides responses at the Fourier modes corresponding to input sinusoidal waves of the surface, the electric field also contains responses at other Fourier modes, with various amplitudes. It is noted that while the amplitudes of the shorter wavelength surface perturbations (i.e. $k = 40, 60$) are the

same as longer wavelength surface perturbations (i.e. $k = 2, 5, 20$), the contribution of the shorter wavelength perturbations to the electric field is much smaller than that of longer wavelength perturbations.

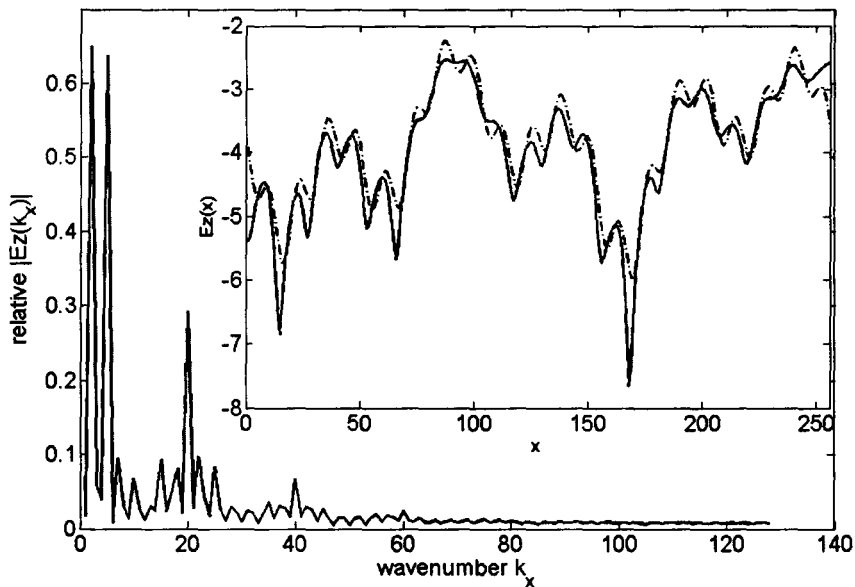


Figure 4.4 Power spectrum of the z-component of electric field obtained from the full solution of the Poisson Equation for a paper surface of the form $H = \bar{H} + \sum_k A_k \sin(2\pi x/\lambda_k)$, where the wave number is in unit of $2\pi/L$, with $L = 256 * 5 \mu\text{m}$. Other constants include $\lambda_k = L/k$, where $k = 2, 5, 20, 40, 60$, $\bar{H} = 80 \mu\text{m}$, $A_k = 6 \mu\text{m}$. The inset compares the real-space z-component of electric field obtained from Full Poisson equation solution to the solution of the 1D multi-layer model using principal modes of $k = 2, 5, 20$ to reconstruct the local paper thickness. In the inset, x is in unit of $5 \mu\text{m}$ and the electric field is in unit of 10^6 volts/meter.

The above observations can be conceptually understood if the Poisson equation is solved with a constant dielectric coefficient in Fourier space. As the wave number k goes to infinity, the corresponding electric field (in Fourier space) goes to zero. In other words, the contribution to electric field from very short wavelength perturbation is negligible compared to that from very long wavelength surface perturbation.

The results of Figure (4.4) are consistent with the recent work of Kallunki et al. (Kallunki 2005). In that work, they compared the solutions from a full Poisson equation solver using a *single* sinusoidal surface perturbation to a one-dimensional, three-layer model very similar to that introduced above in Section 4.3. They found that the electric field from surface perturbations of wavelength $\lambda \geq 3d_{per}$ --where in this case d_{per} is the mean distance from the position of the surface height to the centre of the toner layer-- can be modeled locally by an effective one dimensional capacitor model. Contributions to the electric field from perturbations with wavelength $\lambda \leq 3d_{per}$ need to be solved with the full 3D Poisson solver, but are in any case much less important.

From the parameters defined in Figure 4.4, it is found that $d_{per} = 35 \mu\text{m}$, which corresponds to $k \approx 36$ in terms of the units shown in Figure 4.4, and is approximately the scale of the gap between the paper surface and the toner layer, d_{gap} . The inset of Figure 4.4 compares the electrostatic field from our full model to the one-dimensional model (i.e., Equation (4.21)) using a local surface thickness

reconstructed only from the lower frequency principle modes $k = 2, 5, 20$ of the original surface. With the exception of the boundaries, the one-dimensional approximation is quite good.

As a comparison, Figure 4.5 shows the similar results for a surface reconstructed using cosine wave perturbations.

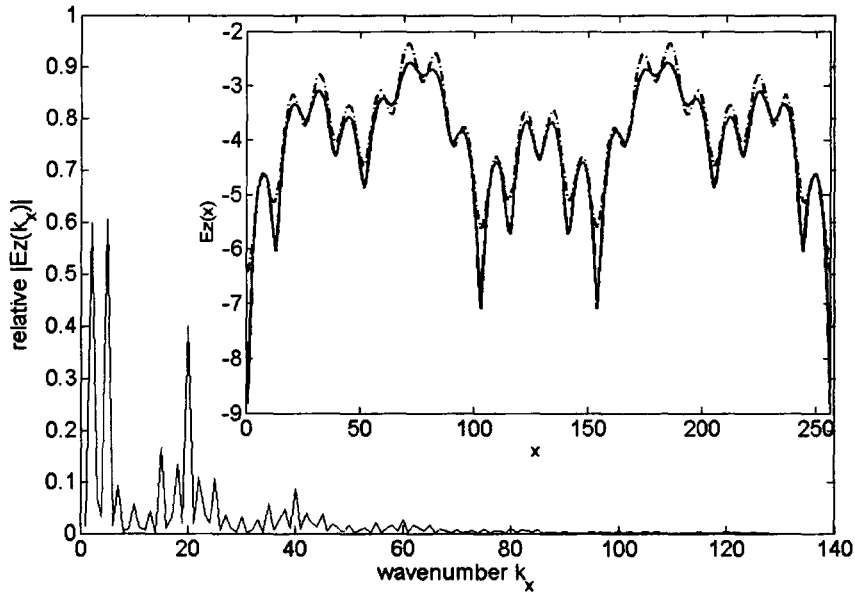


Figure 4.5 Power spectrum of the z-component of the electric field vs. wave number k for the case of cosine wave perturbation of the paper surface. Frequencies used are the same as in the data of Figure 4.4. The inset compares the real-space z-component of the electric field obtained from the full solution of the Poisson equation to the multi-layer 1D model that uses the principal modes of $k = 2, 5, 20$ to reconstruct the local surface roughness. Other parameters are as defined in Figure 4.4.

It is clear that the matching in the boundary region between the full Poisson solver and one-dimensional approximation is excellent. This excellent match is presumably due to the fact that cosine form of surface perturbation is consistent with non-flux boundary condition imposed in our full 3D Poisson solver.

These results indicate that for *filler-free* paper, only surface heterogeneity with in-plane variations on the scale of $\lambda \geq 3d_{gap}$ contribute significantly to variations in the electrostatic field. Moreover, their effect can be modeled with a 1D capacitor model. Smaller-scale surface variations add only small corrections to the electrostatic field, on length scales smaller than d_{gap} , which must be modeled accurately using the full model. The principal mode analysis also reveals that there is some degree of mode mixing that gives rise to electric field variations at intermediate frequencies between those of the bare paper surface.

The Fourier analysis of paper surface roughness can also be extended to two-dimensional paper surface. The paper surface in this case is modeled as a superposition of two dimensional cosine waves of the form $H = \bar{H} + A \left[\sum_k \cos(2\pi x/\lambda_k) \right] \left[\sum_k \cos(2\pi y/\lambda_k) \right]$ where $A = 1.2 \mu\text{m}$, $\bar{H} = 80 \mu\text{m}$ and λ_k are the same as those defined in Figure 4.4. It is found that the dominant Fourier modes in the electric field have a one-to-one correspondence to modes defining the paper surface. Moreover, the various modes are decoupled in each direction as shown in Figure 4.6.

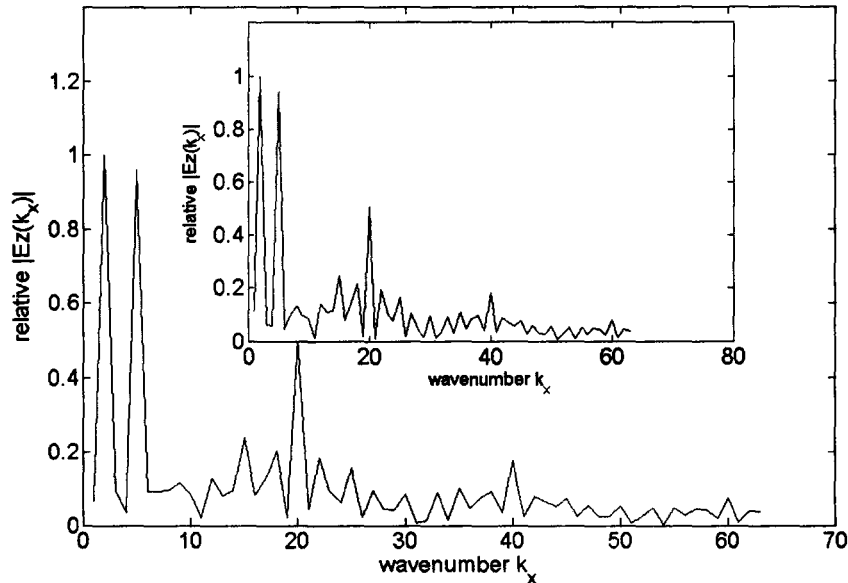


Figure 4.6 Power spectrum of the electric field vs. wave number in x direction with $k_y = 2$. In the inset shows the plane $k_y = 5$. Other parameters are as defined in Figure 4.4

4.4.2 Effect of Filler and Porosity Fluctuations

4.4.2.1 Surface Filler

Filler is an important component of commercial paper. It is used to provide opacity and to reduce fiber costs. Non-uniformity in filler distribution has previously been conjectured to cause electric field variations in the toner layer (Cassidy 2004). The causal connection between filler/surface variations and the toner transfer field can

now be made more quantitative using the principal mode analysis presented above.

Figure 4.7 shows that adding filler particles into valleys *corresponding to short wavelengths* of the paper surface has no effect on electric field, consistent with the principal mode analysis above.

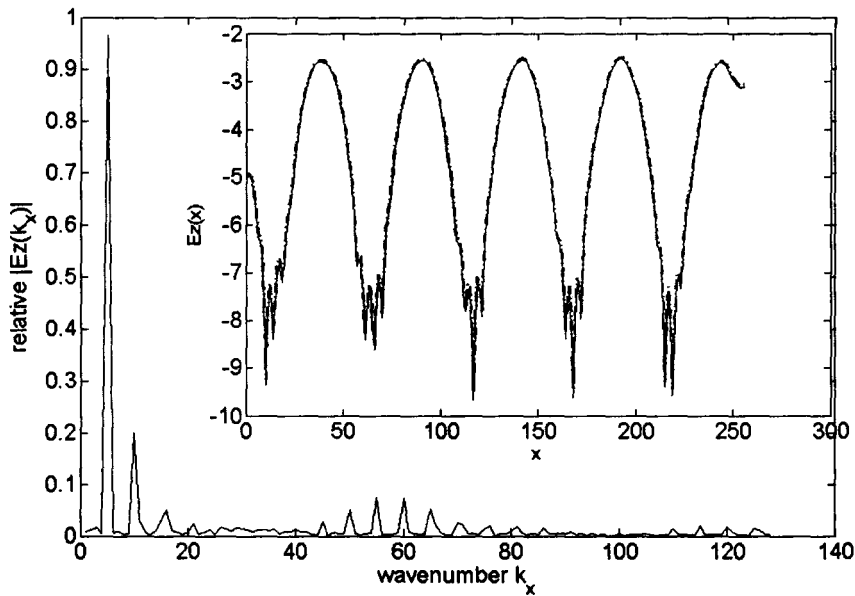


Figure 4.7 Power spectrum of the z-component of electric field obtained from the numerical solution of the Poisson equation for the case where the paper surface is a superposition of sine waves of frequencies $k = 5, 60$ and equal amplitude of $15 \mu\text{m}$. Inset: filler particles of size $5 \times 2 \mu\text{m}$ are distributed across the surface at a frequency corresponding to $k = 60$. The inset compares the z-components of electric fields obtained from the full solution of the Poisson equation with and without a filler particle in each valley of paper surface. Other parameters are the same as in Figure 4.4.

When filler particles sit in the valleys of a paper surface *corresponding to long wavelengths*, a different picture emerges, as shown in Figure 4.8.

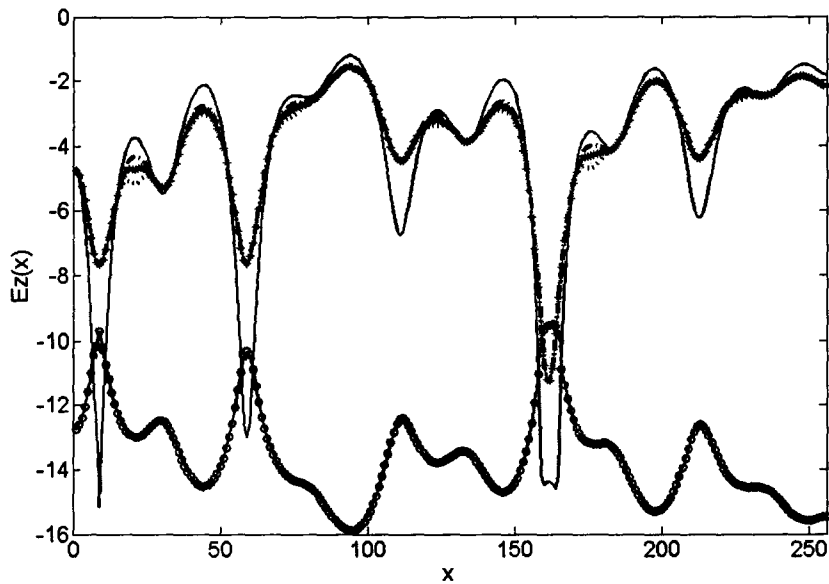


Figure 4.8 Plot of the z-component of electric field (solid line) obtained from numerical solution of the Poisson equation for a paper surface described by the form $H = \bar{H} + A \sum_k \sin(2\pi kx/L)$, where $k = 2, 5, 10$, $\bar{H} = 80 \mu\text{m}$, $A = 10 \mu\text{m}$. The figure also displays the electric fields after the insertion of filler particles in the valleys of the paper surface. In each valley of the paper surface corresponding to $k = 10$, filler agglomerates of size $5 \times 4 \mu\text{m}$ (dash-dotted line), $5 \times 8 \mu\text{m}$ (star line) and $15 \times 8 \mu\text{m}$ (dotted line) are inserted. For comparison, the z-component of electric field with filler particles fully filling the gap between paper surface and the bottom of toner layer (open-circle line) is also shown in the figure. All other units are as in Figure 4.4.

Specifically, when filler particles of size $5 \times 4 \mu\text{m}$ are inserted in each valley, the resulting electric field is strongly modified from what it was without any filler. In particular, the magnitudes of electric field corresponding to paper surface valleys where filler particles are inserted are increased (i.e. more negative as shown in Figure 4.8). This feature can be easily explained using our principal mode analysis above.

A much more surprising and interesting feature is that the strength of electric field corresponding to paper surface peaks is reduced. This feature is due to mode mixing, which results in the reduction of *effective* surface peak height. We note that the peak magnitudes of the electric field do not change any further if more filler particles are further added within the valleys of the surface, indicating no further mode mixing occurs.

Figure 4.8 also plots the total z component of the electric field when all the space between the paper surface and the bottom of toner layer is fully filled with filler particles. In this case, the mean value of the transfer field increases. Interestingly, however, the degree of electric field fluctuation in this case is comparable to that when only single filler particles are sitting in the valleys.

To summarize, the positioning of filler particles only in the long wavelength valleys of the paper surface is effective in reducing the electric field *fluctuations*, *without* changing the overall mean toner transfer force very much. On the other hand, heavy coverage of the surface and valleys with filler will shift the overall toner

transfer force significantly, but will not be more effective in reducing the point-to-point variation in the toner transfer force. It is noted that the second scenario is relevant to the case of surface coating in commercial paper.

4.4.2.2 Bulk Filler

The effect of filler particles distributed inside the bulk of the paper was studied on the resulting electric field non-uniformity in the toner layer. For simplicity, it is assumed that paper surface is perfectly smooth, with a thickness of $81.25 \mu\text{m}$. Filler particles of volume fraction of 20% are either distributed near the top or bottom surface of the paper, or throughout the paper bulk.

The resulting electric field measured along the center line of toner layer is shown in the inset of Figure 4.9. The mean value of the electric field in the three different cases is the same, and can be predicted by the 1D model (i.e., Equations (4.22) and (4.23)) based on the mean of the total heights ($\sum d_{i_{filler}}$) of the filler layer (i.e., $81.25 \mu\text{m} * 20\%$) and the paper layer ($81.25 \mu\text{m} * 80\%$) with relative error of only a few percent.

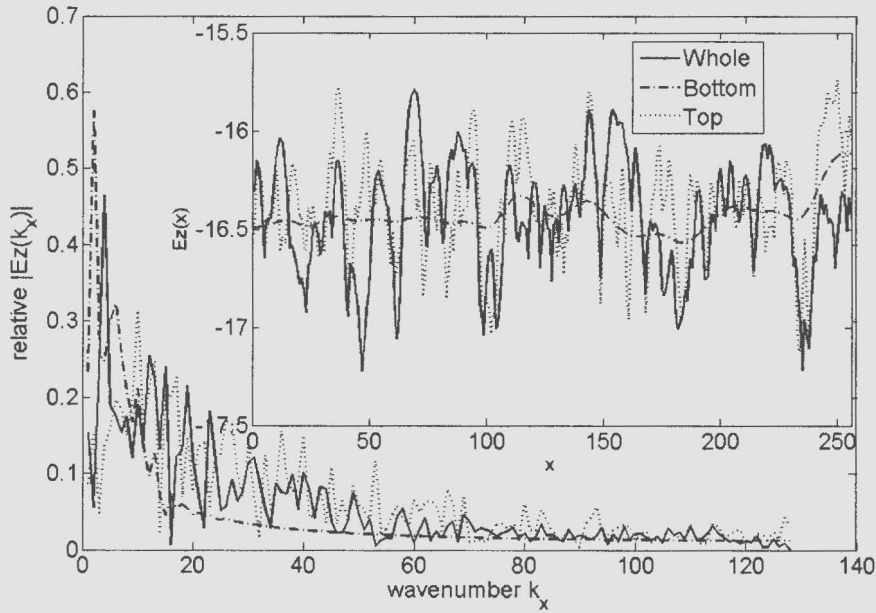


Figure 4.9 Power spectrum of the z-component of the electric field obtained from the full solution of the 3D Poisson equation. Filler particles follow a uniform-random spatial distribution and are deposited near the top surface of the paper (dotted line), bottom paper surface (dash-dotted line), or distributed throughout the entire bulk (solid line). The paper is idealized to have zero roughness and a caliper (thickness) of $81.25 \mu\text{m}$. In all the cases, the total volume fraction of filler particles is 20%. The size of filler particle occupies one unit cell, $5 \times 1.5625 \mu\text{m}$. The thickness of toner and photoconductor layers are the same as in Figure 1. In the inset, the z-components of electric fields along the middle of toner layer are shown for the three cases. All other units are the same as in Figure 4.4.

The inset of Figure 4.9 shows that paper containing a significant near-surface distribution of filler generates the largest fluctuations in the electric field within the toner layer. Paper with filler buried deeper into the paper generates much smaller

electrical field fluctuation, merely acting to shift the overall increase in the mean transfer force from what it was in the absence of filler.

These observations can also be explained in terms of the principal mode analysis of the previous section. Filler particles distributed deeper into the paper substrate, which establishes a larger cutoff wavelength d_{per} , which implies that as filler penetrates deeper into the paper, its effect is manifested on increasingly longer wavelength of the electric field. This result is also consistent with the empirical finding of reference (Cassidy 2004).

A Fourier analysis of the integrated filler particle thickness in the z direction, at each x, y position, is performed. This is shown in Figure 4.10 for the case where filler particles are distributed throughout the paper bulk.

In the same figure, the power spectrum of the electric field is also displayed. It can be clearly seen that at long wavelengths ($k \leq 5$, which corresponds to $\lambda \geq 3d_{per}$, where $d_{per} \approx 86 \mu\text{m}$ is close to the thickness of the paper substrate), the peak positions in the power spectrum of the integrated filler distribution and electric field perfectly match with each other. Between wavelengths d_{per} to $3d_{per}$, which corresponds to $5 \leq k \leq 15$, the matching between the two are reasonably good.

To decipher the *dielectric signature* of filler at different penetration depths, the integrated power spectrum of the filler, obtained by summing the power spectra of the dielectric distribution in each layer, is examined across all layers in the z-direction of

the paper. It is noted that in each layer (value of z) the resulting power spectrum of the dielectric distribution was re-scaled as follows: Fourier components with wavelength greater than $3d_{per}$ are assigned weight factor of 1, while high frequency components with wavelength shorter than d_{per} are discarded. Wavelengths in between are assigned weight factor between 0 to 1 using linear interpolation. (We note that d_{per} is increasing from the top-most layer down to the bottom layer).

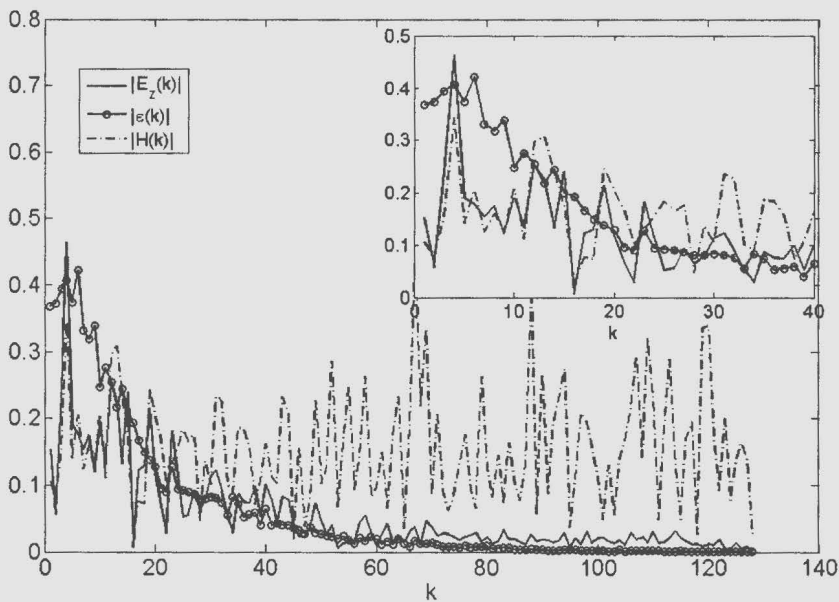


Figure 4.10 Power spectra of: the z -component of the electric field obtained from our 3D Poisson solver (solid line), the integrated filler particle thickness in z direction at each lateral position (dot-dashed line) and the integrated power spectra from the complete dielectric distribution from all layers across the paper thickness (open-circle line). For this simulation, filler particles are uniformly-randomly distributed inside the entire bulk with 20 % volume fraction. Other parameters are the same as in Figure 4.9. The inset is the blow-up of the plots in long wavelength regime. The vertical scales are arbitrary.

The summation of the filler power spectra from all paper layers is also shown in Figure 4.10, indicating the matching with electric field pattern in long wavelength regime is not as good as integrated filler thickness. The data shows that at long wavelength, peaks in the spectrum of the electrical field are almost identically commensurate with those of the integrated (z-direction) filler thickness distribution. Conversely, no single layer, acting separately, can be said to control the long wavelength variations of the electrical field. These results imply that with regard to bulk filler, it is the spatial distribution of integrated filler content (in the z-direction) that controls the spatial variations of electrical transfer field, and not the filler variation from any particular layer in the paper.

4.4.2.3 Porosity

A similar power spectral analysis as above can be applied to study the effect of the total mass distribution of paper, which is referred to as paper *formation*. First the simplest case of a uniform-random distribution of air pores in an otherwise uniform paper substrate is considered. Similarly to the case of filler distribution, power spectrum peaks of the integrated thickness of air pores at each lateral position are commensurate with those of the electric field in the long wavelength limit.

Chapter 5

The Role of Paper Structure Heterogeneity in Xerography

5.1 Analysis of Electrostatic Field in Toner Layer Using Simulated Paper

We now turn to the case of a substrate in the printing nip that is heterogeneous in all of its paper-related measures. Paper being the ideal candidate, we used the simulated paper webs as discussed in chapter 3 as input to the 3D Poisson solver to study the effects of paper surface roughness and paper formation (i.e. porosity) on the distribution of the electric field in middle of the toner layer.

Figure 5.1 displays the power spectra of the electric field, the paper surface height as well as the integrated pore thickness (in z-direction) distribution. The simulated paper corresponded to a 36.00 g/m^2 handsheet. The simulated area over which properties were analyzed was $5\text{cm} \times 5\text{cm}$. The integrated air pore distribution is based on the total air height in each lateral position, and thus has the same units as the surface height, although it is actually a measure proportional to the local mass density. Thus, given the linear nature of Poisson equation, the relative intensities of the power spectra of surface height and air pore distributions can be seen as indicative of their relative contribution to the electric field, at any given wave vector.

Comparing the relative intensities and peak positions of the surface roughness and integrated pore height, it is predicted that the long wavelength non-uniformity of

the electric field will be predominantly controlled by surface height variations at similar wavelengths. It is noted that the correspondence of the peak positions of the surface and electric field is also consistent with the principal mode analysis in chapter 4.

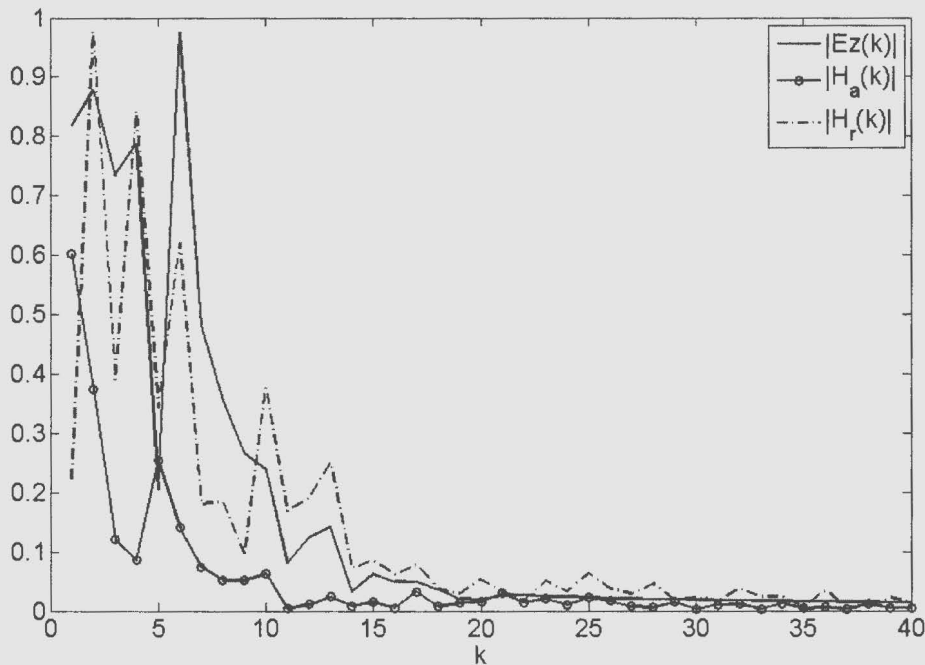


Figure 5.1 Power spectra of: the z-component of the electric field (solid line) obtained from our 3D Poisson solver using a simulated 3D paper web, the surface height (dash-dot line) of the simulated paper web, and the distribution of integrated pore heights at each lateral position (open-circle line). The x-axis corresponds to wave number k_x and we have set $k_y = 2$. The wave number is in units of $2\pi/L$, with $L = 512 * 5 \mu\text{m}$.

It should be noted that in commercial paper, based on the density of pure fiber and the mass density of paper (paper mean thickness about 80 μm), it is found that the total air content inside paper is in between 60% to 70% by volume, with most of the mass of the paper coming from pure cellulose. Since this 3D fibre network model neglects the hollow centre of a fibre, our simulated paper webs under-estimate the air fraction in a paper web. Thus, in commercial paper, porosity is expected to play an even smaller role than that predicted in Figure 5.1.

As a consistency check, a power spectral analysis of paper surface height and integrated pore height distributions in the laboratory handsheet samples were also performed. Figure 5.2 shows these measures for one of our samples of size 3200 x 3200 μm . Since the resolution of our formation measurements is limited to 100 μm , the paper surface height profile is also coarse grained to 100 μm .

Simulations of other basis weight handsheets also predicts that the relative variations of paper surface roughness from the length scales of 0.1 mm to 3.2 mm are much stronger than those of air pores inside the paper bulk, consistent with the results of Figure 5.1. Thus it is expected that for the simulated handsheets, variations in the toner forces (and, consequently, toner mottle) will be controlled almost entirely by surface height variations and *not* by porosity variations, i.e. formation.

The results of data such that of Figure 5.1 are noteworthy from the point of view that the paper manufacturing industry has consistently in the past relied on formation

as its main quality control index in many applications of paper. These results and the once to be discussed below will strongly challenge that position.

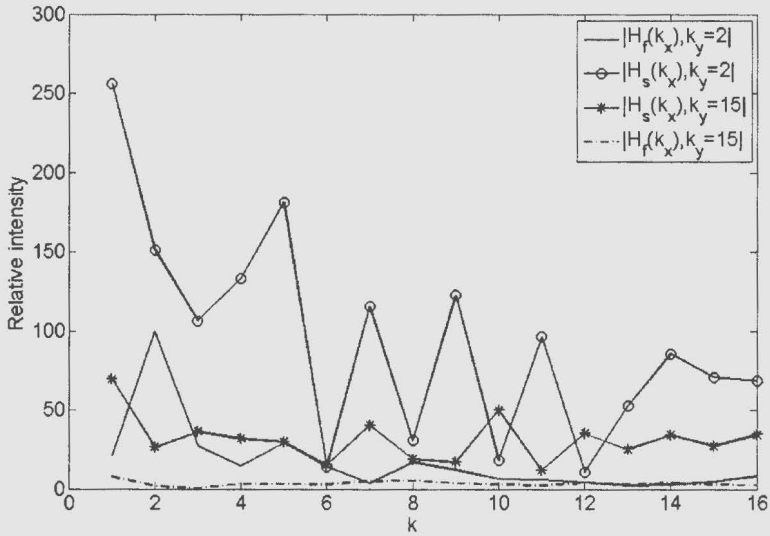


Figure 5.2 Comparison of power spectra of surface height (open-circle line for $k_y = 2$, starred line for $k_y = 15$) and of the integrated air height distribution (solid line for $k_y = 2$, dash-dot line for $k_y = 15$) for our laboratory handsheets.

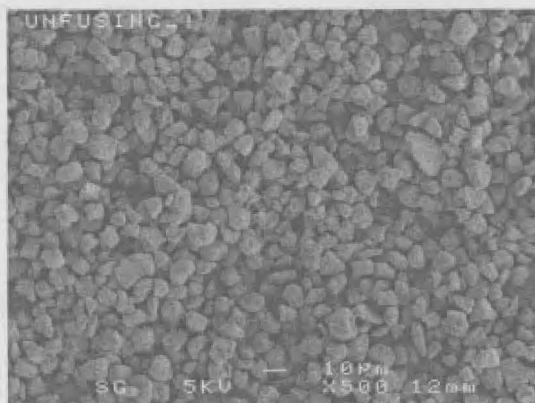
5.2 Predicting Toner Density Distribution onto Paper

5.2.1 Toner Transfer Experiments

Black toner was transferred onto a $5 \times 5 \text{cm}^2$ area of several laboratory handsheets samples prepared according to TAPPI Standards using a Xerox DocumentColor 12 copier in XRCC. This copier was modified so that the machine could be stopped before the paper went into the toner fusing stage. In this way, toner distribution properties can be examined only by the electrostatic transfer.

The printed sample was scanned using a high resolution scanner to obtain maps (i.e. spatial distributions) of reflected light intensity from the toner layer. This was a measure often used in paper research to quantify print mottle. Using the Image Processing Toolbox in Matlab, the image information from the reflected light was converted to digitally grayscale stored as a two dimensional array. This data was indicative of the toner density distribution on the printed area. The size of the printed zones that were scanned was dictated by the largest possible volume (i.e. *memory*) of paper that we can manipulate in our present computing facility when simulating the Poisson Equation (4.4).

Three sample areas of 36g/m^2 basis weight handsheets of average thickness $80\ \mu\text{m}$ were printed with black toner ($5\times 5\text{cm}^2$ area), following the method introduced above. Figure 5.3 shows an SEM image of toner particles distributed on an area of a typical handsheet sample surface. From the image it can be seen that the toner particles on the sample are non-uniformly distributed and that there is essentially one layer of toner transferred to the sample.

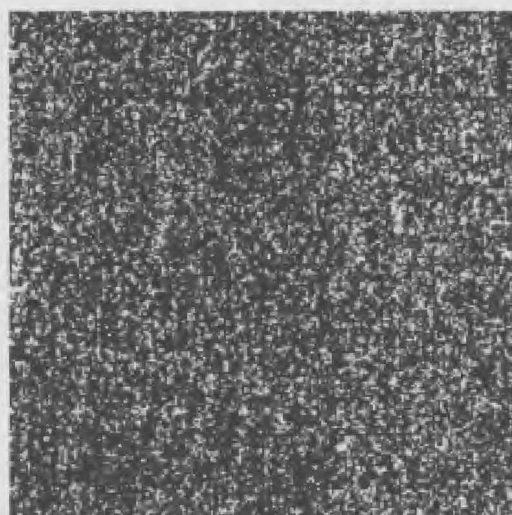


(a)



(b)

Figure 5.3 SEM image for toner particle distribution on a laboratory handsheet sample, under (a) 500x magnification, (b) 100x magnification.



1mm

Figure 5.4 Reflected light distribution of a $5 \times 5\text{mm}^2$ section of paper covered by toner.

Two $5 \times 5 \text{mm}^2$ areas from the centre of each printed sample area were scanned and the reflected light was transformed into a light intensity map. A typical such map of reflected light is shown in Figure 5.4.

The reflected light intensity from the six images of the six $5 \times 5 \text{mm}^2$ sub-sections cut out from our printed samples, were processed by Matlab. The 2-dimensional arrays obtained for digitalized grayscale was analyzed by using principal mode analysis. Figure 5.5 shows the averaged power spectrum from the six images.

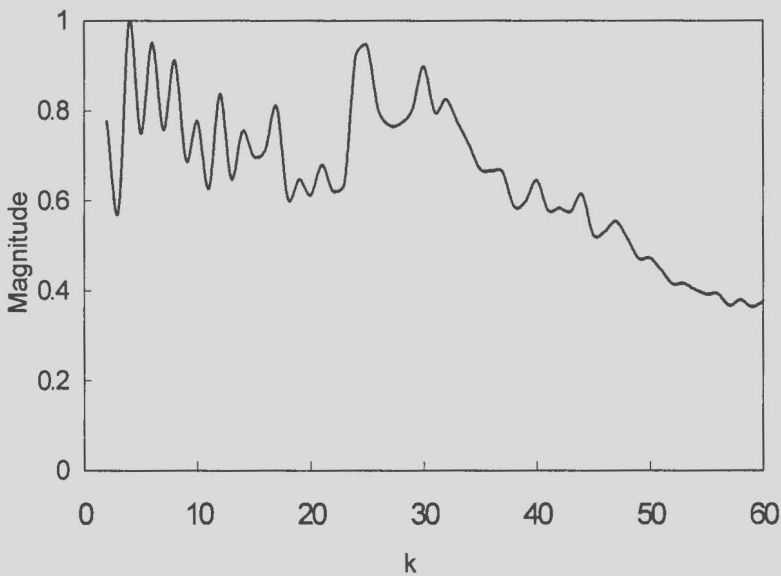


Figure 5.5 Power spectrum of toner density distribution obtained from experimentally printed zones (solid line). The x-axis corresponds to wave number k . The wave number is in units of $2\pi/L$, with $L = 512 \times 5 \mu\text{m}$

5.2.2 Comparison of Experiments and Simulations: The Importance of Paper Deformation and Contact Adhesion in the Print Nip

In the discussion of section 5.1 it was assumed that the electrostatic field responsible for transferring toner to paper is established entirely by the *original* paper structure. However, when comparing the power spectrum of experimental toner density distribution from experimental paper samples (e.g., Figure (5.5)), with that of the z-component of the electrostatic transfer field obtained from the 3D Poisson solver using a simulated handsheet paper shown in Figure 5.6, there is *little similarity* between the two power spectra, except at the very longest wavelengths.

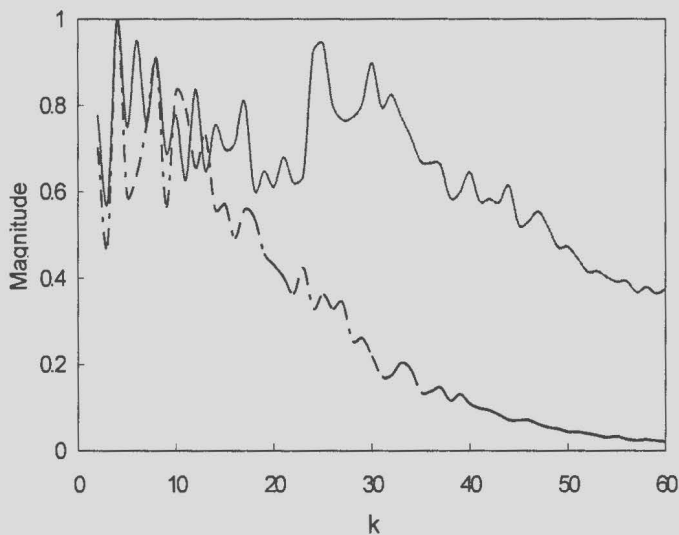
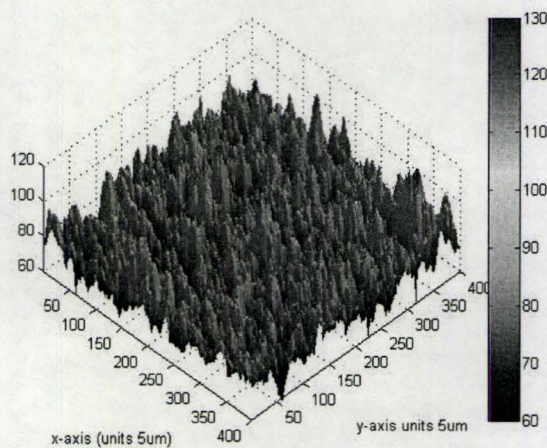


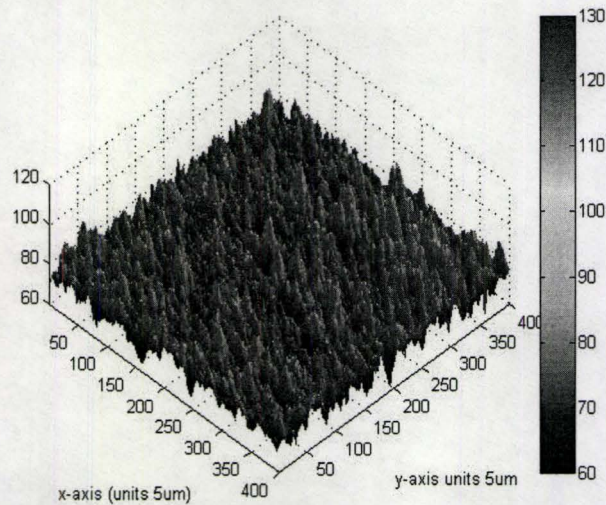
Figure 5.6 Power spectra of: (i) z-component of electric field predicted from simulated handsheet paper webs (dash-dotted line) that do not deform at all in the print nip; and (ii) toner density distribution obtained from experimentally printed zones (solid line). The x-axis corresponds to wave number k . The wave number is in units of $2\pi/L$, with $L = 512 \times 5 \mu\text{m}$

The answer to this dilemma may lie in two factors that we have neglected thus far: (i) paper deformation under the printing nip, (ii) toner paper and tone-photoreceptor adhesion, or (iii) both. During the transfer process, it is reasonable to expect that papers passing through a print nip will experience a certain degree of surface deformation, which will in turn affect the electrostatic and contact adhesion landscape controlling toner transfer onto the paper. This hypothesis is supported by recent experimental work (Rimai 2004, Wright 2005, Rimai 2003).

Surface deformation of simulated webs was discussed in chapter 3. Figure 5.7 shows (a) the simulated handsheet before compression; and (b) the simulated handsheet after compressive loading that compresses the paper by a strain of 0.083 of its maximum asperity height. The effect of compression on the simulated paper web was simulated using the stress vs. strain response of Equation 3.28, which was applied incrementally to each in-plane ‘paper spring’ of the paper web.



(a)



(b)

Figure 5.7 Simulated paper surfaces before (a) and after (b) compression. The axes are scaled in units of $5 \mu\text{m}$. Paper basis weight is 36 g/m^2 and average paper caliper before compression is $80 \mu\text{m}$. The paper is compressed to a mean strain of 0.083.

In addition to the electrostatic forces acting on toners, it is also reasonable that contact adhesion forces must also be considered in predicting toner transfer. Toner transfer prediction thus needs to incorporate paper-toner and toner-photoreceptor contact forces on toners. Based on the experimental and theoretical research on adhesion forces that have been studied in the literature, several forces can be applied to individual toner particles. These are illustrated in Figure 5.8. These include the van der Waals force between toner particles and photoreceptor, as well as the Electrostatic adhesion force from photoreceptor. These are referred to as “adhesion forces”, which

resist transfer of the toner particles from photoreceptor to paper substrates.

The primary dragging force is from the electrostatic transfer force, which is calculated from the 3D Multigrid Poisson solver. The van der Waals force between the toner particles and paper substrates will help to drag down the toner particles, but this force varies with the paper surface roughness. If at some places where toner particles contact the paper surface during the transfer process, this additional dragging force (van der Waals force between the toner particles and paper substrates) will exist and the toner particles can be more easily transferred onto the paper; Otherwise, only the electrostatic force acts on the toner particles, which may make it more difficult to cause transfer.

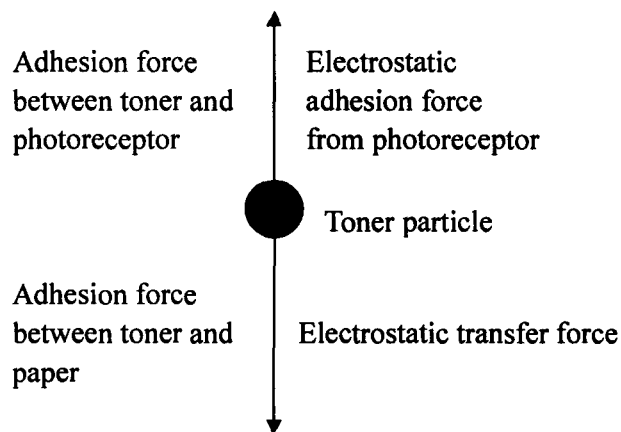


Figure 5.8 Illustration of various forces that may act on a toner particle.

Modelling the toner transfer process algorithmically is done as follows: if a toner particle resides over a paper valley where there is no direct contact between toner particle and the paper surface, a 500nN contact adhesion force is active in the positive z direction (toward the photoreceptor). Otherwise a net adhesion force of 100nN is applied to the toner in the positive z-direction, because the contact between toner and paper surface will offset most of the toner-photoreceptor force. This can be altered according to specific adhesion measurement data. The electrostatic bias field calculated from Equation (4.4) is always in the negative direction (toward the paper).

Toners with a net force (adhesion plus electrostatic bias) in the negative direction are marked for transfer onto the paper, otherwise they do not transfer. The final *simulated* toner density distribution thus simulated is then coarse-grained to the same resolution as the toner transfer experiments described in section 5.2.1, the resolution of which in this work is $50\ \mu\text{m} \times 50\ \mu\text{m}$.

Figure 5.9 shows the details of the complete simulation platform for computing toner transfer density distribution, which includes different 3D paper structures under different states of paper-nip deformation, and which accounts for both electrostatic and adhesion forces acting on toner particles.

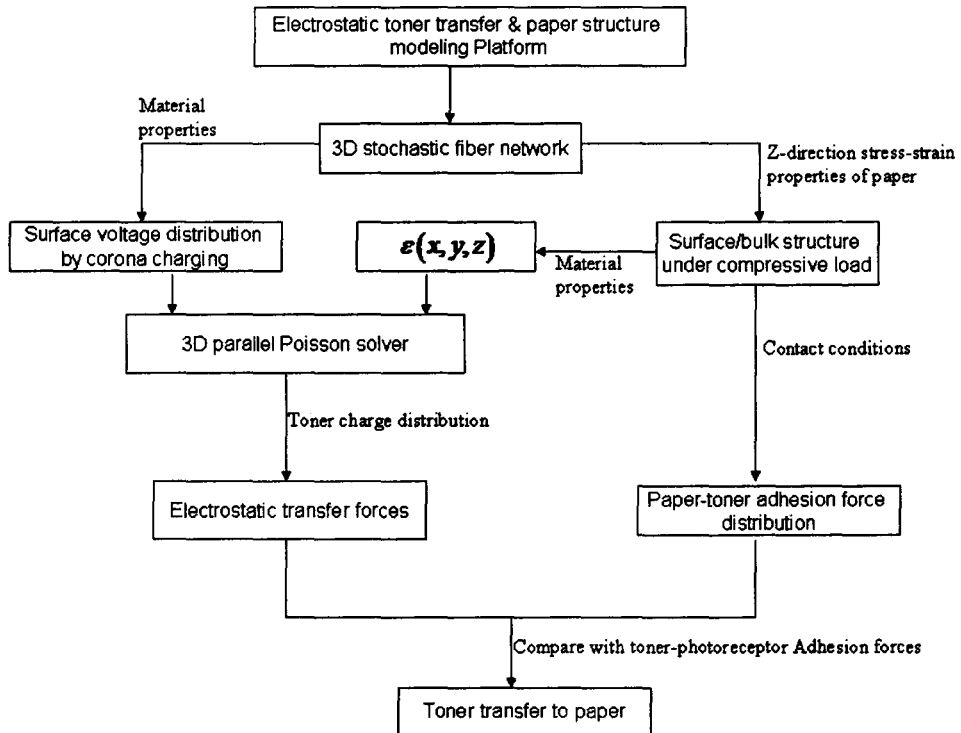


Figure 5.9 Schematic of the toner transfer and paper structure modeling platform

5.2.3 Comparison of Simulations and Experiment: Predicting Toner Density Distribution

This section examines the combined effect of paper structure heterogeneity and paper-nip interactions on toner transfer. It compares simulation results from the new modeling platform with the toner transfer experiments described in the previous section, identifying attributes of paper structure and paper deformation which affect toner transfer.

Several simulated handsheet samples analogous to that in Figure 5.7(a) were generated. Simulated handsheets had the same initial surface, thickness and mass density statistics as the laboratory handsheets discussed in chapter 3. These ‘virtual’ handsheets were then compressed to several strain levels (0.05, 0.10, 0.20) of their maximum asperity height, yielding surfaces analogous to that shown in Figure 5.7(b). The power spectra of mass density variation (formation) and surface variations of the resulting simulated handsheets were computed, as well as the power spectra of the predicted toner distribution onto these virtual handsheets. Finally, the power spectra of the experimental toner distributions described in the previous section were also obtained. Power spectra from the experimental zones were averaged over the six printed zones to reduce statistical fluctuations. Power spectral analysis was used to help establish a correspondence in length scales between different signals that are noisy under visual inspection.

The power spectra of the simulated toner distribution, obtained with different strains of compression (in the print nip) applied to virtual handsheets, were compared, which is shown in Figure 5.10. Also shown is the power spectrum of the toner distribution determined experimentally on the laboratory handsheets. Figure 5.10 isolates the case of 10% strain and the experimental toner transfer curve, shown in Figure 5.11.

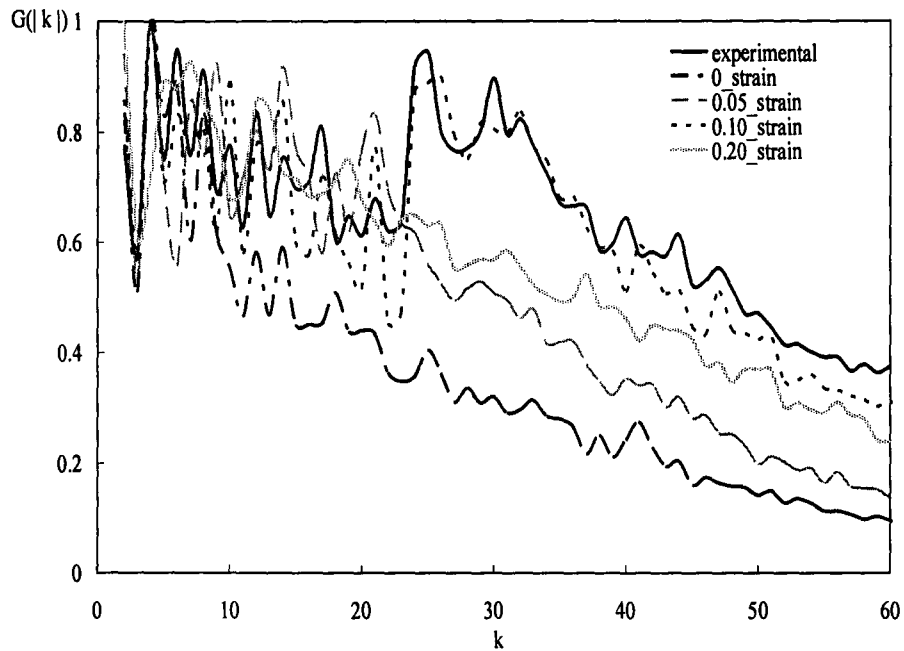


Figure 5.10 Circularly averaged power spectra of: (i) toner density distribution obtained from simulation without compression (dash-dotted line); (ii) toner density distribution obtained from simulation under strain 0.05 (dash line); (iii) toner density distribution obtained from simulation under strain 0.10 (dotted line); (iv) toner density distribution obtained from simulation under strain 0.20 (shadow line); and (v) toner density distribution obtained from experimentally printed zones (solid line). The x -axis corresponds to wave number k . The wave number is in units of $2\pi/L$, with $L = 512 \times 5 \mu\text{m}$

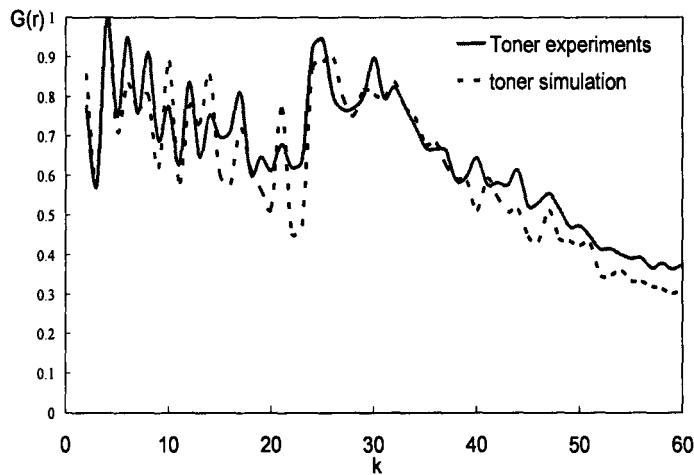


Figure 5.11 Circularly averaged power spectra of: (i) simulated toner density distribution obtained assuming a nip-strain 0.10 (dotted line) and (ii) toner density distribution obtained from experimentally printed zones (solid line). The x-axis corresponds to wave number k . The wave number is in units of $2\pi/L$, with $L = 512 \times 5 \mu\text{m}$.

The simulation data suggests that at wavelengths larger than $500\mu\text{m}$ ($|k| < 10$) paper compression does not play a large role in establishing the toner transfer distribution. *For smaller wavelengths the power spectra of the simulated toner transfer distributions yield a good correspondence with experiments only if a certain degree of paper compression is accounted for.* In this case, z-direction deformation of about 10% yields the best correspondence in the peak structure and general trend of simulated and experimental power spectra. We note that the average feature resolution that the human eye can resolve at normal reading distance is approximately $100 \mu\text{m}$.

To separate the effect of electrostatic field transfer and contact-mediated transfer, we compared the power spectra of the electrostatic bias field simulated with and

without 10% paper compression to that of the toner distribution determined experimentally. This is shown in Figure 5.12.

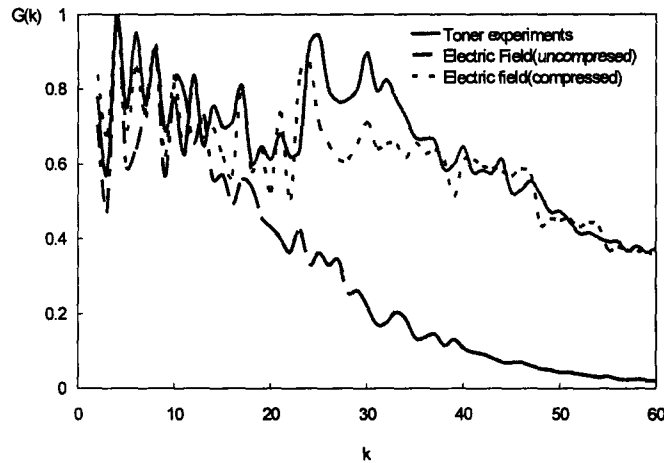


Figure 5.12 Circularly averaged power spectra of: (i) z-component of electric field corresponding to uncompressed simulated paper webs (dash-dotted line); (ii) z-component of electric field corresponding to compressed simulated paper webs (dotted line) and (iii) toner density distribution obtained from experimentally printed zones (solid line). The x -axis corresponds to wave number k . The wave number is in units of $2\pi/L$, with $L = 512 \times 5 \mu\text{m}$

Good correspondence in the peak positions and the morphology of the power spectra of the toner distribution and the electrostatic field is obtained in this situation, particularly at intermediate to long wavelengths (i.e., greater than $\sim 50 \mu\text{m}$). This is to be expected since the major transfer force acting on toner during transfer is that from the electrostatic bias field, which was shown to be “shaped” strongly by the surface topography.

We also compared the power spectra from simulated surface profiles corresponding to the 10% deformed and un-deformed paper with the power spectrum of the experimental toner density distribution. This is shown in Figure 5.13.

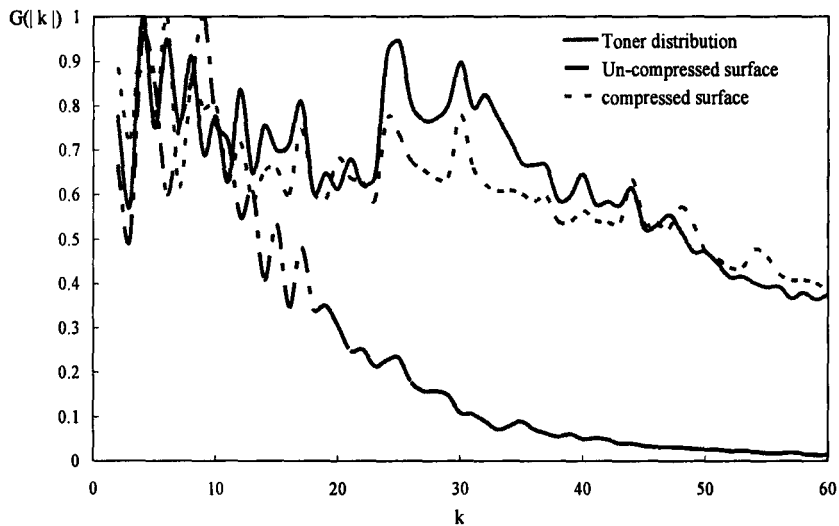


Figure 5.13 Circularly averaged power spectra of: (i) surface height of a simulated paper webs before compression (dash-dotted line); (ii) surface height of the simulated paper webs after compression (dotted line) and (iii) toner density distribution obtained from experimentally printed zones (solid line). The x -axis corresponds to wave number k . The wave number is in units of $2\pi/L$, with $L = 512 \times 5 \mu\text{m}$.

Figure 5.13 shows that the compressed paper surface topography corresponds very closely with toner density variations, over almost the entire range of wavelengths. This can be rationalized by noting that the surface of paper controls not only the electrostatic transfer field but also modulates the distribution of toner adhesion contact forces.

Finally, the power spectrum of the mass variation (i.e., formation) in our simulated paper webs was compared with the toner density distribution from our experiments, shown in Figure 5.14.

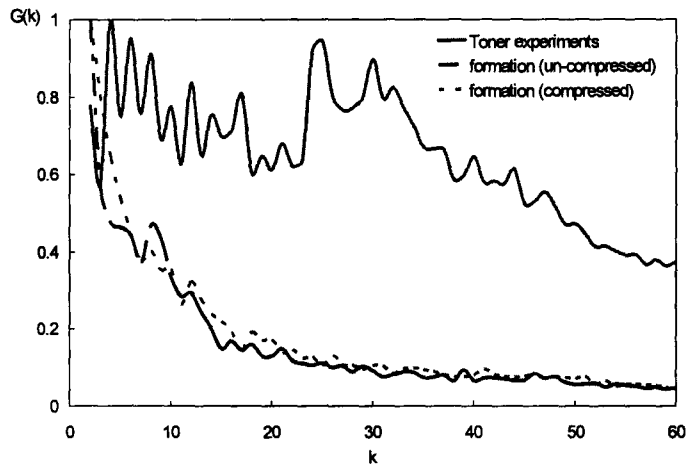


Figure 5.14 Circularly averaged power spectra of: (i) overall mass density from simulated paper webs before compression (dash-dotted line); (ii) overall mass density from simulated paper webs after compression (dotted line) and (iii) toner density distribution obtained from experimentally printed zones (solid line). The *x-axis* corresponds to wave number k . The wave number is in units of $2\pi/L$, with $L = 512 \times 5 \mu\text{m}$

The data shows that there is very little correspondence between spatial variations in toner density and mass density at any wavelength. It is also clear that the formation is not correlated at all to the electrostatic field or surface profile. The latter result is explained by noting that surface profile variations occur closer to the toner layer than do bulk mass variations, thus exerting greater control on perturbations of the electrostatic field in the toner layer.

Interpreting the above results in the context of the principle mode analysis of chapter 4, suggests that at long wavelengths the net toner transfer force is controlled by the electrostatic bias field, which is in turn is predominately modulated by the *compressed* paper surface profile. On the other hand, as shown in chapter 4, the surface does *not* exercise much control over the electrostatic field at wavelengths smaller than about 50um. At these length scales, the good agreement between experimental and simulated toner transfer density is likely controlled by toner-paper adhesion forces, which are also modulated by the [deformed] surface profile.

These results suggest that the description of spatial variation of toner transfer requires detailed knowledge of the electrostatic toner transfer fields at long wavelengths and more precise information of toner adhesion forces with the photoreceptor and paper at small length scales.

The most important prediction of this chapter is that the effect of the nip-deformed paper surface is the most important measure of paper quality when assessing the role of commercial paper grades on Xerographic print quality. Indeed, our results would appear to point away from using traditional paper formation as the most important index to asses print quality. However, it should be noted that it may assessing the paper topography under a state of nip-compression may pose significant problems experimentally. It is expected that this problem can be resolved by combining experiments with paper surface characterization with modeling work such as that presented in this thesis.

Chapter 6

Conclusion and Future Work

6.1 Conclusion

In this PhD work, the 3D fibre network model was successfully calibrated by the experiments. The experimental work proves that the 3D fibre network model can be used to model realistic paper structures, by comparing the mean mass, mean thickness, mass distribution and roughness distribution between experimental and simulated paper webs.

Micro-indentation tests were used to obtain stress-strain properties of paper. Different indenter radius pressing on different basis weight of paper was studied. It is proved that they can be scaled to one universal stress-strain curve with the additional effective radius, because of fibre-crossing in the paper structure. It is found that this additional effective radius decreases with increasing the indenter radius or decreasing the paper basis weight (thickness). Finally, an equation was generated to obtain the stress-strain behavior vs. indenter radius pressing on different basis weight of paper. This equation was used to predict the stress-strain property of paper between the printing nips.

An efficient 3D multi-grid Poisson solver was developed to directly calculate the electric field arising from complex simulated paper structures, which can be input from a 3D stochastic fibre network model of paper.

A 1D analytical model of electrostatic toner transfer, which was analogous to that developed by Yang-Hartmann (Yang 1976) and re-visited more recently by Kallunki et al. (Kallunki 2005), was also developed. A key difference in our approach was that this 1D model involves multiple dielectric layers, making it possible to incorporate *local* information about the integrated thickness of multiple paper constituents. The thickness of each constituent at any lateral position can be defined mathematically, or extracted from 3D simulated paper webs. These models were used to study how spatial variations in paper surface height, filler and porosity distributions affect electrical forces acting on a toner particle.

We calculated the electrostatic toner transfer field for the case of a paper substrate whose surface was analytically defined to be a summation of various frequencies. The main result of this analysis was that long wavelength variations of the electrostatic transfer field corresponded very closely to the same length scales of variation in the paper surface. Conversely, surface variations on smaller length scales did not display any relevant effect on the electrostatic field. It was also shown that the exact solution of the Poisson equation can essentially be reproduced by our 1D local capacitor model using only the long wavelength components to reconstruct the paper

surface (i.e. wavelengths larger than $3d_{per}$)

We also examined the role of surface and bulk filler on the electrostatic transfer field. Our results showed that surface filler distributed on small wavelengths across the surface does not alter the electrostatic “signature” created by surface height variations alone. Conversely, surface filler distributed in the long wavelength valleys of the surface leads to mode mixing, which actually reduces the peak-to-peak fluctuations of the electrostatic field. Furthermore, for filler distributed throughout the bulk, we found that the relevant measure controlling electrostatic variations is the integrated filler thickness in the z-direction of the paper.

We believe that the modeling platform developed in this work can be used to simulate a wide variety of complex paper structures, and to diagnose how their statistical attributes will affect electrostatic toner transfer field. We used simulated paper webs (without filler) to analyze the *combined* role of surface roughness and formation on the electrical field in the toner layer during transfer. Specifically, we found that long wavelength variations of electric field (i.e. peaks in the power spectrum) correlate almost perfectly with those of the surface height variations. *Formation* was not found to play an important role in controlling the toner transfer force field fluctuations.

A new modeling platform was introduced for computing how virtual paper structures *and* paper-nip interactions influence the toner density distribution in

Xerography.

Comparison of our simulations with experiments indicates that above visible length scales (long wavelength scales, bigger than 50 μm), toner density variations on printed handsheets are strongly correlated to those of the paper surface profile *under a state of compression*, which directly shapes the electrostatic field in the print nip. This suggests that the nip-*deformed* paper surface is critical in establishing the electrostatic field responsible for toner transfer onto paper, as well as controlling the print quality results in toner transfer process.

On the small length scales, it was noted that the toner density distribution is no longer correlated to the electrostatic transfer force distribution. In this regime, we believe that toner adhesion force becomes more crucial. As a result, the toner density distribution across all wavelengths is modulated by the *combination* of electrostatic transfer force and adhesion force on length scales comparable to toner particle sizes.

Our results proved that bulk mass density (i.e., paper formation), which is often linked to good or bad print quality, *is not a relevant index* in electrophotographic print quality. In manufacturing paper for digital printing, more attention should be paid to surface finish as opposed to the more traditional formation index. And we can conclude that the coating layer typically used to optimize the print quality is to improve the surface properties of the print substrate.

6.2 Future Directions

6.2.1 Moisture Distribution in Paper

Wood fibres in paper are hygroscopic — they absorb water readily. There are two ways for paper webs to absorb water: (i) free water goes to the pores between fibres and as intra-fibre free water in the lumen of fibres, (ii) bound water gets frozen to the pores of fibre walls (Gupta part1 2003, Gupta part2 2003) Thus, the distribution of water in paper substrate is following the fibre and pore distribution, which is non-uniformly distributed as well.

The dielectric constant of water is about 80, 20 times as that of cellulose (paper fibre is 4), 10 times as that of filler (about 8). In this thesis work, it has been already proved that the dielectric distribution greatly affects the toner transfer force. Thus, the water distribution in paper is another important effect which controls the distribution of toner transfer force. In future, it would be better to include the water distribution in this 3D paper structure model and the new platform.

6.2.2 Corona Charging

In toner transfer process, a conductor at high voltage can produce electric field of sufficient amplitude to transfer toner, however such devices often generate corona breakdown, or worse, sparking, by which about half of the energy is dissipated acoustically; thus the sound wave generates pressures sufficient to dislodge charged

toner and impair the quality of the transferred image.

A device, such as corotron, is used in high-speed copiers and printers. A nominal set of operating conditions- 6kV at the wire and 1.5kV at the outer cylinder - establishes a charge current of perhaps 120uA flowing to the paper, which generates enough voltage to transfer toner particles.

The space charge of the corona current has a complicated distribution, which will generate a complicated charge distribution on paper surface. After the charge from corotron devices spraying onto the paper surface, the retention of charge on materials is another problem.

A preliminary work has been done by measuring the 'self-dissipation' charge decay capability. A simple and easy to use approach for charge decay measurement is to use a high voltage corona discharge to deposit a small patch of charge on the material to be tested, move the corona charging electrodes quickly out of the way and use a fast response 'field mill' electrostatic field meter to measure how quickly the deposited charge migrates away by the decrease in the surface voltage. (Shown in figure 6.1) This arrangement has been described in a number of papers (British Standard 1996, Chubb 1990, Chubb 1996, Chubb 1999, Chubb 2000, Chubb 2002) and is included in a British Standard, (IEC 61340-2-1 2000) and an international standard (Gompf 1998). The experiments were conducted by using 'Jic155v5' at XRCC.

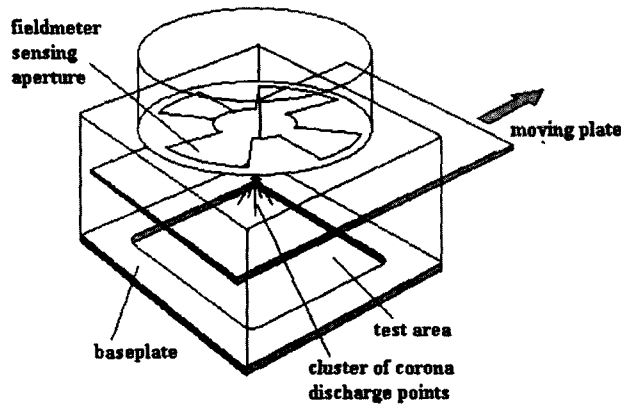


Figure 6.1 Arrangement for measurement of corona charge decay (copied from IEC 61340-2-1 2000)

Figure 6.2 shows the charge decay properties obtained for handsheet paper with different basis weight. The paper surface was charged by corona devices at 6 kV for 40 milliseconds. After the corona charging, the voltage on handsheet surface obtained the highest value, for about 800 V. Then the voltage decayed with the time, which means the charge flees away to the atmosphere around. Usually it takes about 100 milliseconds to finish the toner transfer process, thus about 400 V is the transfer voltage. It was noted that this voltage doesn't change with handsheet paper of different thickness.

We compared the charge decay properties between the handsheet paper and special made paper, which is made by depositing titanium dioxide particles on handsheets surface, in Figure 6.3. The filler particles, especially the coating layer on top of the paper, greatly affect the generated voltage and voltage decay property.

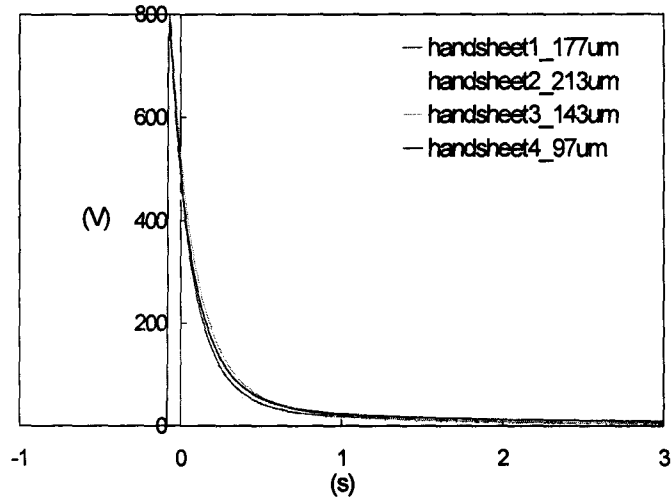


Figure 6.2 Charge decay curves for handsheets paper with different basis weight.

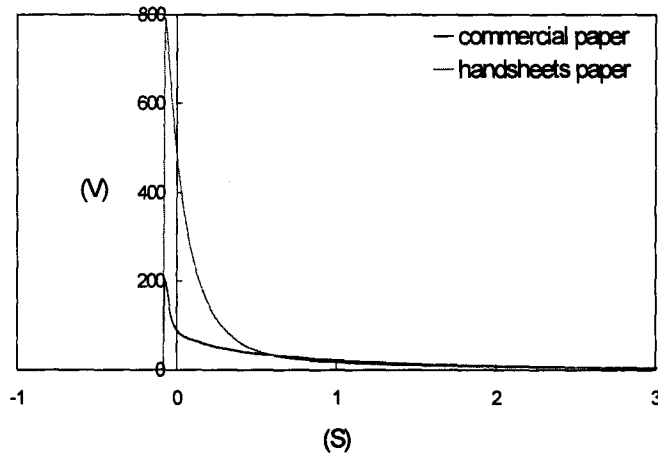


Figure 6.3 Charge decay curves for handsheet paper vs. special made paper.

Thus, to simulate the toner density in the toner transfer process of modern copier machine, the corona charging process should be included in the platform. The effects

from different paper properties (i.e. paper surface, paper formation, filler distribution, water distribution) on the corona charging should be studied in detail.

6.2.3 Effect from the Combination of Surface and Filler Distribution

The 3D Poisson Solver was modified and the dielectric constant distribution can be an input array. A 2D filler layer (dielectric constant is 9), which shows the distribution as in figure 6.4, was generated as a 2D array. This filler distribution can replace any layer in a 3D dielectric distribution (dielectric constant 4, uniformly distributed cellulose). The top layer, two middle layer and bottom layer, inside 3D dielectric was replaced by the generated filler layer respectively. The electrostatic transfer field under different condition was calculated by the 3D Poisson Solver.

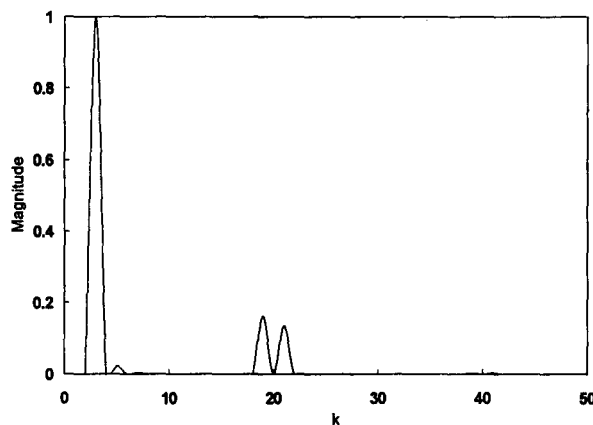


Figure 6.4 Power spectrum of the filler layer

Figure 6.5 shows the results. It was shown that the distribution of top layer filler has the most important influence on that of electrostatic transfer force.

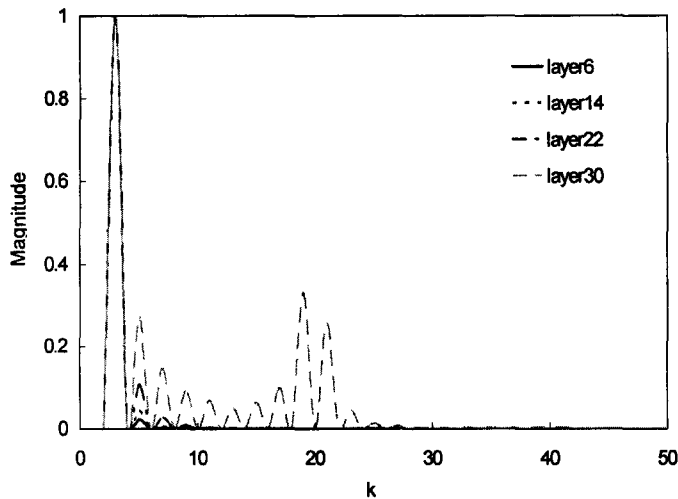


Figure 6.5 The power spectra of electrostatic transfer field from (i) filler layer replaces the bottom layer of 3D dielectric (dashed line); (ii) filler layer replaces the middle layer of 3D dielectric (dotted line) (iii) filler layer replaces the top layer of 3D dielectric (solid line)

Furthermore, the uniform 3D dielectric distribution for cellulose was modified, which involves a surface variation. The calculated electrostatic transfer field is shown in figure 6.6. The filler layer (shown in figure 6.4) was added to the top and the bottom of the new modified dielectric distribution respectively, the resulted electrostatic transfer fields are shown in figure 6.7 and 6.8. If the filler particles are on top of the surface, the filler and surface together control the electrostatic transfer field; However, if filler particles are located at the bottom, they have little influence and

only the surface variation controls the electrostatic transfer field.

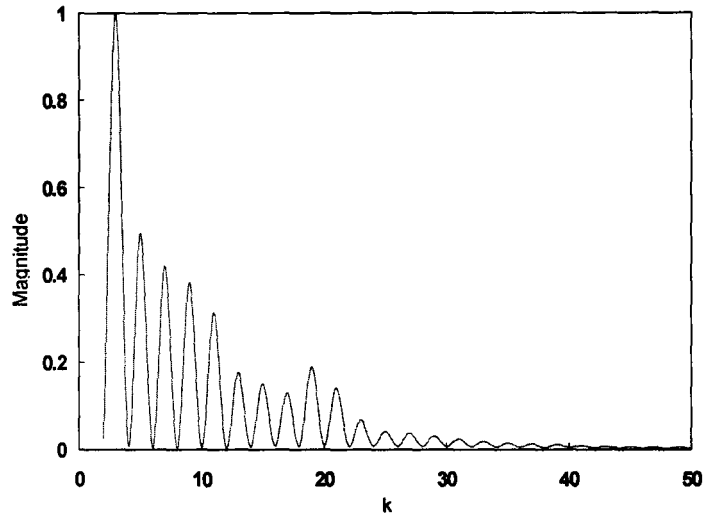


Figure 6.6 power spectrum of electrostatic transfer field from new modified 3D dielectric distribution

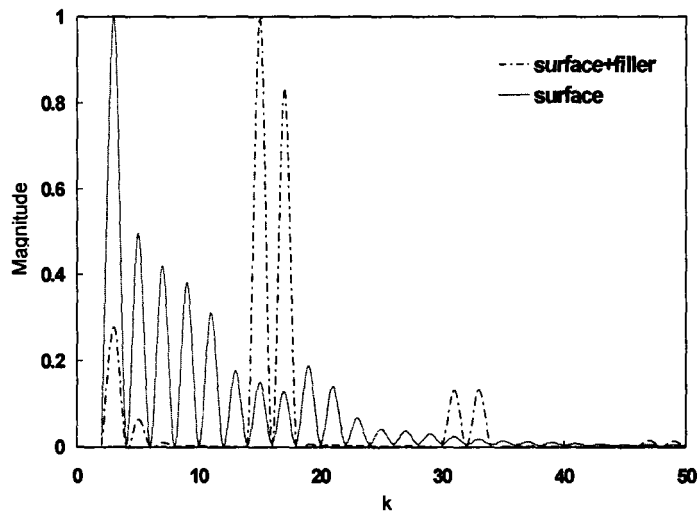


Figure 6.7 The power spectra of electrostatic transfer field from (i) filler layer added to the top of the modified 3D dielectric (dash-dotted line); (ii) new modified 3D dielectric distribution (solid line).

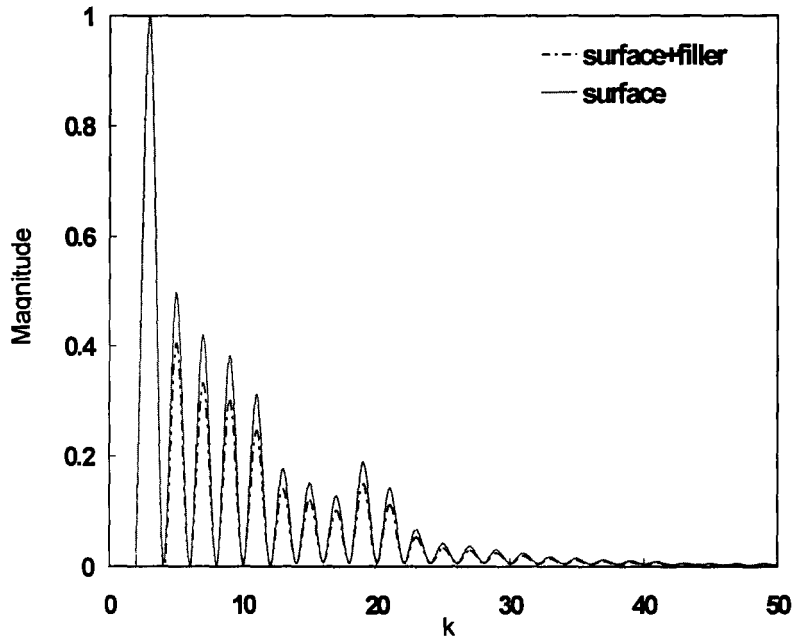


Figure 6.8 The power spectra of electrostatic transfer field from (i) filler layer added to the bottom of the modified 3D dielectric (dash-dotted line); (ii) new modified 3D dielectric distribution (solid line)

The above numerical experiments conclude that the surface variations and filler on top (coating layer) is the most important factors controlling the final toner density distribution.

Suggestions on commercial paper making

Normally the process of paper coating is analogous to the filling of holes in a wall (fibre network surface) before painting. Suppose that original ‘wall surface’ - the

fibre network surface, has some dielectric distribution, which generate a fluctuated electrostatic field. Then the painting objects (coating layer) with another dielectric distribution are added to the paper surface. The resulting final electrostatic field will be greatly influenced by this new added layer. If this coating layer is specially chosen, then the fluctuation of the final electrostatic field can be greatly reduced from the combination effect of ‘wall surface’ and painting materials. That is, the effect from added filler distribution can offset the fluctuation of electrostatic transfer field generated from surface roughness. Thus, in toner transfer process, the fluctuation of electrostatic transfer field can be greatly reduced and obtain a uniform transfer force, which can reduce the toner density variation.

Preliminary numerical experiments have been done on handsheet paper. The simulated handsheet paper in chapter 3 is used as ‘wall surface’, and dielectric distribution of filler layer is added to the top of the paper surface. It is proved that a suitable distribution of filler particles can efficiently reduce the fluctuation of the toner transfer field.

In future, a study can be done on how to choose the suitable filler distribution. It is better to find the relationship between the added filler distribution and the original paper surface. Suppose $\varepsilon_{papersurface}(\vec{x})$ and $\varepsilon_{fillerparticles}(\vec{x})$ are the dielectric distribution of added filler and original paper network. The combined dielectric distribution is an input into equation below

$$\nabla \cdot (\varepsilon(\vec{x})(-\nabla\phi(\vec{x}))) = \rho(\vec{x}) \quad (6.1)$$

Then the resulted fluctuation of $\phi_{new}(\vec{x})$ is reduced. If the $\varepsilon_{fillerparticles}(\vec{x})$ can be found according to the known $\varepsilon_{papersurface}(\vec{x})$ and $\phi(\vec{x})$, a better paper making scheme will be developed to efficiently reduce the printing mottle and obtain good printing quality.

BIBLIOGRAPHY

- Alava, M. and Niskanen, K. (2006). “The Physics of Paper.” Rep. Prog.Phys, 69: 669-723
- Attwood, D., Parker, J. R. (1962). “Basis Weight Variations Over Small Areas of Paper.” Pap. Technol. 3(5): 435-443.
- Batten, G. L., Delekto, P. J. (1996). “A new test for toner adhesion.” In TAPPI Proceedings, Papermakers Conference.
- Bronkhorst, C. A. (2003). “Modelling Paper as a Two-Dimensional Elastic-Plastic Stochastic Network.” International Journal of Solids and Structures, 40: 5441-5454
- Butler, A. J., Hoburg, J. F., Cendes, Z. J. (1991). “A Model for Space Charge Evolution and Charge Deposition in the Electrophotographic Toner Transfer Process.” IEEE Tans. Industry appl., 27: 1218-1224.
- Cassidy, A., Grant, M., Provatas, N. (2004). “Modelling Dielectric Heterogeneity in Electrophotography.” Modelling Simul. Mater. Sci. and Eng: 91-107.
- Chalkin, P. M., Lubensky, T. C. (1995). Principles of Condensed Matter Physics, Cambridge University Press, Cambridge, UK.
- Chubb J. N. (1990). “Instrumentation and Standards for Testing Static Control Materials.” IEEE Trans Ind Appl, 26 (6): 1182.
- Chubb J. N. (1996). “Corona Charging of Practical Materials for Charge Decay Measurements.” J. Electrostatics, 37: 53.
- Methods for Measurements in Electrostatics. (1996). British Standard BS 7506: Part 2.
- Chubb J. N. (1999). “The Assessment of Materials by Tribo and Corona Charging and Charge Decay Measurement.” Inst Physics ‘Electrostatics 1999’ Confr.

Cambridge, March IoP Conf Series, 163: 329-333.

Chubb J. N. (2000). “Measurement of Tribo and Corona Charging Features of Materials for Assessment of Risks from Static Electricity.” IEEE-IAS Meeting Phoenix, Arizona Oct 1999 IEEE Trans Ind Appl, 36 (6): 1515.

Chubb J. N. (2002). “New Approaches for Electrostatic Testing of Materials.” J. Electrostatics, 54: 233.

Corte., H. (1957) “The Porous Structure of Paper. In Fundam. Papermaking Fibres, Trans. Symp.” Br. Pap. Board Makers’ Assoc., London: 301-331.

Corte, H., Kallmes, O. J. (1960). Tappi J., 43: 737

Czarnecki, W. S., Schein, L. B. (2004). “Electrostatic Force Acting on a Spherically Symmetric Charge Distribution in Contact with a Conductive Plane.” J. Electrostat., 61: 107-115.

Dan, A., Hays, D. (1995). “Toner adhesion.” Adhesion, 51:41–48.

Dejesus, M. C., Rimai, D. S., Quesnel, D. J. (2006). “Effect of Young’s Modulus on the Detachment Force of 7 um Particles.” Langmuir:729-735.

Deng, M. (1994). Paper: An Engineered Stochastic Structure. Atlanta, Tappi Press.

Eltern, M. Modeling and Simulation of an Electrostatic Image Transfer. PhD dissertation. Technische Universität, München.

Fox, C. A., Bertrand, J. C. (1992) “Processes for Toner Pigment Dispersion.” U.S. Patent 5,080,995.

Fukuchi, Y., Takeuchi, M. (1998). “A comparative Study on Toner Adhesion Force Measurements by Toner Jumping and Centrifugal Method.” In Proc. of IS&Ts NIP 14 International Conference on Digital Printing Technologies: Society for Imaging Science and Technology: 390–393.

- Fuller, T. J., VanLaeken, A. C., Prest, W. M. (1993). “Toner Polymers and Processes Thereof.” U.S. Patent 5,266,438.
- Gady, B., Schleef, D., Reifenberger, R. (1996). “Identification of Electrostatic and Van der Waals Interaction Forces between a Micrometer-Size Sphere and a Flat Substrate.” Physical Review B, 53(12): 8065–8070.
- Gady, B., Reifenberger, R., Schaefer, D. M., Bowen, R. C., Rimai, D. S., DeMejo, L. P., Vreeland, W. (1998). “Particle Adhesion to Elastomeric Substrates and Elastomeric Substrates with Semi-Rigid Coatings.” Journal of Adhesion, 67: 19-36.
- Gady, B., Quesnel, D. J., Rimai, D. S., Leone S., Alexandrovich, P. (1999). J. Imaging. Sci. Technol., 43: 288.
- Garboczi, E. J., Day, A. R. (1995). “An Algorithm for Computing the Effective Linear Elastic Properties of Heterogeneous Materials:3-D Results for Composites with Equal Phase Poisson Ratios.” J.Mech.Phys.Solids, 43:1349.
- Gibson, L. J., Ashby, M. F. (1988). Cellular Solids, Structure and Properties, Pergamon Press, Oxford, UK.
- Goel, N. S., Spencer, P. R. (1975). Polymer Science Technology, Part B, L.H.Lee (Ed.), New York, Plenum Press.
- Gompf R. H. (1998). “Standard Test Method for Evaluating Triboelectric Charge Generation and Decay.” NASA Doc: MMA-1985-79 Rev 3.
- Gotzinger, M., Peukert, W. (2004). “Particle Adhesion Force Distributions on Rough Surfaces.” Langmuir, 20: 5298-5303.
- Grushkin, B. (1992). “Processes for the Preparation of Toners.” U.S. Patent 5,145,762.
- DeMejo, L. P., McCabe, J. M., Wilson, J. C. (1992). “Toner Compositions Containing a Multi-Purpose Additive.” U.S. Patent 5,112,715.

- Gupta, H., Chatterjee, S. G. (2003). “Parallel Diffusion of Moisture in Paper. Part 1 : Steady-State Conditions.” Ind. Eng. Chem. Res., 42: 6582-6592.
- Gupta, H., Chatterjee, S. G. (2003). “Parallel Diffusion of Moisture in Paper. Part 2 : Transient condition.” Ind. Eng. Chem. Res., 42: 6593-6600.
- Hasegawa, J., Yanagida, N., Tamura, M. (1999). “Toner Prepared by the Direct Polymerization Method in Comparison With Pulverization Method.” Colloids and Surfaces A: Physiochemical and Engineering Aspects, 153: 215-220.
- Hays, D. A. (1978). Photographic Sci. Eng. 22: 232.
- Hays, D. A. (1996). Advances in Particle Adhesion, D. S. Rimai and L. H. Sharpe (Eds), Gordon and Breach Publishers, Amsterdam.
- Hays, D. A., Sheflin, J. C. (2005). “Electrostatic Adhesion of Ion and Triboelectric-Charged Particles.” Journal of Electrostatics: 63687-63692.
- Herdan, G. (1960). Small particle statistics. Butterworths, London.
- Hirakawa, H., Murata, Y. (1996). “Generation of Fine Dry Toner and Its Charging Characteristics.” Industry Application Conference, Thirty-first IAS Annual Meeting, IAS'96 Conference Record of the 1996 IEEE, 4: 2026-2030.
- Hornbeck, R.W. (1975). Numerical Methods. New York, Quantum.
- Hunter, R. (1995). Foundations of Colloid Science. Clarendon Press.
- IEC 61340-2-1. (2000). “Measurement Methods in Electrostatics – Test Method to Measure the Ability of Materials and Surfaces to Dissipate Static Electric Charge.” International Electrotechnical Commission
- Jang, H. F. (2001). “The Science of Papermaking, Tran.12th Fund. Res. Symp..” Pulp Paper Fund.Res.Soc., 1:193-210.
- Jang, H. F., Weigel, G., Seth, R. S., Wu, C. B. (2002). “The Effect of Fibril Angle on

- the Transverse Collapse of Papermaking Fibres.” Paperija Puu, 84(2): 112-115.
- Johnson, K. L., Kendall, K., Roberts, A. D. (1971). Proc. R. Soc. London, Ser. .
- Kallmes, O., Ayer, J. A. (1987) Pulp Pap. ,61: 99.
- Kallunki, J., Alva, M., Hellen, E. K. O., 2005, preprint
- Keller, D. S., Luner, P. (1998). “An Instrument for Electron Beam and Light Transmission Imaging of Mass Distribution in Paper and Fibrous Webs.” Review of Scientific Instruments, 69:2495-2503.
- Keller, D. S., Pawlak, J. J. (2001). “Beta-Radiographic Imaging of Paper Formation Using Storage Phosphor Screens.” Journal of Pulp and Paper Science, 27:117-123.
- Kirkpatrick, S., Stoll, E. (1981). J. Comput. Physics, 40: 517.
- Kolseth, P. (1986). The Cell Wall Components of Wood Pulp Fibers in Paper Structure and Properties. New York, Dekker Inc.
- Küttner, A., Epping, R. (1998). “Measurements with a Small, Low-Cost Toner Charge Spectrometer.” In Proc. of IS&Ts NIP 14 International Conference on Digital Printing Technologies: 623–626.
- Landau, L. D., Lifshitz, E. (1959). Theory of Elasticity, 3rd ed., Butterworth-Heinemann Woburn, USA.
- Law, K. Y., Tarnawskyj, I. W., Salamida, D., Debies, T. (1994). “Mechanism of Triboelectrification in Xerographic Toner.” Industry Application Society Annual Meeting, Conference Record of the 1994 IEEE:1364-1367.
- Lee, M. H., Ayala, J. (1985). “Adhesion of Toner to Photoconductor.” J. Imaging Technol., 11: 279-284.
- Lee, M. H., Jaffe, A. B. (1988). Particles on Surfaces 1: Detection, Adhesion, and

Removal, K.L.Mittal (Ed.). Plenum Press, New York.

Mahabadi, H. K., Agur, E. E., Allison, G. R., Hawkins, M. S., Drappel, S., McDougall, M. N. V., Grushkin, B., Hoffend, T. R., Barbetta, A. J. (1994). “Toners Having Cross-Linked Toner Resins.” U.S. Patent 5,352,556.

Mastrangelo, C. J. (1982). “Effects of Charge, Size, and Shape on Toner Photoconductor Adhesion in Electrophotographic System.” Photographic Sci. Eng., 26: 194-197.

Hoffmann, Rainer (2004). Modeling and Simulation of an Electrostatic Image Transfer. PhD Thesis, Technische University Munchen.

Metcalf, M., Press, W. H., Teukolsky, S. A., Vetterling, W. T., Flannery, B. P. (1992). Numerical Recipes in Fortran 90, Cambridge University Press, Cambridge.

Mizes, H., Ott, M., Eklond, E., Hays, D. (2000). “Small particle adhesion: Measurement and Control.” Colloids and Surfaces, 165:11–23.

Nilsen, N., Zabihian, N., Niskanen, K., (1998). “A New Tool for Simulating Paper Properties.” Tappi J.,81(5):163-166.

Norman B., Wahren, D. (1974). “The Measurement of Mass Distribution in Paper Sheets Using a Beta Radiographic Method.” Sven. Paperstidn, 77(11) :397-406.

Norman, B., Wahren, D. (1976). Mass Distribution and Sheet Properties of Paper. In Fundam. London, Br. Pap. Board Ind. Fed.

Niskanen, K., Alava, M. (1994). “Planar Random Networks with Flexible Fibers.” Phys.Rev.Lett., (73):3475.

O’Neill, M., Jordan, B. (2000). The Journal of Pulp and Paper Science, 26(4): 131.

Ooij, I. W. J. (1969). “Beta Radiography of Paper Using a Flat Beta-ray Source (in

- Durch).” Papierwereld, 24(3): 67-73.
- Paavilainen, L. (1993). Paperi ja Puu, 46: 689.
- Page, L. (1928). Introduction to Theoretical Physics, D. Van Nostrand Company, New York.
- Pawlak, J. J., Keller, D. S. (2001). “Analytical Technique for the Comparison of Paper Formation Imaging Methods.” Journal of Pulp and Paper Science, 27:171-176.
- Provatas, N., Haataja, M., Asikainen, J., Majjaniemi, S., Alava, M., and Alanissila, T. (2000). J. Colloids Surfaces, 165: 209.
- Provatas, N., Haataja, M., Asikainen, J., Majjaniemi, S., Alava, M., Alanissila, T. (2000). “Fibre Deposition Models in Two and Three Spatial Dimensions.” J. Colloids Surfaces, (165): 209.
- Provatas, N., Cassidy A., Inoue, M. (2001). “Dielectric Variation in Paper and Its Effects on Print Density Mottle in Electrophotographic Printing.” Pulp and Paper Report.
- Provatas, N., Uesaka, T. (2003). “Modelling Paper Structure and Paper-Press Interactions.” Journal of Pulp and Paper Science, 29(10): 332-340.
- Pulp & Paper TAPPI Test Methods Standard T 205 sp-95, 1995, TAPPI.
- Rasi, M., Koponen, A., Aaltosalmi, U., Timonen, J., Kataja, M., Niskanen, K. (1999) “Permeability of Paper: Experiments and Numerical Simulations, Proc.” TAPPI Paper Physics Conf.: 297-306.
- Rimai, D. S., DeMejo L. P., Bowen, R. C. (1990). J. Appl. Phys., 68: 6234.
- Rimai, D. S., Moore, R. S., Bowen, R. C., Smith V. K., Woodgate, P. E. (1993) J. Mater. Res., 8: 662.
- Rimai, D.S., Quesnel, D. J., Bowen, R. C. (2001). “Particle Adhesion to Highly

- Compliant Substrates: Anomalous Power-Law Dependence of the Contact Radius on Particle Radius.” Langmuir, 17: 6946-6952.
- Rimai, D. S., Quesnel, D. J., DeMejo, L. P., Regan, M. T. (2001). “Toner to Photoconductor Adhesion.” J. Imaging. Sci. Technol., 45: 179-186.
- Rimai, D. S., Ezenyilimba, M., Goebel, W. K., Cormier, S., Quesnel, Q. J. (2002). “Toner Adhesion: Effects of Electrostatic and van der Waals Interactions.” Journal of Imaging Science and Technology, 46: 200-207.
- Rimai, D.S., Alexandrovich, P., Quesnel, D. J. (2003). “Effects of Silica on the Adhesion of Toner to a Composite Photoconductor.” J. Imaging Sci. Technol., 47: 1-8.
- Rimai, D. S., Weiss D. S., Quesnel, D. J. (2003). “Particle Adhesion and Removal in Electrophotography.” J. Adhesion Sci. Technol., 17: 917-942.
- Rimai, D. S. (2004). “Electrophotographic Printing on Textiles and Non-Planar Substrates.” Journal of Imaging Science and Technology, 48: 10-14.
- Roberts, A. P., Garboczi, E. J. (2000). “Elastic Properties of Model Porous Ceramics.” J. Am. Ceram. Soc., 83(12): 3041-3048.
- Rodal, J. J. A. (1983). “Paper Deformation in a Calendering Nip.” Tappi, 76(12):63
- Rushing, A. J., Fields, R. D. (2001). “Toner Satellite Formation in Electrostatically Transferred Images.” Journal of Imaging Science and Technology, 45(2):187–197.
- Schaffert, R. M. (1975). Electrophotography. New York, Focal Press Limited.
- Scharfe M. (1984). Electrophotography Principles and Optimization, vol.3 Electrostatics and Electrostatic Application Series. New York, Wiley.

- Schein, L. B. (1988). Electrophotography and Development Physics. New York, Springer-Verlag.
- Schein, L.B. (1996). Electrophotography and Development Physics, revised 2nd ed. Laplacian Press, CA.
- Schein, L. B. (1999). “Recent Advances in Our Understanding of Toner Charging.” Journal of Electrostatics, 46: 29-36.
- Schein, L. B., Czarnecki, W. S. (2004). “Proximity Theory of Toner Adhesion.” J. Imaging Sci. Technol., 48: 412-416.
- Schein, L.B., Czarnecki, W. S., Christensen, B., Mu T., Galliford, G. (2004). “Experimental Verification of the Proximity Theory of Toner Adhesion.” J. Imaging Sci. Technol., 48: 417-425.
- Schein, L. B., Czarnecki, W. S. (2005). “Electrostatic Proximity Force, Toner Adhesion, and Atomic Force Microscopy of Insulating Particles.” J. Electrostat., 63: 699-704.
- Scott, W.E. (1995). Properties of Paper. 2 ed. Tappi Press, Georgia.
- See, E.G, Andrade, J. S., Herrmann, H. J., Andrade, R. F. S., Da Silva, L. R. (2005). Phys. Rev. Lett, (94): 018702.
- Soux, S., Feugeas, F., Bach, M., Fagon, M., Bettinger, C., Mourad, S., Cornet, A. (2008) “Determination of Paper Filler Z-Distribution by Low-Vacuum SEM and EDX.” Journal of Microscopy, 229: 44-59.
- Sundholm, J. (1999). Mechanical Pulping. Helsinki, fapet.
- Takeuchi, M. (2006). “Adhesion Forces of Charged Particles.” Chemical Engineering Science, 61: 2279-2289.
- “Forming Handsheets for Physical Tests of Pulp.” TAPPI Test Method T 205.

- Trottenberg, U., Oosterlee, C. W. Schuller, A. (2001). Multigrid, Academic Press, London.
- Tydeman, P.A. (1965). “The Measurement and Automatic Print-out of Small Scale Basis Weight Variations.” Br. Pap. Board Ind. Res. Assoc. Bulletin, 39:8-19.
- Williams, E. M. (1984). The Physics and Technology of Xerographic Process. New York, Wiley.
- Wright, G., Tombs, T. N., Chowdry, A., Weiss, D. S., Rimai, D. S. (2005). “Toner transfer: Effects of size polydispersity.” J. Imaging Sci. Technol., 49: 531-538.
- Wyko NT1100 Instruction Menu, <http://www.veeco.com/>.
- Vivaldo-Lima, E., Wood, P. E., Hamielec, A. E., Penlidis, A. (1997). “An Updated Review on Suspension Polymerization.” Ind. Eng. Chem. Res., 36 (4): 939-965.
- Yamauchi, T. (1989). “Compressibility of Paper Measured by Using a Rubber Platen Thickness Gauge.” Appita, 42(3): 222-224.
- Yang, C. C., Hartmann, G. C. (1976). “Electrostatic Separation of a Charged-Particle Layer Between Electrodes.” IEEE Transactions on Electron Devices, 23: 308-312.
- Yang, J., Wang, T., He, H., Wei, F., Jin, Y. (2003). “Particle Size Distribution and Morphology of in situ Suspension Polymerized Toner.” Ind. Eng. Chem. Res., 42: 5568-5575.
- Yuan, H. G., Kalfas, G., Ray, W. H. (1991). “Suspension Polymerization.” J. Macromol. Sci., Rev. Macromol. Chem. Phys., C31(2 and 3): 215-299.
- Zhou, H., Gotzinger, M. Perkert, W. (2003). “The Influence of Particle Charge and Roughness on Particle Substrate Adhesion.” Power Technology, 135-136: 82-91.